Numerical Analysis of Blade Tip Leakage Flow and Shroud Heat Transfer in Gas Turbine Engines

Md. Hamidur Rahman

A Thesis

in

The Department

of

Mechanical and Industrial Engineering

Presented in Partial Fulfillment of the Requirements

for the Degree of Master of Applied Science (Mechanical Engineering) at

Concordia University

Montreal, Quebec, Canada

December 2008

Library and Archives
Canada

Published Heritage
Branch

395 Wellington Street
Ottawa ON K1A 0N4
Canada

Bibliothèque et
Archives Canada

Direction du
Patrimoine de l'édition

395, rue Wellington
Ottawa ON K1A 0N4
Canada

Your file Votre référence
ISBN: 978-0-494-63240-6
Our file Notre référence
ISBN: 978-0-494-63240-6

NOTICE:

The author has granted a non-exclusive license allowing Library and Archives Canada to reproduce, publish, archive, preserve, conserve, communicate to the public by telecommunication or on the Internet, loan, distribute and sell theses worldwide, for commercial or non-commercial purposes, in microform, paper, electronic and/or any other formats.

The author retains copyright ownership and moral rights in this thesis. Neither the thesis nor substantial extracts from it may be printed or otherwise reproduced without the author's permission.

AVIS:

L'auteur a accordé une licence non exclusive permettant à la Bibliothèque et Archives Canada de reproduire, publier, archiver, sauvegarder, conserver, transmettre au public par télécommunication ou par l'Internet, prêter, distribuer et vendre des thèses partout dans le monde, à des fins commerciales ou autres, sur support microforme, papier, électronique et/ou autres formats.

L'auteur conserve la propriété du droit d'auteur et des droits moraux qui protège cette thèse. Ni la thèse ni des extraits substantiels de celle-ci ne doivent être imprimés ou autrement reproduits sans son autorisation.

In compliance with the Canadian Privacy Act some supporting forms may have been removed from this thesis.

While these forms may be included in the document page count, their removal does not represent any loss of content from the thesis.

Conformément à la loi canadienne sur la protection de la vie privée, quelques formulaires secondaires ont été enlevés de cette thèse.

Bien que ces formulaires aient inclus dans la pagination, il n'y aura aucun contenu manquant.

Canada

ABSTRACT

Numerical Analysis of Blade Tip Leakage Flow and Shroud Heat Transfer in Gas Turbine Engines

Md. Hamidur Rahman

One of the most critical components of gas turbine engines, rotor blade tip and casing, is exposed to high thermal load. It is a significant challenge to the designer to protect the turbine material from this severe situation. Leakage flow over the blade tip is also one of the important issues to improve the turbine performance. To understand the detailed phenomena and natures of the heat transfer on the turbine blade tip and casing in association with the tip leakage flow under actual turbine operating conditions, both steady and unsteady simulations have been conducted.

A single stage gas turbine engine was modeled and simulated using commercial CFD solver ANSYS CFX R.11. The modeled turbine stage has 30 vanes and 60 blades with a pressure ratio of 3.2 and a rotational speed of 9500 rpm. The predicted isentropic Mach number and adiabatic wall temperature on the casing showed good agreement with available experimental data under the close operating condition.

Through the steady simulations, the typical tip leakage flow structures and heat transfer rate distributions were analyzed. The tip leakage flow separates and recirculates just around the pressure side edge of the blade tip. This coverage of the recirculating flow results in low heat transfer rates on the tip surface. The leakage flow then reattaches on the tip surface beyond the flow separation zone. This flow reattachment has shown enhanced heat transfer rates on the tip. The leakage flow interaction with the reverse cross flow, induced by relative casing motion, is found to have significant effect on the casing heat transfer rate distribution. Critical region of high heat transfer rate on the casing exists near the blade tip leading edge and along the pressure side edge. Whereas near the suction side the heat transfer rates are relatively low due to the coverage of the reverse cross flow. The effects of the tip clearance heights and rotor rotating speeds were also investigated. The region of recirculating flow increases with the increase of clearance heights. The flow incidence changes and the casing relative motion is enhanced with higher rotation speeds. As a result, the high heat transfer rate regions have been changed with these two parameters.

Unsteady simulations have been performed to investigate time dependent behaviors of the leakage flow structures and heat transfer on the rotor casing and blade tip. The effects of different time steps, number of sub iteration and number of rotor vane passing were firstly examined. The periodicity of the tip leakage flow and heat transfer rate distribution is observed for each vane passing. The relative change in the position of the vane and the vane trailing edge shock alters the inlet flow conditions of the rotor part. It results in the periodic variations of the leakage flow structures and heat transfer rate distributions. The higher heat transfer rates were observed at the region where the trailing edge shock reached. The maximum amplitude of the pressure fluctuation in the tip region is about 20% of the averaged rotor inlet pressure. The maximum amplitude of the heat transfer rate fluctuation on the blade tip, caused by the unsteady leakage flow variations, reaches up to about 25% of the mean heat transfer rate. The effects of tip clearance heights and rotor speeds have also been analyzed and compared one with respect to others. Same typical patterns of leakage flow structures and heat transfer rate distribution can be obtained in both steady and unsteady simulations. However, steady simulation underpredicted the highest heat transfer rate. Because it couldn't capture the critical local high heat transfer phenomena caused by the unsteady stator-rotor interactions.

DEDICATION

To my respected teacher Prof. Dr. Md. Abdur Razzaq Akhanda and my parents who have been my source of inspiration.

ACKNOWLEDGMENT

Praise be to GOD, who gave me the success in this endeavor.

I would like to express my sincere thanks and gratitude to Dr. Ibrahim Hassan, my research advisor, for his consistent support, guidance and encouragement throughout this research period. I would also like to thank Dr. Sung In Kim, research associates, for sharing his thoughts and ideas to enrich the technical side of this thesis.

I am also grateful to my parents, my brother for their encouragement and love. I would like to thank my wife, Sara Afroz, for her endless support and my only lovely son, Tahmid Rahman, who makes my life happy.

A special thanks to all my dearest research colleagues, Dr. Chad, Minh, Dr. Roland, Tariq and Dr. Saleh who graduated and present member includes Ayman, Dino, Feng, Mohamed, Tarek. Their support, advice, comments are greatly acknowledged.

Table of Contents

List of Figures

List of Tables

Nomenclature

C	Chord at the blade tip, *(m)*
C_x	Axial chord distance at the blade tip, *(m)*
FB	Front Blade
H	Heat transfer coefficient, $\left(\frac{W}{m^2 \cdot K}\right)$
LE	Leading edge
PS	Pressure side
Pr	Prandtl number
P_k	Production rate for turbulence due to viscous force, $\left(\frac{kg}{m \cdot s^3}\right)$
RB	Rear Blade
SS	Suction side
S	Strain rate $\left(=\frac{1}{2}\left(\frac{\partial U_i}{\partial x_j}+\frac{\partial U_j}{\partial x_i}\right)\right)$, (s^{-1})
TE	Trailing edge
T	Static temperature, *(K)*
T_{tot}	Total temperature, *(K)*
T^*	Non-dimensional temperature
T_f	Near wall temperature, *(K)*
T_w	Wall temperature, *(K)*
$T_{os,in}$	Stator inlet total temperature, *(K)*

$T_{or,in}$	Rotor inlet total temperature, *(K)*
$\overline{U}$	Reynold's average velocity vector (x,y,z), *(m/s)*
$\vec{U}$	Velocity vector (x,y,z), *(m/s)*
c_p	Specific heat at constant pressure, $\left(\dfrac{J}{kg \cdot K}\right)$
c_v	Specific heat at constant volume, $\left(\dfrac{J}{kg \cdot K}\right)$
h	Static enthalpy, $\left(\dfrac{J}{kg}\right)$
$\overline{h}$	Average enthalpy, $\left(\dfrac{J}{kg}\right)$
h'	Fluctuating enthalpy, $\left(\dfrac{J}{kg}\right)$
h_o	Total enthalpy, $\left(\dfrac{J}{kg}\right)$
k	Turbulent kinetic energy$\left(=\dfrac{\overline{u'^2}+\overline{v'^2}+\overline{w'^2}}{2}\right)$, $\left(\dfrac{m^2}{s^2}\right)$
$\overline{p}$	Average pressure, (Pa)
p	Absolute Pressure, *(Pa)*
q	Heat flux, $\left(\dfrac{W}{m^2}\right)$
r	Position vector, *(m)*
t	Time, *(s)*
t^*	Non-dimensional time

t_y	Blade thickness, *(m)*
Δt	Time step, *(s)*
u_τ	Wall friction velocity, $\left(\frac{m}{s}\right)$
u^*	Alternative velocity scale
u	u-component of velocity in x direction, *(m/s)*
u'	Fluctuating velocity component in x direction, *(m/s)*
$\bar{u}$	Average velocity component in x direction, *(m/s)*
v	v-component of velocity in y direction, *(m/s)*
v'	Fluctuating velocity component in y direction, *(m/s)*
$\bar{v}$	Average velocity component in y direction, *(m/s)*
w	w-component of velocity in z direction, *(m/s)*
w'	Fluctuating velocity component in z direction, *(m/s)*
$\overline{w}$	Average velocity component in z direction, *(m/s)*
x	Axial coordinate, *(m)*
y	Tangential coordinate, *(m)*
y^+	Dimensionless distance from the wall
y^*	Alternate dimensionless wall spacing

Greek symbols

σ_{xx}	Stress component in x direction on a face normal to x, *(Pa)*
σ_{xy}	Stress component in y direction on a face normal to x, *(Pa)*

σ_{xz}	Stress component in z direction on a face normal to x, *(Pa)*
σ_{yx}	Stress component in x direction on a face normal to y, *(Pa)*
σ_{yy}	Stress component in y direction on a face normal to y, *(Pa)*
σ_{yz}	Stress component in z direction on a face normal to y, *(Pa)*
σ_{zx}	Stress component in x direction on a face normal to z, *(Pa)*
σ_{zy}	Stress component in y direction on a face normal to z, *(Pa)*
σ_{zz}	Stress component in z direction on a face normal to z, *(Pa)*
μ	Dynamic viscosity, $\left(\frac{kg}{m \cdot s}\right)$
μ_t	Turbulent dynamic viscosity, $\left(\frac{kg}{m \cdot s}\right)$
ρ	Fluid's density, *(kg/m^3)*
Φ	Dissipation function
ω	Specific dissipation rate $\left(=\frac{k^{\frac{1}{2}}}{l}\right), \left(\frac{1}{s}\right)$
υ	Kinematic viscosity, $\left(\frac{m^2}{s}\right)$
θ	Stator passing period, *(s)*
ε	Turbulent dissipation rate $\left(=\rho C_\varepsilon \frac{k^2}{\mu_t}\right), \left(\frac{m^2}{s^3}\right)$
Ω	Rotor angular velocity, *(rpm)*
λ	Thermal conductivity of the fluid, $\left(\frac{W}{m \cdot K}\right)$

φ	Stator angular pitch, *(radians)*

Subscripts

abs	Absolute
f	Fluid
in	Inlet
w	Wall

Chapter 1

Introduction

In modern gas turbine engine, the inlet temperature is continuously increasing in order to improve engine performance in terms of efficiency and power. Due to rising demand for higher turbine performance, all turbine components are exposed to high thermal load which has been the major interest for the researcher to protect the turbine metal from melting. Heat load intensity of the turbine component is not uniform; rather it varies within the turbine stage and appears intensive in some critical region. Turbine tip clearance is such where leakage flow occurs due to pressure difference between the pressure side and suction side of the blade, resulting high heat transfer region on the blade tip and the casing. Figure 1.1, typically illustrates the turbine leakage flow regime at two different axial locations. The sections are taken at a normal to the blade camber line. It is seen that the flow enters the gap through reduced flow area due to flow separation near the pressure side of the tip surface that enhances the flow acceleration further. Flow mixing of the incoming jet occurs just after the separation and reattaches on the blade tip surface, depending upon the available blade thickness that allows sufficient room for the reattachment. This phenomena does not appear near the trailing edge due to reduced thickness of the blade. Eventually the leakage flow immerges into the adjacent blade passage where it interacts with the main flow or the passage flow to form leakage vortex. The size of the leakage vortex relies on the mass transfer rate through the gap as well as leakage flow velocity. Leakage flow deflection is seen lower near the leading

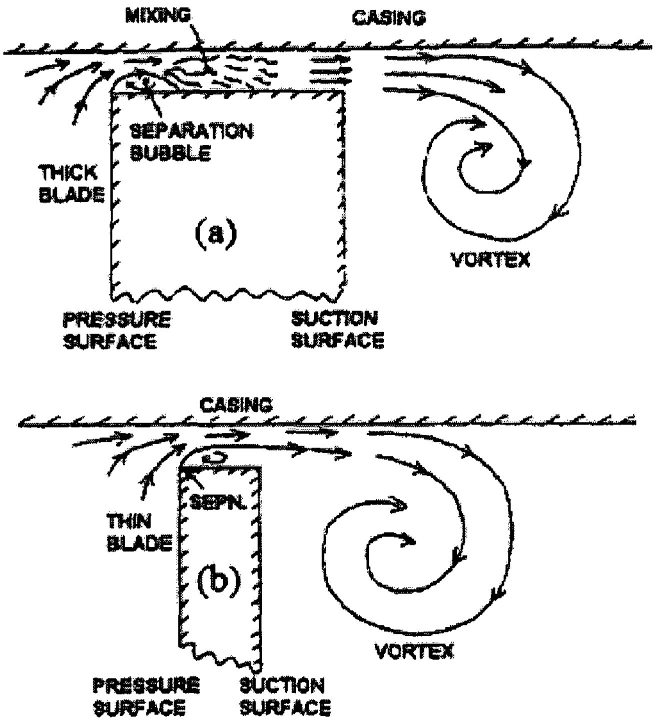

Figure 1.1 Schematic of typical over tip leakage flow [22].

edge because of small pressure difference exist between the pressure side and suction side of the blade. As the flow approaching to the trailing edge, the deflections become more and more because of increased pressure gradient. Therefore, the leakage vortex gets stronger and growing in size, as shown in Fig. 1.2, from leading to trailing edge. The impact of the tip leakage vortex and the flow field in the clearance region has been substantial in the performance of the gas turbine engine. It reduces the flow momentum and thus, decreases the overall turbine efficiency. On the other hand, it enhances the heat transfer rate on the tip surface, casing and the suction surface of the blade.

In gas turbine engine, the casing is stationary as seen from the absolute frame of reference, while the rotor is rotating at a higher speed. Engine working conditions are varying with the time that significantly affects the geometric heights of the tip clearance. When the engine runs at maximum load, potential surface rubbing may occur and may cause serious damage to the engine components. Therefore, a minimum gap between the tip surface and the casing should be maintained in order to accommodate centrifugal growth and the thermal expansion of the blade metal. Figure 1.3 presents the tip clearance variations at different operational conditions. Under idle condition, the tip gap is a geometric clearance while thermal and centrifugal effects are very significant during engine accelerated or decelerated. Hence, it is very important to accurately predict the data in the tip clearance region to ensure minimum gap in between and to protect it from any unwanted failure.

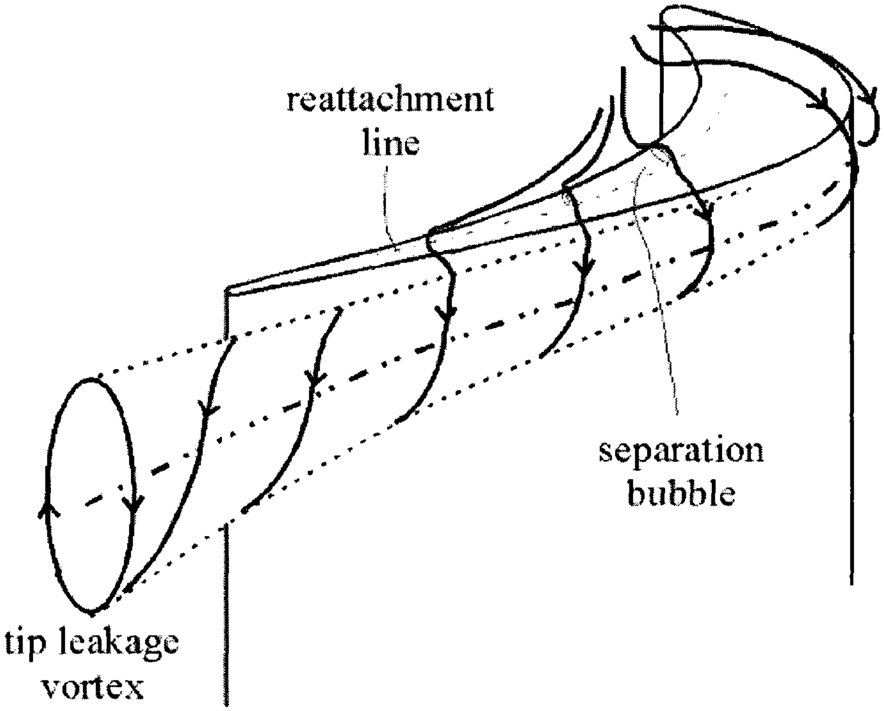

Figure 1.2 Schematic of a typical turbine tip leakage vortex [15].

There have been many experimental investigations conducted on the tip leakage flow and heat transfer under different working conditions. Unfortunately, due to geometric complexity and experimental limitations, it is very difficult to capture accurate data on the tip clearance region. For the sake of convenience, many people uses stationary turbine cascade that disregards the rotational effect on the flow structure and heat transfer which is somewhat unrealistic. However, these data could be useful for turbomachinary application, if special attention is paid for rotating turbine condition.

Computational simulation has been attracting the attention, in the recent years, due to its cost effectiveness and high accuracy predictions. It becomes an important tool in engineering application, in particular, in the field of fluid mechanics in order to predict highly three dimensional complex flow structures and variations of heat transfer distributions. Tip clearance region is the most critical turbine component which is still a major challenge for the aero space industry since no one could attain reliable or sufficient experimental data in that region. Hence, in order to meet their needs and demands, CFD becomes an invaluable tool for the aerospace industry.

This numerical study will be presented in the following way. First, a detailed literature review of the earlier studies, selected from the relevant field, more particularly, on tip leakage flow and associated heat transfer for both stationary cascades and rotating blades will be presented in Chapter 2. Following these, a numerical approach along with the details description of the model, governing equations, boundary conditions, and grid

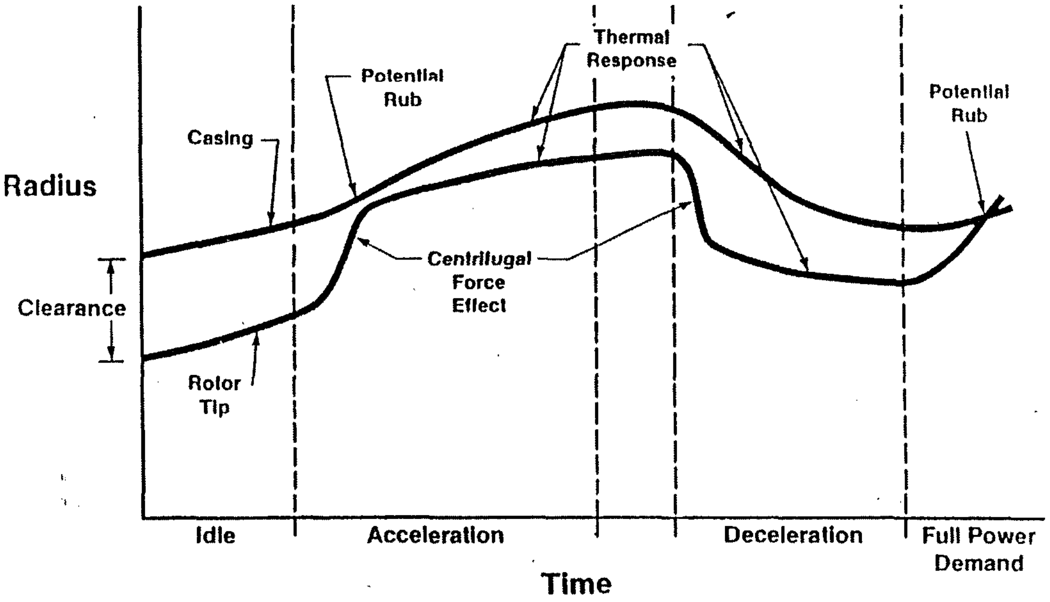

Figure 1.3 Variation of tip clearance height at different operating condition [45].

independency test will be discussed and then a brief introduction on the different test cases (test matrix) will be given in chapter 3, in order to clarify the key objectives of this study. In Chapter 4, CFD predictions will be validated using available experimental data and the steady state results will then be analyzed for the rotor blade tip and casing surface for all the cases. In Chapter 5, results of unsteady simulations will be investigated and discussed. Finally, conclusions and specific contributions, from the current study, will be drawn in the subsequent sections, as well as computational challenges and future directions that are required for further study of turbine leakage flow with associated heat transfer.

Chapter 2

Literature Review

In the recent studies, turbine tip aerodynamics and corresponding heat transfer have been focused in order to enhance gas turbine engine performance. There are many experimental as well as numerical studies in the past years, conducted with appropriate attention to the turbine tip geometry and its effect on the flow and heat transfer. In this section, a chronological review of these studies will be presented with two subsections. All studies that include both experimental and numerical works with stationary blades will be summarized in the first subsection, while the second subsection will cover the rotating turbine blades. The geometric consideration of the blade tip and its effect on heat transfer and aerodynamics will be covered in each section. Then all these studies will be summarized at the end of this chapter with the objectives and motivations of this present study.

2.1 Leakage Flow and Heat Transfer for Stationary Blade

2.1.1 Effect of Tip Clearance Height

Leakage flow over the tip is becoming important issue in gas turbine application to improve the performance. Tallman and Lakshminarayan [1] numerically studied the effect of the tip clearance heights on the tip leakage flow in a linear cascade. Three dimensional Navier stocks CFD code with standard k-ε turbulence model was used in their study. High resolution H grid was set in with appropriate clustering near the wall to achieve required y^+ value. This turbine cascade was simulated at the tip clearance heights of 2.5% and 1% of the blade span and comparison were made between them. They found that the reduced tip clearance greatly affects mass flow through the gap, vortex pattern and thermal losses. For the case of 2.5 % tip clearance height, a larger leakage vortex and high leakage flow was seen in compared to the low clearance height. However, the points where leakage vortex originates were found at the same location for both cases. The leakage vortex restrict the passage flow near the suction side and hence, cause secondary flow blockage and was seen severe for the case of 2.5% clearance height while 1% clearance height showed up severe for the near casing secondary flow. In later study [2], the author investigated the effect of relative motion of the turbine casing on the tip leakage flow. The same CFD code was used in this study with the exception in the boundary condition that the casing has velocity of 32 m/s relative to the rotor blade and the direction of rotation was set opposite to the blade motion. They found that a shear layer is developed on the wall surface that reduces the mass flow and increases the flow blockage. With the casing wall motion, the aerodynamic losses associated by the leakage vortex was seen higher due to leakage flow mixing with that of the passage cross flow, forms secondary flow near the hub, and further increases the losses.

The details study of heat transfer coefficient distribution on a gas turbine blade was done experimentally by Han and Azad [3]. Five bladed linear cascades were used for the test in a low speed wind tunnel facility under mainstream Reynold's Number of 5.3×10^5. They considered three different tip clearance heights of 1.1%, 2% and 3% of the blade span. The heat transfer coefficient distributions on the tip surface was measured using liquid crystal technique. At a smaller tip clearance height, the unsteady wake effect on the heat transfer was found to be lower. The critical region of high heat transfer was found at the mid chord of the blade. However, low heat transfer coefficient was observed from the leading edge to some extend along the suction side due to reduced tip leakage flow while higher heat transfer coefficient was observed at the pressure side tip. For the tip gap of 3%, the heat transfer is increased by the unsteady wake, however, at a reduced tip gap the wake effect on the heat transfer distributions were not seen significant. From their study, a higher heat transfer coefficient was reported at the mid chord region which was characterized by the higher pressure difference between the pressure and suction edge which results in increase in mass flow through the gap.

Eriksson et al. [4] numerically studied leakage flow and heat transfer in the tip region for the clearance heights of 1%, 1.5%, and 2.5% of the blade span. The geometry of the blade tip, investigated in this study, was flat tip surface and the cavity tip called squealer. They also focused on the CFD solver capabilities for different turbulence model to accurately predict the blade heat transfer and eventually used SST based k–ω model to validate the predictions with the experimental data. The inlet total pressure and temperature were specified as 129.6 kPa and 297 K, respectively, with a stage pressure ratio of 1.22. The wall surface temperature of 350 K was used for heat transfer measurement. Results showed that the high pressure loading on the casing is shifting towards the trailing edge region with the increase of the clearance heights. This pressure shifting cause the leakage flows to be dominating with higher flow acceleration near the trailing edge. Their study also revealed that the pressure distribution comparatively decreases for the case of squealer tip than that of the flat tip case, meaning that the mass transfer through the gap is reduced by the use of squealer tip configuration. Thus, the heat transfer rate is expected to be lower for this case since the amount of mass flow through the gap is seen lower in compared to flat tip case.

2.1.2 Effect of Tip Geometry

Key and Arts [5] experimentally compared turbine tip leakage flow for flat and squealer tip geometries under high speed condition. They performed flow visualization technique in order to analyze tip leakage flow structure on the suction surface of the blade. The results showed that squealer tip provides a significant reduction in velocity through the tip gap with compare to the flat tip blade. They found that the tip velocity levels were increased due to increase in Reynolds's number for the case of flat tip while squealer tip did not show any significant effect of Reynold's number. From the results, it was seen that a small region of constant pressure exist at 97.3% span for squealer tip. The highest pressure gradient or high tip leakage flow across the tip of the blade occurred at 6 to 8 percent of the axial chord. For the flat tip blade, a pressure side separation vortex was appeared on the tip of the blade while the squealer tip did not show such separation. From the visualization image, they observed that the flow is re-circulated inside the squealer tip cavity. The flow path lines were traced using oil dot on the surface and they observed that the flow leaves the cavity and travels along the squealer rim towards the leading edge. A tip leakage vortex appeared and found slightly larger in size for the squealer tip than the flat tip due to sufficient tip gap to accommodate vortex reattachment.

Schabowski and Hodson [6] investigated the tip leakage reduction technique using different turbine tip geometry. Both numerical and experimental results were presented in this paper. Different combinations of turbine recessed tip such as squealer; winglet were used to analyze their effects on the performance of the turbine. In the experimental investigation, 4-passage low speed linear cascade was used which consisted of three aluminum parts and one Perspex with variable tip gap size. The test section was also equipped with additional equipment to control the blade periodicity and path of the tip leakage vortex. On the other hand, the numerical simulation was performed by using commercial CFD code FLUENT version 6.1. Spalart Allmaras turbulence model was used with incompressible, segregated solver employing SIMPLEC algorithm. A hybrid mesh having 1.5 and 3.5 million grid points were generated by using GAMBIT. Observations revealed that a simple change to the tip design greatly affect the total pressure loss coefficient. They employed three techniques in order to reduce the tip leakage flow. It was demonstrated that in addition of winglet, two squealer and thin squealer results in reducing pressure gradient, total pressure loss coefficient and mass flow rate through the gap, respectively. From their study, it was seen that the total pressure loss coefficient reduced by as high as 22% for the combination of winglet-squealer tip in compared to flat tip geometry.

2.1.3 Combined Effect of Tip Geometry and Clearance Height

Han and Kwak [7], investigated tip geometry effect on the distribution of heat transfer coefficient on a squealer tip. They compared results for both squealer and flat tip geometry at a Reynolds number of 1.1×10^6 with 9.7% inlet turbulence intensity. The data were taken for three different tip clearances of 1%, 1.5% and 2.5% of the blade span. Results showed that the heat transfer coefficient is higher on the casing and the tip of the squealer near the pressure and suction surface. The rate of heat transfer for the squealer tip case was lower in compared to flat tip case since the mass flow through the gap is greatly reduced because of the presence of the squealer tip cavity. The cavity of the squealer tip affects the heat transfer variation over the tip surface from the leading edge to the trailing edge. Overall heat transfer coefficient was seen higher at the cavity near the leading edge because the leakage flow trapped inside and recirculated with flow reattachment on the cavity base. On the other hand, lower heat transfer coefficient was observed near the trailing edge cavity due to insufficient room to reattach the leakage flow on the cavity surface. Heat transfer coefficient showed higher at 10% of the chord due to leakage flow shifting towards the leading edge and was shown affected by the suction side mainstream flow. High heat transfer region at near tip pressure surface was reported in their study because of mainstream flow interactions with the leakage vortex.

Newton et al. [8] studied heat transfer and aerodynamics on five bladed cascades with three different blade tip geometries such as flat, suction side squealer and cavity squealer. Two tip clearance gaps of 1.6% and 2.8% were used with an exit Reynolds number of 2.3×10^5 based on exit velocity and chord. For the flat tip, the results showed that the flow separates near the pressure edge and reattaches on the tip surface that exhibits high heat transfer coefficient. They also measured heat transfer coefficient on the suction surface and found higher at a location where the leakage vortex attaches. In the same paper, they also compared the experimental results with the numerical to have more understanding on aerodynamics and heat transfer within the gap by using commercial CFX CFD code.

Effect of tip clearance and tip geometry were studied by Lamyaa [9] numerically to investigate heat transfer and pressure losses for an un-cooled gas turbine blade tip. Three different blade tip configurations such as flat tip, full perimeter and partial perimeter squealer were considered to investigate its effects on the heat transfer distributions. A three-dimensional, compressible CFD solver code called TACOMA was used for this numerical simulation. The effect of the clearance heights were also investigated for 1.25%, 2% and 2.75% of the blade span. From the study, it was found that the pressure distributions on the pressure surface at 97% of the span remains identical, regardless of the tip geometry configuration used. At the suction side, the variation of the pressure observed in between 30% and 80% of the chord distance where the peak pressure is dominating for the flat tip case. For all cases of the tip geometry, the surface heat transfer was increased with the increase of tip leakage flow due to increased mass flow through the gap. Full perimeter and partial perimeter cases showed higher heat transfer region at the pressure side rim and the bottom cavity surface. However, the heat transfer rate was observed comparatively higher on the rim surface than the cavity surface for all cases. From this numerical study, tip geometry with full perimeter squealer has been found the most effective configuration in compared to other tip geometries.

2.2 Tip Leakage Flow and Heat Transfer for Rotating Blade

2.2.1 Effect of Tip Clearance Height

Yamamoto et al. [10] have studied the unsteadiness of the flows and associated losses in the blade tip clearance region. Their test facility consisted of 1.5 stage, low speed axial turbine with the tip clearance of 1.2 mm. The random fluctuations of the flow were observed inside the tip clearance and caused higher losses for the turbine stage. The region where the leakage flow separates from the blade tip showed unsteady behavior. Stator and Rotor interaction showed significant contribution onto the unsteadiness and the leakage flow complexity.

Kumada et al. [11] experimentally investigated local heat transfer coefficient on the casing to explore the effects of inlet flow angles, rotor speeds and clearance heights. It was seen that the average value of the heat transfer coefficient increases with the increase of rotor speeds and the decrease of clearance heights. Averaged heat transfer rate in the condition of positive incidence was at its highest, and that in the on-design point was low.

Chana and Jones [12] conducted an experimental study on the turbine tip and the casing heat transfer under actual gas turbine condition in a high pressure light piston test facility. The type of the commercial turbine investigated for this experiment was consisted of 32 vanes and 60 rotor blades. The radial and circumferential temperature profile found in modern gas turbine engine was generated and used as the inlet temperature condition for their experiment. The experiment was carried out for fixed inlet temperature of 444 K and a radial temperature distribution ranges from 393 K to 470 K with maximum at the stator inlet mid span. The circumferentially averaged adiabatic wall temperature was presented on the casing surface showing a temperature drop of 100 K as the flow pass through the rotor passage from inlet to outlet. To investigate the heat transfer distribution on the casing surface, contour of Nusselt number was plotted. Three distinct regions of the high heat transfer were observed for uniform inlet temperature case, two of which were seen along the path of the unsteady vane wake flow direction while the other high heat transfer region is coincided with the traveling transonic shock wave originated from the vane trailing edge. Axial variations of the heat transfer were also presented for uniform and nonuniform temperature case. Experimentally, it was seen that the Nusselt number reaches maximum at 30% of the rotor axial chord for non-uniform case while the uniform case exhibits higher heat transfer rate at the leading edge and then falls gradually in the axial direction. Circumferentially averaged Nusselt number for uniform temperature profile was varying in the axial direction from the leading edge with a peak at 30% of the axial chord. High heat transfer on the casing was observed when the pressure side of the blade tip is approached and then rapidly decreases as it faces the blade tip suction side edge. Then, the heat transfer rate increases again as soon as the neighbor blade comes over the same location.

Aerodynamic and surface heat transfer measurements were conducted by the same author [13] on an intermediate pressure nozzle guide vane at the downstream of a high pressure turbine stage with both uniform and turbine inlet temperature distribution function. The experimental data were compared with two numerical predictions by integral method and TEXSTAN code. The integral method prediction was in well agreement with the experimental results at a turbulence level of 5% while the TEXTAN code provided good prediction at 10% turbulence level. From their study, it was observed that the radial total pressure distribution was affected by introducing intermediate pressure vane. It was also found that pressure surface Nusselt number considerably increases for non uniform temperature profile at the inlet. The Nusselt number distribution was presented at 1%, 50% and 90 % of the span using a uniform inlet temperature. The results showed peak at 50% of the span and then gradually dropped down to minimum value. The suction surface and pressure surface Nusselt number were also reported in their study. It was seen that at the suction surface the Nusselt number was gradually decreased and then remained constant from the throat to the trailing edge.

Polanka et al. [14] conducted parametric study on turbine tip and casing heat transfer in a single stage high pressure rotating turbine test facility. They have considered the effect of Reynolds number, pressure ratio, and gas to metal temperature ratio. Instantaneous pressure and heat transfer measurement were taken at the turbine casing region to compute the flow condition of full scale rotating turbine blade. They imposed an inlet pressure of 450 kPa, temperature of 480 K, Mach number of 0.08 and 1% turbulence intensity as the initial boundary condition. A nominal gap of 5% of the blade span was used as the tip clearance. Very high heat transfer rates were measured on both the blade tip and the casing with values as high as the stagnation region on the airfoil itself. They considered the effect of Reynolds number, pressure ratio, and the inlet temperature profile. Lower Reynolds numbers reduced the airfoil heat load in all regions. Both the higher and lower pressure ratios resulted in higher Nusselt numbers on the blade tip, due to increase of the driving temperature and separation, respectively.

Thorpe et al. [15] obtained unsteady heat transfer and aerodynamic data in a transonic turbine stage test facility. They particularly studied the effect of stator-rotor interaction on the unsteadiness of the heat transfer along the blade tip mean camber line. A total of 36 stator vanes and 60 rotor blades were used at a design speed of 8910 rpm. A new thin film gauge fabrication technique was implemented to measure time resolved heat transfer rates. The measured time-mean heat transfer rates along the mean camber line showed a variation that was qualitatively consistent with previously reported low-speed cascade tests. Three distinct heat transfer zones on the blade tip have been identified which have differing characteristic unsteady heat flux signatures: the blade-nose, mid-axial chord, and aft (downstream of the passage throat). The unsteady nature of the heat transfer was found to originate from tip leakage flow fluctuations, relative total temperature fluctuations and vane-shock interaction. From this study, it was also reported that the relative total temperature fluctuations are influenced by static pressure fluctuation.

Metzger et al. [16] numerically investigated tip leakage flow and heat flux characteristics on the casing for the Garrett TFE 731-2 blades. They have implemented an in house Navier stokes code, developed by Hah [44], for this numerical analysis. A grid of $30\times 7\times 102$ was used inside the clearance region for a gap of 0.025 inch. The numerical predictions were compared with the experimental data acquired from full turbine stage with an operating rotor speed of 20,000 RPM. From their observations both time resolved pressure and heat flux have been reported as periodic fluctuations. It was also observed that the pressure fluctuations are strongly influenced the casing heat flux.

Matsunuma et al. [17] experimentally investigated the effect of turbine flow velocity and different level of turbulent intensities ranged from 0.5% to 4.1%. The Reynolds number was varied from a value of 4.4×10^4 to 26.6×10^4. The flow velocity and the turbulence intensity variations influenced the flow distribution in the rotor passages. The height of the clearance was used as 0.67% of the blade span for this study. It was seen that the total pressure loss becomes higher in the region where the tip leakage vortex generated. The combined effect of the passage vortex and the tip leakage vortex enhances the pressure losses near the casing. The pressure losses were observed to be increased since the leakage vortex size is enlarged at higher Reynolds number and caused large disturbances to the main stream flow. On the other hand, at a low Reynolds number it was seen that the mass averaged exit flow angle decreases due to tip clearance flow interactions with the mainstream flow.

Rhee and Cho [18] investigated local heat/mass transfer characteristics on the near tip region of the rotating blade in a single stage low-speed annular cascade. Steady mass transfer coefficient was measured by using sublimation technique. This single turbine stage consisted of 16 stator vanes and rotor blades with a pitch of 34 mm and a chord length of 150 mm. The rotational effect was taken into account by considering the results obtained at design condition and for stationary blade. Off design condition was taken into account to investigate the effects with a range of incidence angle from -15 deg to 7 degrees. These incidence angles were achieved by changing the rotating speed with fixed inlet flow velocity. In this study, the heat transfer on the turbine rotor was also observed with significant change at different relative flow angle variations. In order to investigate heat and mass transfer characteristics on the blade surface, a non rotating case was considered and then used as a baseline data for comparing the results with the rotating case. The local heat transfer coefficient was seen affected by the presence of leakage vortex near the suction side, leakage flow acceleration due to high pressure gradient between the suction and pressure edge of the tip surface, formation of flow separation near the tip pressure surface as well as the flow mixing before the leakage flow immerging into the main stream region.

A numerical study was performed by Yang and Feng [19] to study the tip leakage flow and the heat transfer for a single stage rotor blade. This single stage was modeled for commercial GE-E engine. The simulations were performed for both flat tip and squealer type blade tip geometry at different clearance heights and depths of the squealer cavity. They performed the simulation using commercial CFD software CFX 5.7 and used mesh generation software ICEMCFD to generate structured O type grid around the blade surface and the tip clearance region to increase the grid resolution in order to achieve minimum y+ level. For the heat transfer analysis, a wall to inlet temperature ratio of 0.7 was used as an isothermal boundary condition for the wall surfaces. They observed significant variations in the results for different tip gaps- blade span ratios and groove depth-blade span ratios. For the flat tip case, they observed flow separation at the pressure side and reattachment on the tip surface where the leakage flow passed by the vertical flow separation. The leakage flow structure and the vortex pattern were seen different for the case of cavity or squealer tip surface. A vortex separation was seen on the pressure side of the cavity tip and then the flow enters into the cavity where it is trapped with large vortex formation. Due to this vortex formation the leakage flow reduction was observed to decrease up to 3% of the groove depth-blade span ratio. They also investigated the effect of tip gap heights on the flow structure inside the cavity. It was seen that the cavity vortex affected by the casing boundary layer if the blade span ratio is less than 1%. However, at a higher clearance the flow was seen highly dependent on the cavity depth. Heat transfer rate distribution for the flat tip case and squealer tip case was found completely different due to the change of flow structure for the modified tip geometry. Flat tip case exhibits higher heat transfer region in the pressure side and the blade leading edge, where the suction side region has shown lower heat transfer rate. On the other hand, squealer tip case showed higher heat transfer region on the bottom cavity surface because of the flow entering into the cavity and recirculates with reattachment on the bottom surface, thus, enhance the heat transfer rate. The existence of the hot spot was seen near the leading edge for the squealer tip cavity and the position of the hot spot moved towards the leading edge as the height of the cavity increases. From this study, it has been clearly indicated that the tip gap height has high influence to the heat transfer rate. If the clearance gap could be maintained same or below the boundary layer thickness developed on the casing surface, the overall heat transfer would decrease significantly.

Haller and Hilditch [20] conducted experiment on casing heat transfer of a high pressure turbine in a short duration isentropic light piston test facility and presented numerical predictions to compare experimental results. Data were recorded at three conditions, designed speed, speed reduced to 80% and a high pressure ratio. The heat transfer distributions were plotted at mid span of the rotor blade. Nusselt number exhibits higher at the leading edge due to flow stagnant at that location. However, the measured data showed high Nusselt number, further downstream, at 20% of axial distance from the leading edge. Conversely, the heat transfer was observed lower on the pressure surface which is quite reasonable, due to formation of thick boundary layer. In the span wise direction the trend of heat transfer distribution was seen similar for both pressure and suction surface.

A numerical work was performed by Loma et al. [21] and compared the predictions with experimental in CT3 type compression tube turbine test facility. In the experiment, a complete stage of 43 uncooled stator and 64 uncooled twisted blades was used, while the CFD simulation was conducted for 2 stator and 3 blade passages only. They tested at a rotor speed of 6500 RPM with a 5% inlet turbulence level. From the study, it was concluded that the steady heat transfer is influenced by the variation of the stage pressure ratio. High pressure ratio showed high heat transfer. However, heat transfer unsteadiness was seen to be affected by the stage loading. In addition to this, the heat transfer fluctuations caused by the presence of shock at the stator vane were observed around the blade and found two times larger at 15% chord than that at 85%.

2.2.2 Effect of Tip Geometry

Harvey and Ramsden [22] used partial shroud (winglet) with the blade tip instead of full shrouded blade in order to investigate over tip leakage flow. A steady flow RANS CFD code was used for this numerical study. They found that the presence of winglet at the blade tip significantly improves the efficiency by 1.2% to 1.8% of a highly loaded high pressure turbine at a tip gap of 2% of the span. At near trailing edge, vortices observed due to tip leakage flow and secondary flow mixing. It was concluded from this study that the major loss occurred due to mixing of tip leakage flow with the suction side free stream (reverse cross flow).

Aerodynamics of the tip leakage flow behavior was experimentally investigated by C. Camci et al. [23] using modified blade tip geometry of a single stage gas turbine engine. They considered two different tip geometries with a thin surface extruded from the tip in the spanwise direction called squealer rim, separately on both pressure and suction edge. A nominal tip clearance height of 0.8% of the blade span was used in the model. Their study revealed that the presence of the partial squealer rims greatly affect the tip leakage vortex, reduce its strength and size, thus, reduce the aerodynamic losses. The suction side squealer was found to be better in terms of aerodynamic influences than that of the pressure side squealer.

A numerical study was conducted by Saha et al. [24] to investigate the effect of pressure side blade tip geometry on the tip leakage flow and heat transfer. The calculations were performed for plain tip, full and partial tip with and without winglet. All the measurements were taken for an inlet pressure of 175.182 kPa and a temperature of 300 K where the outlet pressure was specified as atmospheric. It was observed that the leakage flow through the flat tip with pressure side winglet reduced significantly which reduces the heat transfer by 30%. In the presence of winglet, the pressure loss coefficient was reduced by 5% without affecting the average heat transfer coefficient. On the other hand, the suction side squealer with constant width winglet showed heat transfer reduction by 5.5% and pressure loss coefficient by 26% than that of flat tip case. However, combination of the squealer tip at the suction side and the winglet at the pressure side did not demonstrate any significant improvement in overall pressure loss coefficient and average heat transfer coefficient.

Kusterer et al. [25] investigated tip clearance loss reduction technique in an axial turbine by shaped design of the blade tip region. They developed multistage vane-rotor numerical model with new blade tip design. For this numerical simulation, RANS based CFD code CHTflow was used to predict the aerodynamics of two stage turbine. They used two different blade shapes with winglet type tip geometry that extends a constant width surface from the pressure side of the blade tip. With the change of tip geometry, the mass flow through the gap between the blade tip and the casing was reduced significantly. It was found that with modified tip and shape of the blade, the static polytrophic efficiency was increased by 0.092% and the leakage flow reduction for the first stage blade and the second stage blade were achieved 7.2% and 3.2%, respectively.

A numerical study was performed by Krishnobabu et al. [26] in order to study the effect of casing's relative motion on the characteristics of the tip leakage flow and heat transfer in an axial flow turbine. They used commercial CFD code CFX 5.6 for the computation using k-omega based Shear Stress Transport (SST) turbulence model. The predicted results for three different blade tip configurations were compared. It was seen that the relative motion of the casing for all geometries reduces the leakage flow mass transfer through the gap. Thus, the average heat transfer was reduced on the blade tip due to decrease in flow velocity. However, the squealer case showed further decrease in the average heat transfer coefficient than the case of plain tip geometry. This is caused by the drop in flow velocity results from flow circulation inside the squealer cavity and leakage vortex strength.

2.2.3 Combined Effect of Tip Geometry and Tip Clearance

Ameri et al. [27] conducted numerical study of rotor heat transfer and stage efficiency for a commercial gas turbine blade GE-E3. Three different configurations of the squealer tip geometry were investigated in their study. Simulations were performed using TRAF3D.MB CFD code which is designed for highly complex flow structure. Computational grid was made of hexahedral structured grid with the addition of C-type grid around the airfoil surface. The rotational speed of the rotor was set at 8450 rpm. The heat transfer analysis was made for a constant wall temperature of 70% of the inlet total temperature. Flow separation was appeared on the pressure side rim of the squealer cavity at 20% and 40% of the chord distance, while the height of the separation was seen to decrease near the trailing edge region due to higher flow acceleration. Moreover, there was an existence of a small vortex at the vicinity of the pressure side cavity and flow circulation within the cavity space. This flow circulation was act as flow blockage in the tip clearance region which, thereby, reduces the mass transfer through the gap. In addition to the aerodynamic study, the author investigated the heat transfer distributions on the tip surface for all the cases and found higher heat transfer region near the pressure side of the flat tip surface which was attributed to the leakage flow reattachment. In the squealer tip cavity case, the heat transfer coefficient was observed higher, from 10% to 80% of the axial chord length, near the pressure side cavity rim.

2.2.4 Effect of Film Cooling Injection

A novel technique of reducing the leakage flow by using cold air injection from the stationary casing was introduced by Thomas et al. [28]. In their study, flow injection and leakage flow interaction was analyzed experimentally. Air was injected from the casing from 10 holes spaced equally for a rotor pitch angle of 30^0. They also studied the effect of the injection parameter such as mass flow rate, hole size, location of the hole in different axial distance, on the rotor tip secondary flow structure. It was found that tip leakage vortex is greatly affected by the size and position of the injection holes. The leakage vortex moved to the suction side of the blade and reduced in size due to change in turbulence intensity level in the tip region. In addition, the effects of the position of the injection holes were also investigated at two different axial locations at 30% and 50% of the rotor. They found that the injection fluid takes the position inside the passage vortex which results in increased axial velocity and this effect was seen higher at the upstream region than the downstream. The author also achieved improved aerodynamic performance of the rotor by implementing new flow injection technique from the shroud, which increased the isentropic efficiency by 0.55 percent. In later study, they performed computational analysis of the effect of injection holes. They used MULTI3 solver for calculating unsteady compressible Reynolds Averaged Navier Stock equations. The film hole configurations, its positions and the size were modeled identical with their experimental test condition to perform CFD validation. The numerical results were found in well agreement with the experimental results from their study.

2.2.5 Stator-Rotor Unsteady

A number of studies have been devoted both numerically and experimentally to the study of stator-rotor interactions in the flow unsteadiness. Saxena et al. [29] experimentally studied the effect of inlet flow intensity and the wake passing period on the velocity unsteadiness inside the tip clearance region for different tip geometries. Inlet turbulent intensity causes low level velocity fluctuations. However, when the unsteady wake effect was included the velocity amplitude was seen to be higher and showed periodical behaviors.

He et al. [30] numerically observed an unsteady behavior of the pressure at both the suction and the pressure surfaces of the rotor. They used a transonic high pressure turbine stage model for the numerical simulation with a pressure ratio of 2.8 and a rotational speed of 9500 rpm. At the suction surface pressure unsteadiness was reported relatively higher than at the pressure surface along the chord which was attributed to the effect of the stator trailing edge shock and its propagation along the flow. The unsteady temperature fluctuations in the rotor mid span were also evident at different span of the rotor blades.

Molter et al. [31] conducted both numerical and experimental investigations on rotor tip aerodynamics and heat transfer. They used a commercial CFD solver STAR-CD for the numerical computations and compared the predictions with their measured data. Experimentally, they observed that the tip is exposed to about 25% higher heat load than that of the blade at 90% span. Their measurement also showed significant unsteady variations of heat load on the blade tip at the vane passing frequency, whereas the steady analysis couldn't capture that effect. It implies that the stator part has a strong interaction with the rotor flow field and causes unsteadiness of the flow and heat transfer in the rotor part. Steady CFD simulations generally over-predicted the overall heat flux by 10-25%, but captured the spatial heat flux trends well. Therefore, the time accurate analysis for a full turbine stage including both stator and rotor is required to fully understand the flow and heat transfer characteristics in the rotor blade tip clearance region.

The effects of stator rotor interactions on the flow unsteadiness were examined by Gaetani et al. [32] for a high pressure turbine stage. At a higher axial gap, between the stator and rotor, the upstream vortex shedding generated from the stator has shown little effect on the rotor flow field. However, at a nominal gap the rotor hub region was seen to be affected by the rotor incoming flow. From their study, it has been reported that for both axial gaps the region above 60% of the rotor span remains unaffected by the stator vortices and wakes. This is indicating that the flow physics in the tip clearance region can be well captured using steady CFD simulations.

The transport factors of the unsteady flow were investigated by Adami et al. [33] in a transonic turbine stage both by using in house numerical code and experiment. The stage was designed for 43 vanes and 64 blades with an operating pressure ratio of 3 and a speed of 6500 rpm. The level of static pressure fluctuations had been characterized by the rotor inlet Mach number. The fluctuations of the flow properties are higher at a higher Mach number than that at subsonic conditions. The largest variations of the flow field had been reported due to the effect of the shock that originates in the vane and propagates into the rotor section along with the flow.

Loma et al. [34] investigated the effect of strong shock in the heat transfer distribution of the transonic turbine stage. The experiments were performed for the range of maximum isentropic Mach number of 1.07 to 1.25. The data were presented at three spans (15%, 50%, and 85%) of the blade and mid span of the stator. In their study, a stage of 43 uncooled vanes and 64 blades were considered and the experiment was conducted in the compression tube turbine test facility. A highest heat transfer was observed at the vane leading edge due to thin boundary layer which offers less resistance to the heat flux. On the pressure and suction sides of the vane the boundary layer gets thicker and thus, reduces the heat transfer rate. The presence of shock at the vane trailing edge suddenly increases the heat transfer on the suction side of the neighbor blade. The instantaneous heat transfer rates showed two times higher in compared to time averaged data due to presence of shock in the vane trailing edge.

The effect of stator-rotor interaction was investigated by XIE et al. [35] for a 1.5 turbine stage numerically using their in house CFD code. The stage inlet pressure and temperature were specified as 7.3 bar and 536 K, respectively. The study was conducted with a rotating speed of 3000 rpm. At the leading edge of the blade, the instantaneous pressure was monitored in three spanwise locations. The amplitude of the pressure fluctuations due to upstream unsteady flow was observed maximum 0.4 bar. The fluctuating force on the rotor blade indicates the effect of the separated vortices inherited by the upstream vane wake.

2.3 Summary

Recently, the tip geometry configurations have been given more importance by the author to reduce the tip leakage flow with keeping optimum height of the clearance. In their studies [e.g. 6, 7, 9, 10, 15, 17, 23, 24], the flow structure for different tip geometries were investigated. However, less effort has been made to study, in details, the nature of the tip leakage flow as well as heat transfer under real turbine operating conditions.

On the other hand, many authors focused on turbine shroud heat transfer associated with tip leakage flow both in stationary and rotating cascade. For instance, reference number 4, 9, 10, 11, 12, 13, 14, 15, 18, 19, 20, 24, 26, 27 have studied turbine tip or shroud heat transfer under real or simple operating conditions including flat or modified tip geometries.

Moreover, a new technique of reducing tip leakage flow and corresponding heat transfer has been employed by using film cooling injections in the tip leakage region. Two possibilities of injecting cold air have been investigated either from the casing or from the blade tip surface as presented in the study by Newton et al. [9] and Thomas et al. [28].

Based on the literature review, the following key points could be summarized;

- The universal model of experimental turbine test facility or the numerical technique that could account all real conditions inside the engine, have not yet been developed. In some experimental study, the rotational effect has been focused but the main stream flow cannot be resembled as actual flow conditions inside the gas turbine engine since no combustions occurs before entering the stator section.
- Mass transfer rate of the leakage flow and the size of the leakage vortex are dependent on the tip gap heights. The larger clearance gap allows for higher mass transfer and thus, larger leakage vortices.
- Higher mass flow rate of leakage flow exhibits higher heat transfer on the blade tip and casing surface due to high temperature and velocity of the leakage flow.
- The tip leakage velocity is influenced by the change of Reynolds's number for the flat tip surface.

- In multistage stator-rotor study, the mean axial velocity in the first stage is reduced due to tip leakage flow. The development of the recirculation zone due to tip leakage flow changes the incidence angle to the second stage which affect on the flow structure, different than as seen in the first stage.
- Flow interaction between the stator exit and rotor inlet affect the rotor incoming flow near the hub region, however, rotor exit flow has been observed unaffected by the stator wakes and vortices.
- In rotating turbine blade studies, when the casing is set in relative motion to the blade, it develops the casing boundary layer that opposes the leakage flow and reduces the strength of the leakage vortex. The movement of the leakage flow is from pressure surface to the suction surface while the reverse cross flow moves in opposite direction, and this allows the leakage vortex to be remained in the suction side region.
- Development of the boundary layer at the blade tip surface and the casing significantly affects the heat transfer coefficient. Due to enhanced acceleration of the tip leakage flow results from the high pressure gradient between the pressure and suction side of the blade tip, the boundary layer thickness is reduced, thus, increases the heat transfer coefficient at the casing and tip surfaces.
- Suction and pressure side edge shows fluctuating heat transfer coefficient due to end wall effect. High heat load is observed at the blade leading edge where the flow stagnant, results in very thin boundary layer flow mostly laminar and gradually transformed in to turbulent.

- Turbulent intensity of the incoming flow and the upstream stator wakes have major contributions to the flow unsteadiness inside the rotor.
- The periodic movement of the rotor for each vane pass demonstrates fluctuating heat transfer distributions on the blade tip.
- The trailing edge shock, if any, at the vane migrating into the rotor section shows pressure fluctuations with respect to time. Presence of progressing shock waves also enhances blade tip heat transfer. However, as in the literature, this effect is more significant below rotor mid span and less near the casing.
- Mid camber of the blade tip found as the critical location of high heat transfer. However, it may vary depending upon the rotor tip characteristics parameter.

From the above statements, it is apparent that the tip clearance is a very critical region within the turbine stage and has been exposed to extream heat transfer conditions associated with the flow complexity which involves many other issues. Thus, it is imperative to investigate both the steady and unsteady nature of the flow field and heat transfer.

2.4 Objectives and Motivations

Many experimental works have been conducted by the researcher until now to explore the details of aerodynamics and heat transfer inside the gas turbine engine. Due to limitations in the experimental facility, most of the experiments have been performed under nonrealistic conditions such as low inlet/outlet pressure ratio, low inlet temperature, non rotating turbine blade which are far from the actual turbine operating condition. Chana and Jones [12, 13] conducted an experiment under real turbine operating conditions in an Isentropic light piston test facility. The author tested high pressure single stage turbine at an inlet temperature of 444 K and a rotor speed of 9500 rpm. The type of the turbine investigated for this experiment was MT1 which consisted of 32 vanes and 60 rotor blades. Initially, they imposed constant temperature at the inlet of the turbine stage and later the effect of variable temperature inlet conditions, results from uneven combustion inside the combustor, were taken into consideration in order to investigate its effect on turbine casing heat transfer and leakage flow.

Phutthavong et al. [36, 37] performed both steady and unsteady simulations of the blade tip leakage flow for the modeled gas turbine engine based on the study of Chana and Jones [12, 13]. An industrially owned CFD solver Nistar was used. They carried out CFD code validation and steady simulation in the first part while the second part was comprised of unsteady and parametric study. The commercial CFD software FLUENT was also used in their study as an attempt of heat transfer analysis for blade tip and casing. The Shear Stress Transport (SST) $k-\omega$ turbulence model was selected in order to capture the turbulence characteristics of the flow in the tip gap region. This numerical study mainly considered the tip leakage flow patterns in the tip clearance region. From their observation, it is seen that the shape and size of the flow separation varies with the time. However, detailed study of the leakage flow associated with the heat transfer distribution was not carried out. Hence, this work has been extended mainly for heat transfer distributions on the casing as well as blade tip with more details of the leakage flow structure in the clearance region.

In the earlier works, both numerical and experimental studies have been conducted using simplified flow conditions that are far from the real turbine operating state. To explain details phenomenon and nature of the turbine casing heat transfer in association with the complex turbine tip leakage flow, a further investigation is necessary considering rotational effect of the rotor under actual flow conditions, such as, high pressure ratio, high rotational speed, high inlet temperature, a complete stage, turbine blade curvature etc. at varying tip gap heights. Therefore, the objectives of this study are specified as follows:

- To investigate the heat transfer distributions and the leakage flow structures in the tip region for a plain tip surface at different heights of the clearance.
- To study the effect of inlet flow angle at different speeds of the rotor on the tip leakage flow field and heat transfer.
- To study both steady and unsteady behavior of the leakage flow and casing heat transfer.

Chapter 3

Numerical Methodology

The purpose of this numerical study is to investigate the heat transfer at the tip clearance region with various tip clearance heights and at different rotor speeds. Inside the gas turbine, the flow is turbulent and compressible. Therefore, the choice of an appropriate model is important for accurate and reliable predictions.

3.1 Governing Equations

3.1.1 Equations of Conservation (Mass, Momentum, Energy)

In this section, the governing equations of mass, momentum, and energy conservation are presented. For this numerical study, the flow through the turbine was considered as three dimensional, unsteady, viscous, turbulent and compressible. Ideal gas air was used as a working fluid whose properties i.e. density, thermal conductivity, dynamic viscosity and specific heat at constant pressure were set to linear function of temperature dependent variables. The differential form of unsteady conservation equations for flow and heat transfer can be written as:

Conservation of Mass:

The general compact form of the continuity equation is

$$\frac{\partial}{\partial t}(\rho)+\nabla\cdot\left(\rho\vec{U}\right)=0 \tag{3.1}$$

This equation can be expressed using the components of the velocity in three directions as follows,

$$\frac{\partial}{\partial t}(\rho)+\frac{\partial}{\partial x}(\rho u)+\frac{\partial}{\partial y}(\rho v)+\frac{\partial}{\partial z}(\rho w)=0 \qquad (3.2)$$

For steady,

$$\frac{\partial}{\partial x}(\rho u)+\frac{\partial}{\partial y}(\rho v)+\frac{\partial}{\partial z}(\rho w)=0 \qquad (3.3)$$

Conservation of Momentum:

The general compact form of the momentum equation can expressed as

$$\frac{D}{Dt}\left(\rho\vec{U}\right)=\nabla\cdot\sigma_{ij}+\rho g \qquad (3.4)$$

Where the substantial derivative is, $\frac{D}{Dt}(\ )=\frac{\partial}{\partial t}(\ )+u\frac{\partial}{\partial x}(\ )+v\frac{\partial}{\partial y}(\ )+w\frac{\partial}{\partial z}(\ )$, and in this numerical study, the gravity force (ρg) is neglected.

The momentum equation can be expressed in words as

Density × (Local acceleration + convective acceleration) = Pressure force per unit volume + viscous force per unit volume.

The following are the momentum equations by component,

X – Momentum,

$$\left(\frac{\partial}{\partial t}(\rho u)+u\frac{\partial}{\partial x}(\rho u)+v\frac{\partial}{\partial y}(\rho u)+w\frac{\partial}{\partial z}(\rho u)\right)=\left(\frac{\partial}{\partial x}(\sigma_{xx})+\frac{\partial}{\partial y}(\sigma_{yx})+\frac{\partial}{\partial z}(\sigma_{zx})\right)$$

(3.5)

Y – Momentum,

$$\left(\frac{\partial}{\partial t}(\rho v)+u\frac{\partial}{\partial x}(\rho v)+v\frac{\partial}{\partial y}(\rho v)+w\frac{\partial}{\partial z}(\rho v)\right)=\left(\frac{\partial}{\partial x}(\sigma_{xy})+\frac{\partial}{\partial y}(\sigma_{yy})+\frac{\partial}{\partial z}(\sigma_{zy})\right)$$

(3.6)

Z– Momentum,

$$\left(\frac{\partial}{\partial t}(\rho w)+u\frac{\partial}{\partial x}(\rho w)+v\frac{\partial}{\partial y}(\rho w)+w\frac{\partial}{\partial z}(\rho w)\right)=\left(\frac{\partial}{\partial x}(\sigma_{xz})+\frac{\partial}{\partial y}(\sigma_{yz})+\frac{\partial}{\partial z}(\sigma_{zz})\right) \tag{3.7}$$

Where, $\sigma_{xx}=-p-\frac{2}{3}\mu(\nabla\cdot\vec{U})+2\mu\frac{\partial}{\partial x}(u)$; $\sigma_{yy}=-p-\frac{2}{3}\mu(\nabla\cdot\vec{U})+2\mu\frac{\partial}{\partial y}(v)$;

$$\sigma_{zz}=-p-\frac{2}{3}\mu(\nabla\cdot\vec{U})+2\mu\frac{\partial}{\partial z}(w)$$

$$\sigma_{xy}=\sigma_{yx}=\mu\left(\frac{\partial}{\partial y}(u)+\frac{\partial}{\partial x}(v)\right);\quad \sigma_{xz}=\sigma_{zx}=\mu\left(\frac{\partial}{\partial x}(w)+\frac{\partial}{\partial z}(u)\right);$$

$$\sigma_{yz}=\sigma_{zy}=\mu\left(\frac{\partial}{\partial z}(v)+\frac{\partial}{\partial y}(w)\right)$$

Conservation of Energy:

$$\rho\frac{D}{Dt}(h)=\frac{D}{Dt}(p)+\nabla\cdot(\lambda\nabla T)+\Phi \tag{3.8}$$

Change of enthalpy of the system = work due to change of fluid volume + heat influx through the surroundings + mechanical energy dissipation.

Representation of Energy equation by components,

$$\frac{\partial}{\partial t}(\rho h)+u\frac{\partial}{\partial x}(\rho h)+v\frac{\partial}{\partial y}(\rho h)+w\frac{\partial}{\partial z}(\rho h)=\left(\frac{\partial}{\partial t}(p)+u\frac{\partial}{\partial x}(p)+v\frac{\partial}{\partial y}(p)+w\frac{\partial}{\partial z}(p)\right)+$$
$$\left(\frac{\partial}{\partial x}\left(\lambda\frac{\partial}{\partial x}(T)\right)+\frac{\partial}{\partial y}\left(\lambda\frac{\partial}{\partial y}(T)\right)+\frac{\partial}{\partial z}\left(\lambda\frac{\partial}{\partial z}(T)\right)\right)+\Phi \tag{3.9}$$

$$\text{Where, } \Phi = \mu \begin{bmatrix} 2\left(\frac{\partial u}{\partial x}\right)^2 + 2\left(\frac{\partial v}{\partial y}\right)^2 + 2\left(\frac{\partial w}{\partial z}\right)^2 + \left(\frac{\partial v}{\partial x} + \frac{\partial u}{\partial y}\right)^2 + \left(\frac{\partial w}{\partial y} + \frac{\partial v}{\partial z}\right)^2 + \left(\frac{\partial u}{\partial z} + \frac{\partial w}{\partial x}\right)^2 \\ -\frac{2}{3}\left(\frac{\partial u}{\partial x} + \frac{\partial v}{\partial y} + \frac{\partial w}{\partial w}\right)^2 \end{bmatrix}$$

3.2 Turbulence Modeling

3.2.1 Reynolds Averaged Navier-Stokes (RANS)

Turbulence consists of high frequency fluctuations in the flow field in time and space. It is a complex process where unsteady behavior of the flow is observed. The effect of turbulence is significant on the flow characteristics due to three dimensional, unsteady and chaotic natures. Turbulence is characterized by a high Reynold's number and is occurred when the inertia forces in the fluid becomes significant compared to viscous forces. General unsteady Navier-Stokes equations have been rearranged to Reynolds Averaged Navier Stokes equation by introducing averaged and fluctuating components. Hence, the instantaneous velocity components of turbulent flow are expressed as

$$u = \bar{u} + u'; \quad v = \bar{v} + v'; \quad w = \bar{w} + w' \tag{3.10}$$

Where, u', v' and w' are the fluctuating components of the velocity and $\bar{u}$, $\bar{v}$, $\bar{w}$ are the average components which can be further expressed as

$$\bar{u} = \frac{1}{\Delta t}\int_t^{t+\Delta t} u\,dt; \quad \bar{v} = \frac{1}{\Delta t}\int_t^{t+\Delta t} v\,dt; \quad \bar{w} = \frac{1}{\Delta t}\int_t^{t+\Delta t} w\,dt \tag{3.11}$$

The Reynolds Averaged Navier Stokes equations are then expressed as below,

Continuity

$$\frac{\partial}{\partial t}(\rho) + \frac{\partial}{\partial x}(\rho\bar{u}) + \frac{\partial}{\partial y}(\rho\bar{v}) + \frac{\partial}{\partial z}(\rho\bar{w}) = 0 \tag{3.12}$$

X – Momentum,

$$\left(\frac{\partial}{\partial t}(\rho\bar{u})+\bar{u}\frac{\partial}{\partial x}(\rho\bar{u})+\bar{v}\frac{\partial}{\partial y}(\rho\bar{u})+\bar{w}\frac{\partial}{\partial z}(\rho\bar{u})\right)=-\frac{\partial}{\partial x}(\bar{p})+\mu\nabla^2\bar{u}-\left(\frac{\partial}{\partial x}\left(\overline{\rho u'^2}\right)+\frac{\partial}{\partial y}\left(\overline{u'v'}\right)+\frac{\partial}{\partial z}\left(\overline{u'w'}\right)\right) \tag{3.13}$$

Y – Momentum,

$$\left(\frac{\partial}{\partial t}(\rho\bar{v})+\bar{u}\frac{\partial}{\partial x}(\rho\bar{v})+\bar{v}\frac{\partial}{\partial y}(\rho\bar{v})+\bar{w}\frac{\partial}{\partial z}(\rho\bar{v})\right)=-\frac{\partial}{\partial y}(\bar{p})+\mu\nabla^2\bar{v}-\left(\frac{\partial}{\partial x}\left(\overline{\rho u'v'}\right)+\frac{\partial}{\partial y}\left(\overline{v'^2}\right)+\frac{\partial}{\partial z}\left(\overline{v'w'}\right)\right) \tag{3.14}$$

Z– Momentum,

$$\begin{aligned}&\left(\frac{\partial}{\partial t}(\rho\bar{w})+\bar{u}\frac{\partial}{\partial x}(\rho\bar{w})+\bar{v}\frac{\partial}{\partial y}(\rho\bar{w})+\bar{w}\frac{\partial}{\partial z}(\rho\bar{w})\right)=\\&-\frac{\partial}{\partial z}(\bar{p})+\mu\nabla^2\bar{w}-\left(\frac{\partial}{\partial x}\left(\overline{\rho u'w'}\right)+\frac{\partial}{\partial y}\left(\overline{\rho v'w'}\right)+\frac{\partial}{\partial z}\left(\overline{\rho w'^2}\right)\right)\end{aligned} \tag{3.15}$$

The Reynolds Averaged Energy Equation is given in the following form,

$$\begin{aligned}&\frac{\partial}{\partial t}\left(\rho\bar{h}\right)+\bar{u}\frac{\partial}{\partial x}\left(\rho\bar{h}\right)+\bar{v}\frac{\partial}{\partial y}\left(\rho\bar{h}\right)+\bar{w}\frac{\partial}{\partial z}\left(\rho\bar{h}\right)=\left(\frac{\partial}{\partial t}(\bar{p})+\bar{u}\frac{\partial}{\partial x}(\bar{p})+\bar{v}\frac{\partial}{\partial y}(p)+\bar{w}\frac{\partial}{\partial z}(\bar{p})\right)+\\&\left(\frac{\partial}{\partial x}\left(\lambda\frac{\partial}{\partial x}(T)\right)+\frac{\partial}{\partial y}\left(\lambda\frac{\partial}{\partial y}(T)\right)+\frac{\partial}{\partial z}\left(\lambda\frac{\partial}{\partial z}(T)\right)\right)-\left(\frac{\partial}{\partial x}\left(\overline{\rho u'h'}\right)+\frac{\partial}{\partial y}\left(\overline{\rho v'h'}\right)+\frac{\partial}{\partial z}\left(\overline{\rho w'h'}\right)\right)\end{aligned} \tag{3.16}$$

The momentum equation containing terms $\overline{\rho u'^2}$, $\overline{\rho v'^2}$, $\overline{\rho w'^2}$, $\overline{\rho u'v'}$, $\overline{\rho u'w'}$, $\overline{\rho v'w'}$ are called Reynolds stresses. On the other hand, in the energy equation an additional terms arises ($\overline{\rho u'h'}$, $\overline{\rho v'h'}$, $\overline{\rho w'h'}$) that are called Reynolds flux. These terms arises due to turbulent velocity fluctuations and thermal fluctuations. For unsteady flow conditions, these equations allow the solver to be solved numerically. Sometimes, for unsteady numerical simulation, all these equitation's termed as URANS (Unsteady Reynolds Averaged Navier Stokes equations).

3.2.2 The k-omega and SST Models

In CFD analysis selection of an appropriate turbulence model is highly important to predict the boundary layer effect near the wall zone precisely. It is seen that for numerical simulation, in general, the standard $k-\omega$ turbulence model is widely used for some reasonable reason in CFD analysis which is a two equation model that includes two extra transport equations to represent the turbulent properties of the flow. The $k-\omega$ based SST model has now been widely used for external and internal flow, for example, axial flow turbine, flow over an airfoil etc. It accounts for the transport of the turbulent shear stress and provide accurate numerical prediction of the flow separation under adverse pressure gradients. The performance of this model has been validated by several studies and well recommended to use in order to simulate boundary layer simulation with high accuracy [4, 26]. Therefore, in this present study $k-\omega$ based SST turbulence model is adopted to conduct numerical calculations.

The two equation $k-\omega$ model was first developed by Wilcox [38]. This model assumes that the viscosity is linked with the turbulent kinetic energy (k) and turbulent frequency (ω).Later, the Wilcox's formulated model was modified due to significant variations of the results observed for a specified value of ω at the inlet. This problem was overcome by Mentor [39] by implementing blending function into $k-\varepsilon$ and $k-\omega$ model and named as baseline $k-\omega$ model. In the transformed model, the $k-\varepsilon$ model works in the free stream region while the $k-\omega$ model is applied inside the boundary layer. The transport equations after implementing the blending function (F_1) can be expressed as below,

k-Equation

$$\frac{D(\rho k)}{Dt} = P_k - \beta' \rho k \omega + \nabla \cdot [(\mu + \sigma_k \mu_t) \nabla k] \tag{3.17}$$

ω-Equation

$$\frac{D(\rho\omega)}{Dt} = \alpha \rho S^2 - \beta \rho \omega^2 + \nabla \cdot [(\mu + \sigma_\omega \mu_t) \nabla \omega] + 2(1-F_1)\rho \frac{\sigma_{\omega 2}}{\omega} \nabla k \nabla \omega \tag{3.18}$$

P_k is the turbulence production rate which is given by

$$P_k = \mu_t \frac{\partial \overline{U_i}}{\partial x_j}\left(\frac{\partial \overline{U_i}}{\partial x_j} + \frac{\partial \overline{U_j}}{\partial x_i}\right) \rightarrow \widetilde{P}_k = \min(P_k, 10 \cdot \beta' \rho k \omega)$$

The term blending function (F$_1$) is calculated using the flow variables and distance to the nearest wall (y) and expressed as

$$F_1 = \tanh(\arg_1{}^4)$$

$$\arg_1 = \min(\max(\frac{\sqrt{k}}{\beta' \omega y}, \frac{500\upsilon}{y^2 \omega}), \frac{4\sigma_{\omega 2} \rho k}{CD_{kw} y^2}) \tag{3.19}$$

where y is the near wall distance and ν is the kinematic viscosity.

The following is the illustrations of term included in Eqn. 3.19.

$$CD_{k\omega} = \max(2\rho\sigma_{\omega 2} \frac{1}{\omega} \nabla k \nabla \omega, 1.0 \times 10^{-10}) \tag{3.20}$$

The major advantage of $k-\omega$ based SST model is the accuracy in predictions and capable of capturing flow separation caused by the adverse pressure gradient. In order to achieve proper transport properties, a limiter is introduced with the turbulent viscosity (μ_t) formulation as shown below.

$$\mu_t = \frac{\rho a_1 k}{\max(a_1 \omega, SF_2)} \tag{3.21}$$

Here, S is the magnitude of the strain rate. F$_2$ is a second blending function defined by

$$F_2 = \tanh(\arg_2{}^2) \text{ with} \tag{3.22}$$

$$\arg_2 = \max(\frac{2\sqrt{k}}{\beta' \omega y}, \frac{500\upsilon}{y^2 \omega}) \tag{3.23}$$

All constants are calculated from the corresponding constants of the $k-\varepsilon$ and $k-\omega$ models through following expression,

$$\alpha = \alpha_1 F + \alpha_2 (1-F) \tag{3.24}$$

The model constants are

	F=1, near the wall ($k-\omega$)				F=0, far from the wall ($k-\varepsilon$)			
β'	α_1	β_1	σ_{k1}	$\sigma_{\omega 1}$	α_2	β_2	σ_{k2}	$\sigma_{\omega 2}$
0.09	0.555	0.075	0.85	0.5	0.44	0.0828	1	0.856

Where, 1 in the subscript stands for the constants of $k-\omega$ model and 2 for $k-\varepsilon$ model.

3.3 Near Wall Treatment

3.3.1 Automatic Near-Wall Treatment for Omega-Based Models

When a fluid flows over a surface, a boundary layer develops with a velocity gradient zero at the wall to free stream velocity. Inside the boundary layer, there exists three distinct regions, called laminar, buffer and turbulent. All these regions are characterized by the flow interactions with the wall surface that develops different levels of shear stresses caused by fluid's viscosity. In real condition, this boundary layer property has major consequences on the heat transfer distributions. Therefore, for precise heat transfer predictions through numerical calculations, it is highly important to resolve accurately all boundary layer properties.

In order to capture the flow physics in the boundary layer region, the grids are refined enough to ensure sufficient number of nodes allocated near the wall boundary. Commercial CFD solver ANSYS CFX can model appropriately near wall region where SST $k-\omega$ model is used to account fluid layer shear caused by the viscosity effect. In order to facilitate computational effort with additional accuracy, an automatic wall function [Appendix A] is used to attain minimum value of the nondimensional wall distance (y+) for SST $k-\omega$ model. It should be noted here that the acceptable range of y+ value is less than 200 if the automatic wall function is enabled for SST $k-\omega$ model in CFX.

3.3.2. Heat Flux in the Near-wall region:

Heat transfer rate across the wall is characterized by the temperature differences between the wall and wall adjacent fluid. For heat transfer calculation, the thermal boundary layer is modeled using the thermal law-of-the-wall function given by Kader [40].

CFX solver allows wall function approach or automatic wall treatment in calculating heat flux at the wall. A non-dimensional near-wall temperature profile can be plotted in the viscous sublayer and the logarithmic region which is defined as:

$$T^+ = \frac{\rho C_p u^* (T_w - T_f)}{q_w} \tag{3.25}$$

where T_w is the temperature at the wall, T_f near-wall fluid temperature, C_p fluid heat capacity and q_w the heat flux at the wall.

The non-dimensional temperature distribution is therefore modeled as:

$$T^+ = \Pr y^* e^{-\Gamma} + \left[2.12\ln(y^*) + \beta\right] e^{(-1/\Gamma)} \tag{3.26}$$

Where $\beta = (3.85\Pr^{1/3} - 1.3)^2 + 2.12\ln(\Pr)$

$$\Gamma = \frac{0.01(\Pr y^*)^4}{1 + 5\Pr^3 y^*} \tag{3.27}$$

Pr is the fluid Prandtl number and is given by:

$$\Pr = \frac{\mu C_p}{\lambda} \tag{3.28}$$

where λ is fluid thermal conductivity

The wall heat flux model is then takes the simple form as:

$$q_w = \frac{\rho C_p u^*}{T^+}(T_w - T_f) \tag{3.29}$$

3.4 Alternate Rotation Model

For the flow with rotating frame of reference, solver uses absolute frame of reference instead by employing alternate rotation model to account advection term in the momentum equations. The alternate rotation model reduces numerical error when the flow is constant in absolute frame and parallel to the axis of rotation. The advection term models the velocity in relative frame in the momentum equation and is given by:

$$\frac{D}{Dt}(\rho U) = -\nabla p + \nabla \cdot \sigma_{ij} - \rho\Omega \times U - \rho\Omega \times (\Omega \times r) \tag{3.30}$$

where the term $\rho\Omega \times U$ is called the coriollis component of the force.

3.5 Mixing Plane Modeling and the Interface Model

3.5.1 General Connection Interface Model

The interface between the rotor and the stator domain is coupled through general connection interface model provided by CFX in order to allow frame transformation across the interface. During the unsteady simulation, this model is used to apply unsteady sliding interfaces between the domains and can connect non-matching grid. This option accounts for the stationary frame of reference in one side and rotating frame of reference in the other side and pitch changes across the interface. While setting the problem, the general connection model is selected along with mixing model and pitch change option.

3.5.2 Frame Change/Mixing Model

3.5.2.1 Stage Model for Steady Simulation

Steady state solution is obtained by employing "Stage" model (mixing model) at the interface between the rotor and stator domain. The main idea of this mixing model is averaging the fluxes circumferentially at the interface. This model allows performing steady state prediction for the single or multi stage components. The flow data is averaged out at the upstream of the interface which is stationary part of the domain and used as inlet boundary condition for the downstream rotor component. It accounts for the circumferential average and steady interaction between the domain interfaces; however, the unsteady interaction is neglected.

3.5.2.2 Unsteady Rotor-Stator Model for Unsteady Simulation

In order to run unsteady simulation the frame change model is switched to unsteady "Rotor-Stator" model to allow sliding movement of the rotor domain with respect to the time interval. This model accounts the unsteady interaction effect at the sliding interface between the components that are in motion relative to each other. It should be noted here that during the unsteady simulation the relative position of the grids on either sides of the interface is changed, therefore, updates the interface position at each time step. The initial condition for unsteady simulation is taken from the steady simulation. A total of forty time steps were used for a single pass of the stator pitch where each time step consisted of twenty sub iterations for the solutions to be reasonably converged.

3.6 Turbine Modeling

In this study a single stage turbine, as shown in Fig. 3.1, has been modeled and simulated using commercial CFD code ANSYS CFX R-11. Here, High resolution second order central difference scheme for the space and second order backward Euler scheme for the time were used to discretize the flow, turbulent kinetic energy, and specific dissipation rate. The SST $k-\omega$ turbulence model was used to resolve flow turbulence. Ideal gas air was used as a working fluid that obeys the perfect gas law and properties of the gas i.e. density, thermal conductivity, dynamic viscosity and specific heat at constant pressure were set to be the linear function of temperature dependent variable.

The turbine stage geometry consisting of one vane and two rotor blades (Fig. 3.2) were generated using three different geometric software Catia version 4, Gambit and ICEM CFD tools. After ensuring proper geometry, the grid was generated by using ICEM CFD grid generation tools. An unstructured tetrahedral grid, with proper attention to the interested region, was adopted for meshing both rotor and stator domain, as shown in the Figs. 3.3, 3.4 and 3.5, in different cross-sectional plains. Near the wall surface, grid clustering were performed by introducing several prism layers in order to accurately capture the flow physics and heat transfer. A detailed statistics of the grid structure for the rotor section, as of interest, is shown in the Table 3.1. Sufficient number of nodes and cells were distributed on the casing (Fig. 3.6) at the projections of the blade tip surface and within the tip clearance region to ensure dimensionless wall distance (y+) bellow 200 as recommended to use for the SST $k-\omega$ model with automatic wall function provided in CFX. For both rotor and stator domain, a total of ten to twenty prism layers were placed at the wall surfaces in order to resolve the flow condition as accurately as possible.

Proper boundary conditions were applied with consideration to the reference experimental works conducted by Chana and Jones [12, 13]. The computational domain for the stator and the rotor with imposed boundary conditions is shown in Fig. 3.7. At the inlet of the stator domain, a total pressure of 4.6 bar and a total temperature of 444 K were specified while static pressure of 1.46 bar at the rotor domain outlet was set to satisfy experimental static pressure of 1.43 bar at the rotor exit. The boundary condition details are presented in Table 3.2. For both steady and unsteady simulation, rotational periodic boundary conditions were imposed on the periodic surfaces in order to model minimum number of vane and blade passages. In numerical simulation, it is always desirable to use pitch ratio unity which was ensured by modeling 1:2 vane and blade ratio, yielding a pitch angle of 12^0 for each of the domain. It is important to note that in Chana and Jone's work, a stator with 32 vanes was used, while the rotor consisted of the 60 blades. In order to achieve equal pitch angle the geometry was scaled to 30 vanes and 60 blades for this present study. The basic shape of the airfoil and the flow path for turbine stage was obtained from the available figures in Chana and Jone's work in the open literature. In addition, the tip clearance height for the baseline case was considered as 1.2 mm [36, 37].

In the present study, at first, steady simulations were performed for all cases and allowed to run up to 500 iterations to reach the residuals well below 10^{-4} for continuity, momentum, heat transfer, and turbulence. Convergence of different parameters such as mass flow rate, total pressure, static pressure at different location of the domain were also monitored and remained constant over this large number of iterations. For the unsteady simulations, converged steady state solutions were used as the initial condition and it was run for forty time steps for the total time taken by the rotor to pass through single stator pitch. Details of the unsteady validations in regard to the time steps, number of vane pass; number of sub iteration can be seen in chapter 5.

3.7 Grid Independency

For the grid independency test, two approaches are conducted to select appropriate grid system in order that all phenomena are fully captured in that small tip gap region. Firstly, the velocity and temperature (Fig. 3.8) profiles are compared for different number of cells distributed radially in the tip clearance region (e.g. 20, 35, 45, 60 cells along the tip gap). Secondly, pressure distributions (Fig. 3.9) at the rotor mid span compared for fine and course grid of 4 and 2.8 million cells, respectively. Based on these results it may be concluded here that the converged solution can be obtained from the grid system of 2.8 million cells with 45 cells in the tip gap.

3.8 Test Matrix

For both steady and unsteady simulations, a total of ten cases were considered, as shown in the test matrix in Table 3.3 and Table 3.4, respectively. In the baseline case, a tip clearance of 1.2 mm, uniform temperature of 444 K, and a rotational speed of 9500 rpm, as that of experiment, were chosen. The effects of the clearance heights were investigated by considering three gap sizes of 0.6 mm, 1.2 mm and 2 mm that are respectively, 1%, 3% and 5% of the blade span. In addition to that, rotational speed of the rotor at design and off design speeds of 12500 rpm and 15500 rpm, respectively, were chosen for steady simulation whereas in unsteady case the higher speed was restricted to 13125 RPM due to convergence problem with the solver for 15500 RPM speed.

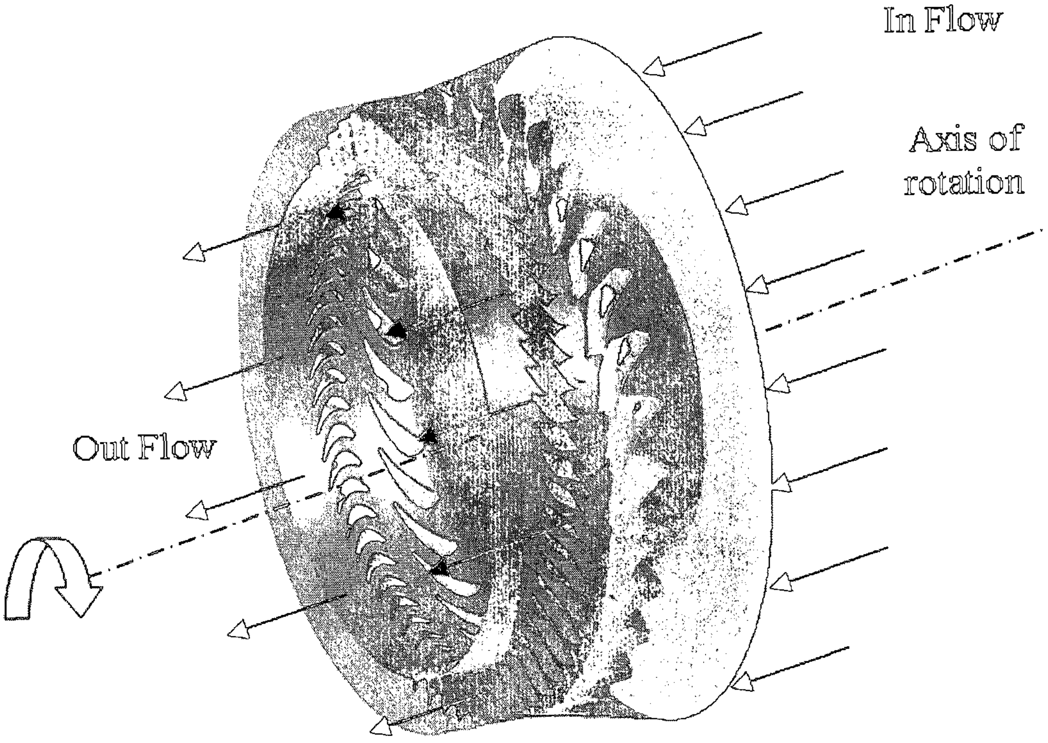

Figure 3.1 Complete turbine stage configuration.

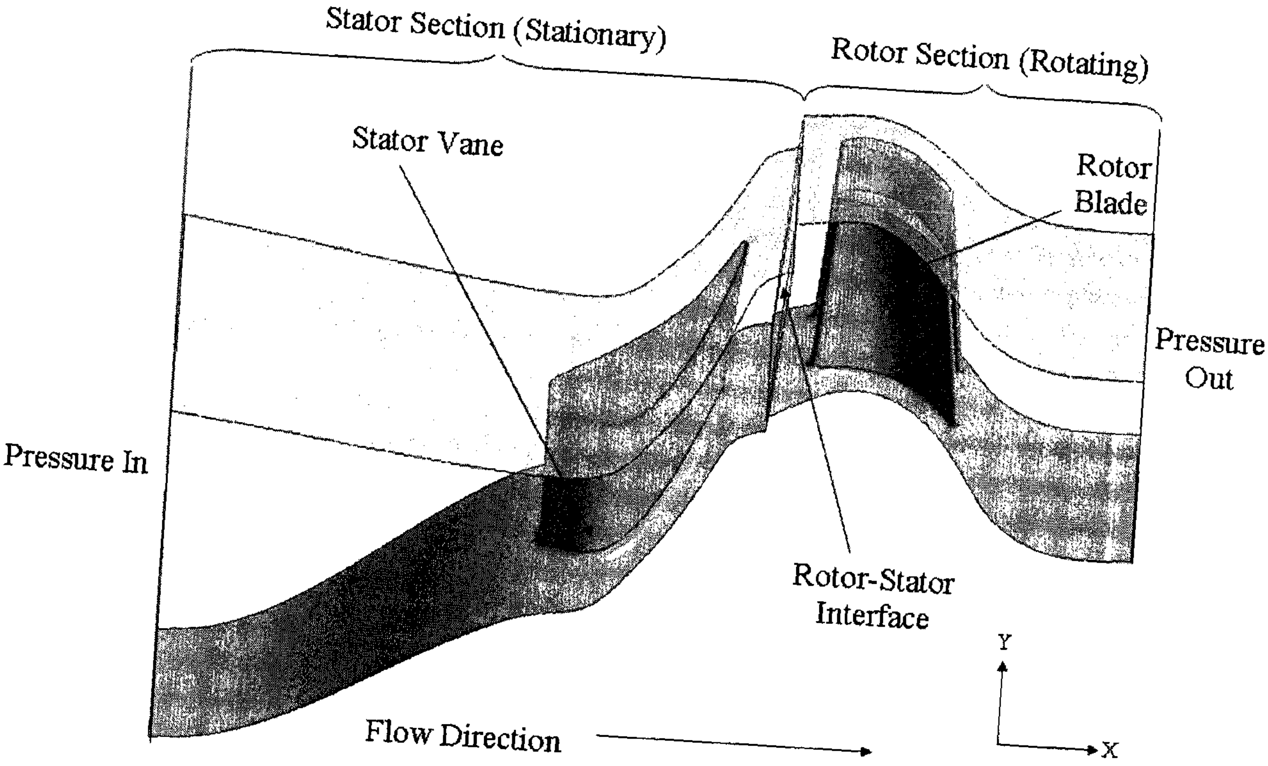

Figure 3.2 Single stage stator-rotor domain with boundary conditions.

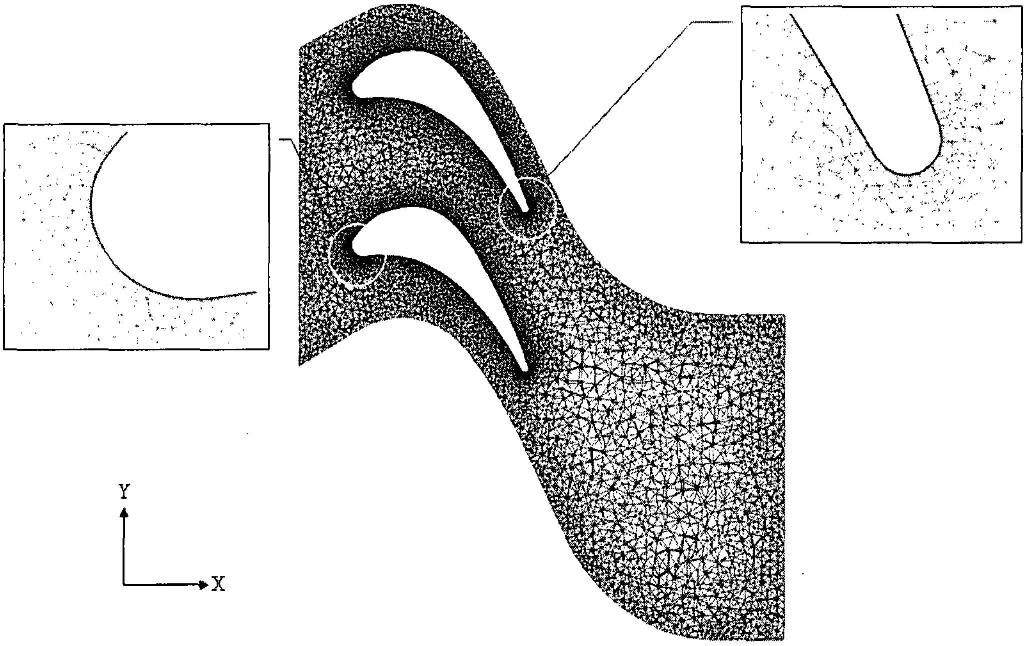

Figure 3.3 Radial cross-section of the rotor section at the mid span.

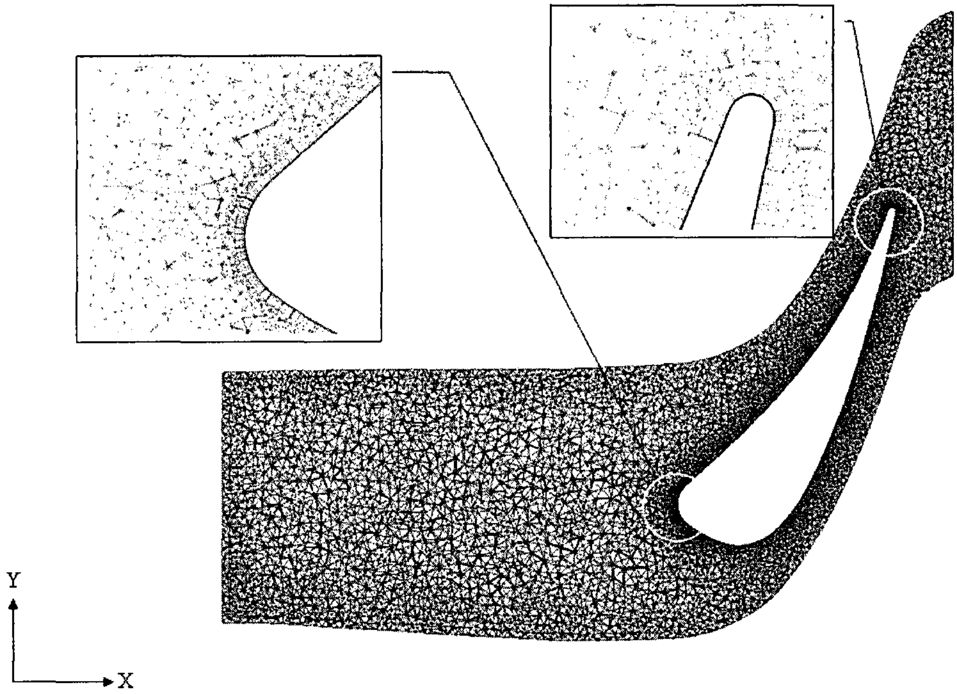

Figure 3.4 Radial cross-section of the stator section at the mid span.

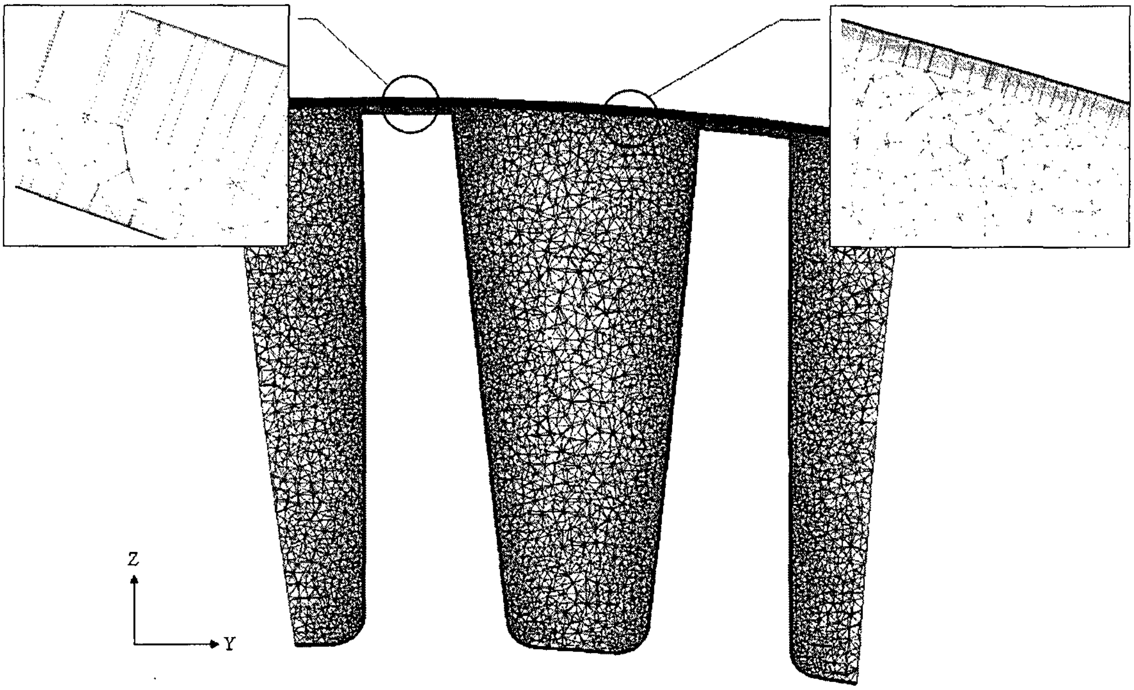

Figure 3.5 Axial cross-section of the rotor section showing grid at Tip and Casing.

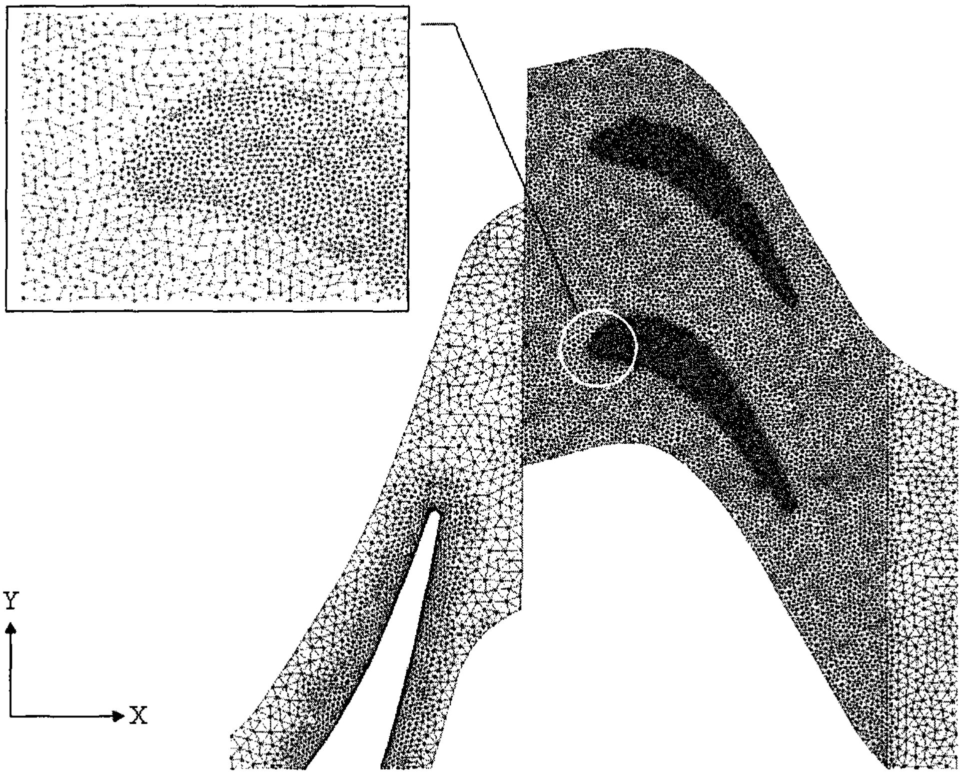

Figure 3.6 Grid distributions on the stator and rotor casing showing fine grid at the blade tip projections on the rotor casing.

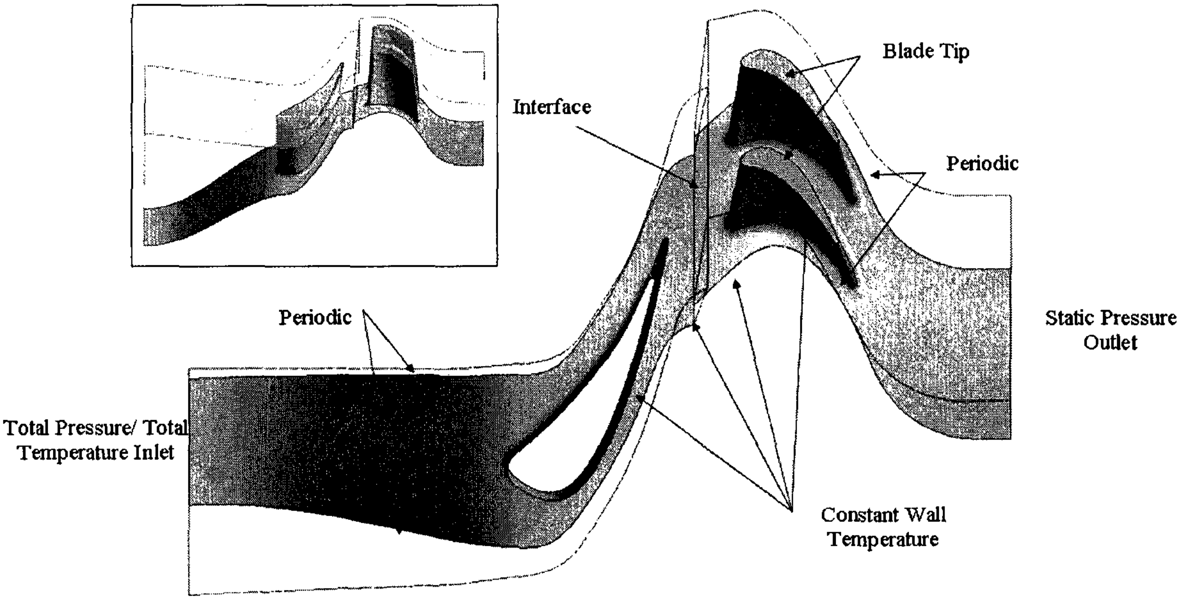

Figure 3.7 Single stage stator-rotor domain without outer walls.

Table 3.1 Statistics of computational grid

Mesh Information (For the Rotor Section)			
	0.6 mm Case	1.2 mm Case	2 mm Case
Number of elements (Million)	3.7	3.23	3.4
Number of cells from tip to casing	30	45	45

Table 3.2 Turbine geometrical and operational parameter

Test Conditions			
Blade tip geometry	Flat Tip	Uniform total inlet temperature case, K	444
Tip clearance, mm	0.6	Inlet turbulence intensity	Medium, 5%
	1.2		
	2	Stator inlet total pressure, bar	4.6
Single stage	One stator-Two rotor	Static pressure outlet, bar	1.46
Stage designed for	30 Stator	Angular speed, RPM	9500
	60 Rotor		12500
Length of stator in x-direction, m	0.12		15500/13125
Length of rotor in x-direction, m	0.075	Wall to inlet temperature ratio	0.5

Table 3.3 Test matrix for steady simulation

TEST MATRIX (Flat Tip)	Case Number	Tip Clearance, mm	Stator Inlet Temperature, K	Speed, RPM
Effect of Tip Clearance	Baseline	1.2	444	9500
	1	0.6		
	2	2		
Effect of Rotor Angular Velocity	3	1.2		12500
	4			15500

Table 3.4 Test matrix for unsteady simulation

TEST MATRIX (Flat Tip)	Case Number	Tip Clearance, mm	Stator Inlet Temperature, K	Speed, RPM
Effect of Tip Clearance	Baseline	1.2	444	9500
	1	0.6		
	2	2		
Effect of Rotor Angular Velocity	3	1.2		12500
	4			13125

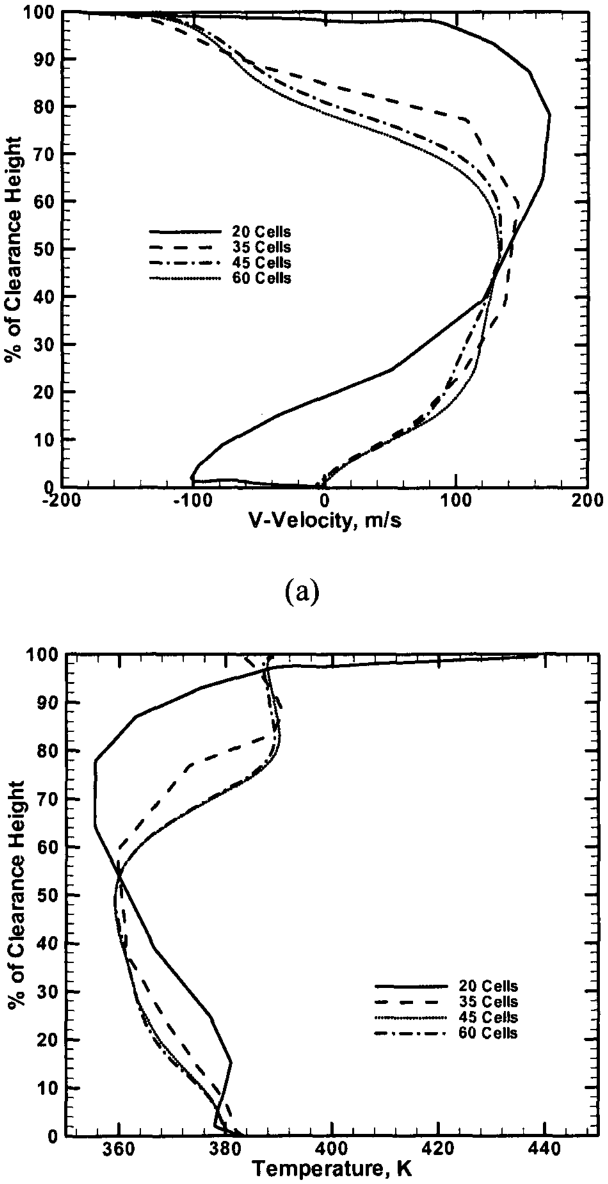

(a)

(b)

Figure 3.8 Effect of number of cells inside the tip clearance region for (a) V-velocity profile and (b) Static temperature profile at a location, $x / C_x = 50\%$, $y / t_y = 45\%$.

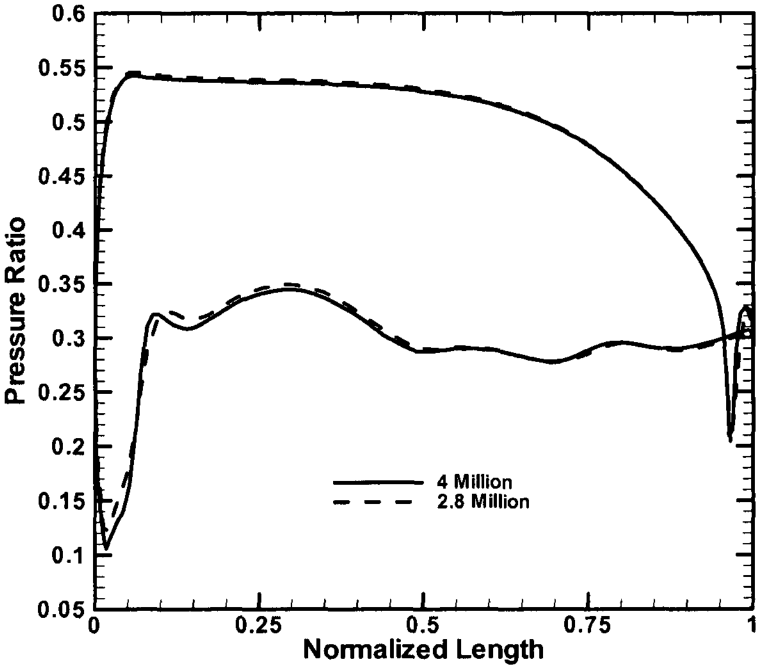

Figure 3.9 Effect of grid size in the rotor blade mid passage.

Chapter 4

Steady Simulation and Analysis

In the following sections, predictions of steady simulations will be validated using the experimental data of Chana and Jones [12, 13], Hilditch et al. [42], and numerical predictions of Roux et al. [41] will be discussed in detail, as will possible reasons for any discrepancies. All steady simulations were performed with boundary conditions similar to the experimental operating conditions of the work of Chana and Jones [12, 13]. The steady state predictions will then be analyzed in detail in order to explain the real physical condition associated with the tip clearance region of the gas turbine engine.

4.1 Computational Details

In the present study, the turbine model was simulated using commercial CFD (Computational Fluid Dynamics) solver ANSYS CFX R.11. A high resolution second order central difference scheme was used to descretize the equations for the flow, turbulent kinetic energy, and specific dissipation rate with automatic wall function provided by the software. Wall function is the empirical method of resolving a boundary layer profile near the wall, regardless of the number of nodes present near the wall zone. Grid resolutions near the wall were examined by maintaining a recommended value of dimensionless wall distance (y+) below 200 for SST $k-\omega$ model with automatic wall function. In CFX, the smooth transition to the wall function is ensured by an automatic option without any loss of accuracy. Krishnababu et al. [25] compared the predictions of tip leakage flow and heat transfer using CFX solver with turbulence models: $k-\varepsilon$, $k-\omega$, and SST $k-\omega$ models. It was found that the SST $k-\omega$ model shows the best agreement with the experimental data. Thus, the SST $k-\omega$ turbulence model was selected for turbulence closure in this study. Air, an ideal gas, was used as the working fluid. As mentioned, for this steady run, the properties of the gas (i.e. density, thermal conductivity, dynamic viscosity and specific heat at constant pressure) were set to be a linear function of the temperature.

As previously discussed, for convenience, the turbine stage was modeled using 30 vanes and 60 blades, in order to achieve equal pitch angle. The vane is tapered with a 73 degree exit angle. The blade is tapered and twisted within the design criteria of the typical turbine blade. The global length of the modeled turbine is similar to that of Chana and Jones [12, 13]. The details of the turbine geometry, however, are not available in their publications. Note that the number of vanes in the stator was 32, and the rotor consisted of 60 blades in Chana and Jone's work. Boundary and operating conditions based on the experimental works of Chana and Jones [12, 13] were applied for qualitative comparison (see Table 3.2).

Steady simulations with stage model at the vane-blade interface were performed for all cases, and were allowed to run up to 500 iterations to reach at least the three orders reduction of the residuals for continuity, momentum, heat transfer, and turbulence. Convergence of various parameters, such as mass flow rate, total pressure and static pressure at different locations along the domain were also monitored and remained constant over a large number of iterations. Stage model in ANSYS CFX performs a circumferential averaging of the fluxes at the interface upstream in the stationary frame of reference and then applies circumferential averaging to the interface downstream, as inlet flow condition for the rotating frame of reference. All simulations were performed in parallel processing environment, and consisted of 10 processors on the HP cluster. The simulation time was approximately 11 hours, and convergence was achieved within 500 iterations.

4.2 Comparison with Experimental Data

For CFD (Computational Fluid Dynamics) code validation, comparisons with experiments (Chana and Jones, 12, 13) were conducted. Values of the isentropic Mach number at the stator exit casing and hub were compared with experimental data, as were the values of relative total pressure at the rotor inlet (see Table 4.1). Although the stator section was modeled using 30 vanes instead of 32 vanes, the present modeled vane has a larger exit angle and narrower throat area based on the vane profile at the mid span. The present vane, therefore, has a higher Mach number at the exit than those of experiments (Chana and Jones, 12, 13).

The distribution of the adiabatic wall temperature on the casing surface is depicted in Fig. 4.1. It should be mentioned here that the wall temperature and surface heat transfer were measured experimentally by Chana and Jones (12, 13), and the adiabatic wall temperature was then calculated by using these values. The uncertainty of the adiabatic

Table 4.1 Comparison with experiment

Parameter/Location	Prediction (Adiabatic)	Experimental by Chana and Jones
Isentropic mach number at NGV exit (hub)	1.24	1.034
Isentropic mach number at NGV exit (casing)	1.0665	0.925
Relative total pressure at Rotor inlet, bar	2.571	2.7

wall temperature was assessed to be 10 degrees. The The adiabatic wall temperatures along a row of gages showed a sudden drop at 58% of the axial chord. This was attributed to the effect of the trailing edge shock waves of the vane. In order to capture the effect of the upstream vane and the trailing edge shock on the downstream rotor blade, the unsteady simulation should be performed without averaging the fluxes at the interface of the vane and blade. The circumferentially averaged adiabatic wall temperature prediction shows wall temperature variations, where the temperature drops from 430K to 350K, indicating work extraction across the rotor. The predicted pressure distributions are also found to be in reasonable agreement with experimental data as presented in Fig. 4.2. In the experimental work of Chana and Jones [12, 13] and Hilditch et al. [42], a bump in the pressure distribution (near the vane trailing edge) resulting from the shock also appeared in similar vane geometry and test conditions. In 2001, Roux et al. [41] numerically observed the existence of the trailing edge shock in the stator section for similar geometric configurations. However, the predicted location is slightly shifted to the trailing edge (Fig. 4.2a). In the present study, this trailing edge shock is under predicted with higher discrepancies (Fig. 4.2a) that might be attributed to the effect of vane geometry, number of vane counts, and/or the effect of the computational method of the CFD solver. When the flow enters the rotor section, it flows with a higher positive flow incidence caused by the stator vane, resulting in a high pressure gradient at the suction side of the leading edge, normal to the airfoil surface. As a result, the flow is separated from the blade wall at the suction side near the leading edge (Fig. 4.2b). The discrepancies in pressure distributions are not significant at all other locations. Based on the comparisons of the CFD prediction and the experiment, it may be stated that the gas

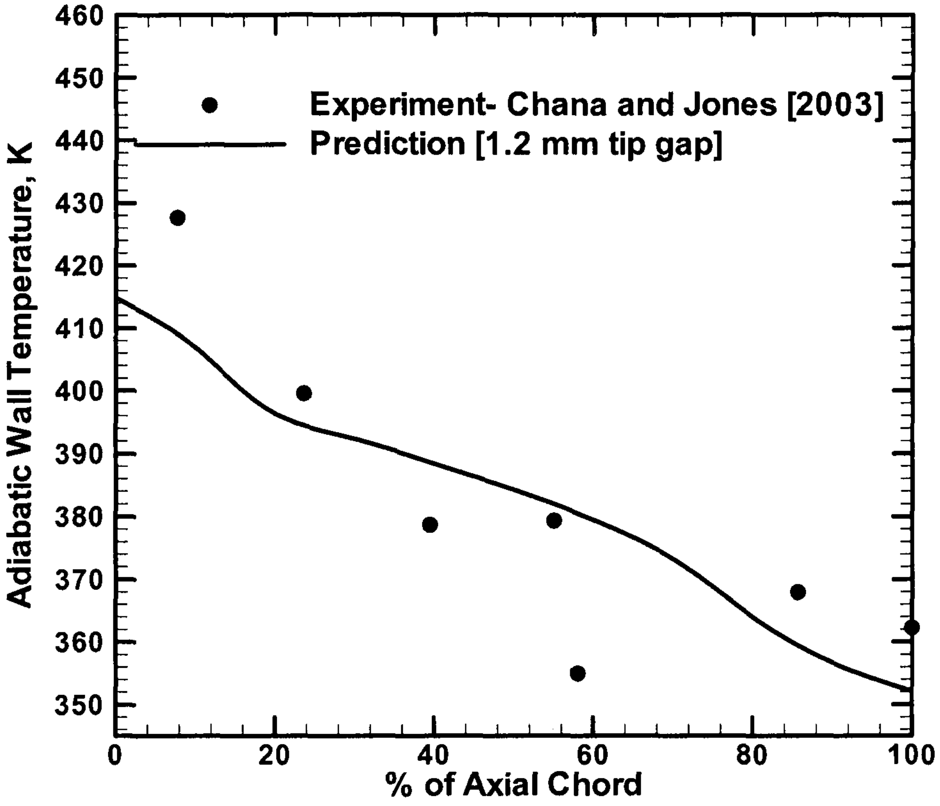

Figure 4.1 Comparison of adiabatic wall temperature averaged circumferentially on the casing from blade tip leading to trailing edge projections.

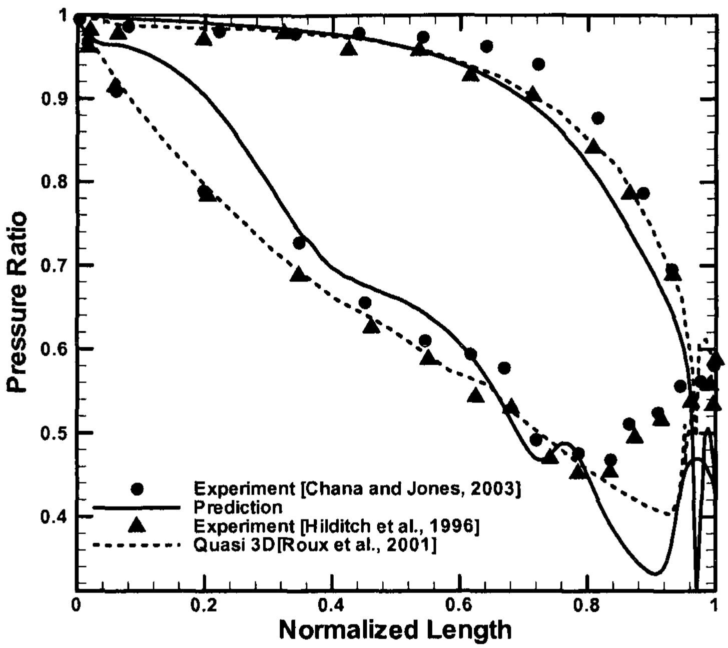

(a)

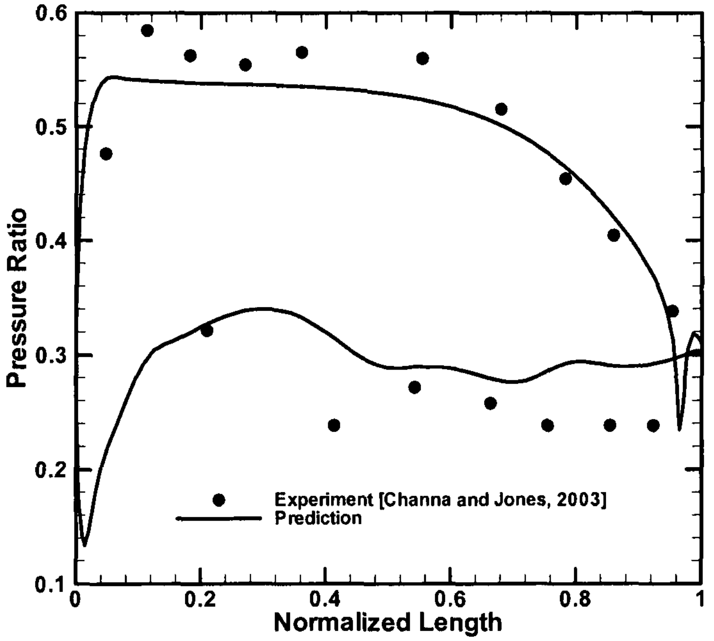

(b)

Figure 4.2 Comparison of predicted static pressure distribution at (a) the stator vane and (b) the rotor blade mid span.

turbine flow and heat transfer characteristics under realistic conditions may be well simulated using the present model.

4.3 Results and Discussion

Details of heat transfer distribution on the blade tip and casing, associated with tip leakage aerodynamics in the tip clearance region, have been discussed in the previous sections. In the baseline case, a tip clearance of 1.2 mm, uniform inlet temperature of 444K, and a rotational speed of 9500 rpm were chosen. The effects of the clearance heights were investigated by considering three gap sizes of 0.6 mm, 1.2 mm and 2 mm which are 1%, 3% and 5% of the blade span, respectively. In order to compare the effect of rotor rotational speeds on the leakage flow structure and its influence on the heat transfer distributions, three different speeds of 9500 rpm (76% of design speed), 12500 rpm (design speed), and 15500 rpm (124% of design speed) were studied. These correspond to positive, zero and negative flow incidence at the mid span, respectively. The typical speed range of rotating turbines is from -30% to +20% of the design speed (Krieger et al., 43). The lower speed (9500 rpm) corresponds to the experimental reference. The same interval was applied for the higher speed (15500 rpm). Leakage flow structure, significantly affected by the height of the clearance and rotational speeds (rotor inlet flow angle), contributes to the rate of heat transfer to varying degrees. The effect of these two major parameters on aerodynamics and the rate of heat transfer have been studied extensively.

For the heat transfer analysis, a dimensionless parameter, the Nusselt number, is used and defined as

$$Nu = \frac{HC}{k} \tag{4.1}$$

where C is chord length, measured at the blade tip, k is fluid's thermal conductivity and h is the heat transfer coefficient, which is further defined as

$$h = \frac{q}{T_w - T_{or,in}} \tag{4.2}$$

in which q is the wall heat flux, T_w is the blade surface temperature, and $T_{or,in}$ is the averaged absolute total temperature at the rotor inlet.

In order to visualize the typical tip leakage flow structure, a 3-D view of path lines is adopted in Fig. 4.3. Path lines of the fluid particles originate from two distinct locations: one at the tip region, where the flow separates near the pressure side edge, and the other at passage flow near the casing and suction side. Reverse cross flows are noticed, and are caused by the relative casing motion. It is observed that the recirculating flow near the pressure side moves downstream with swirling motion along the tip surface. In all cases, this kind of flow recirculation can be seen on the blade tip surface. However, the strength and size of recirculation varies with the flow and geometry conditions. The effect of the casing relative motion on the passage flow can also be seen in Fig. 4.3. The passage flow near the casing is dragged into the blade tip region from the suction side due to viscous effects on the casing. It is then deflected again by the leakage flow issued from the pressure side, and moves downstream with mixing along the blade surface. The strength of reverse cross flow is fully dependent on the rotor rotating speeds. The details of the

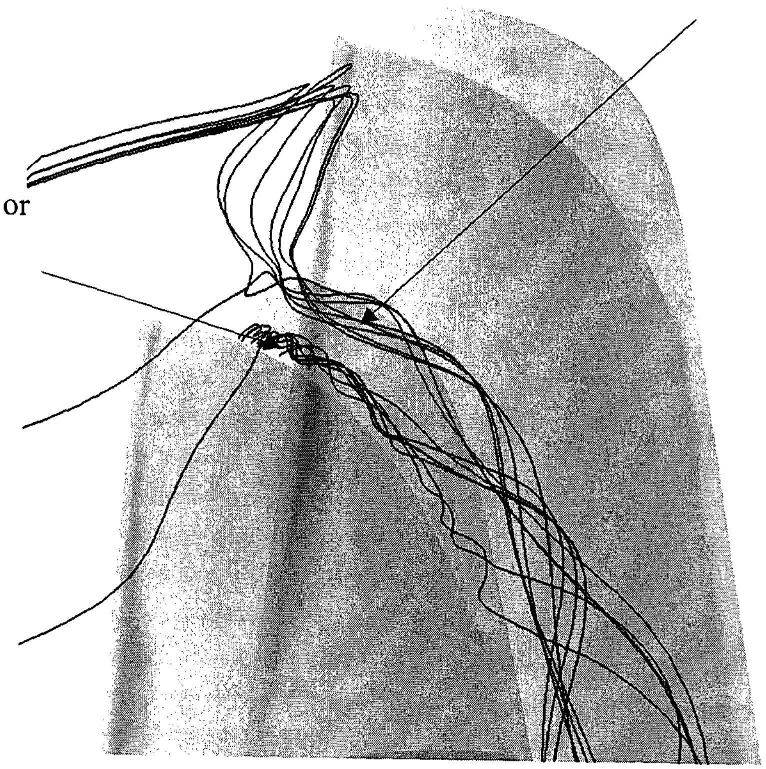

Reverse cross flow due to relative casing motion

Flow separation or recirculation

Figure 4.3 Pathlines for the flow circulation and reverse cross flow in the tip region (at 1.2 mm clearance height).

effect of the clearance heights and rotor speeds on the leakage flow structure and heat transfer are discussed in following sections.

4.3.1 Effect of the Tip Clearance Heights

Leakage flow recirculation zone, point of reattachment and the vortical mixing flow between the reverse cross flow and leakage flow, that are the major consequences of the leakage flow complexity, are indicated using streamlines in Fig. 4.4. Leakage flow entering the tip gap from the pressure side with sudden change in area and direction causes the flow separation from the tip surface. Leakage flow is then reattaches on the tip surface. The point of reattachment is shifting to the suction side with the increasing of gap height and the relative change of flow recirculation height is also apparent (Fig. 4.4). As the clearance height increases, the recirculating flow occurs early near the leading edge, becomes larger, and covers larger tip surface area.

Since the casing and the leakage flow have mainly circumferential motions with opposite directions for a low speed, 9500 rpm, the circumferential flow variation in the clearance region can be used to see these interactions. In the present computational domain, y direction in the tip region is almost aligned with circumferential direction. Therefore, for convenience, the v-velocity profiles at several locations along the y direction at the 25% axial chord are plotted against the normalized clearance height in Fig. 4.5. It is seen that the reverse cross flow in the tip gap becomes outstanding near the suction side. It restricts the leakage flow to be remained within 60% of the tip gap height near the suction side

(a) 0.6 mm

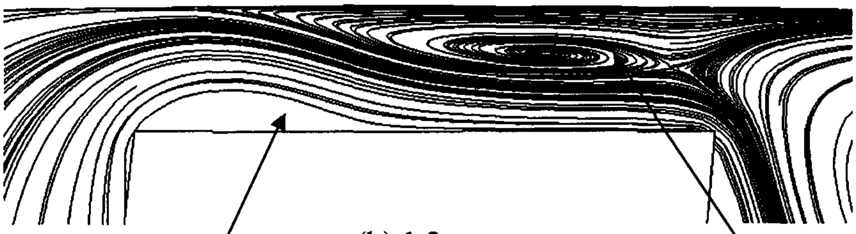

(b) 1.2 mm

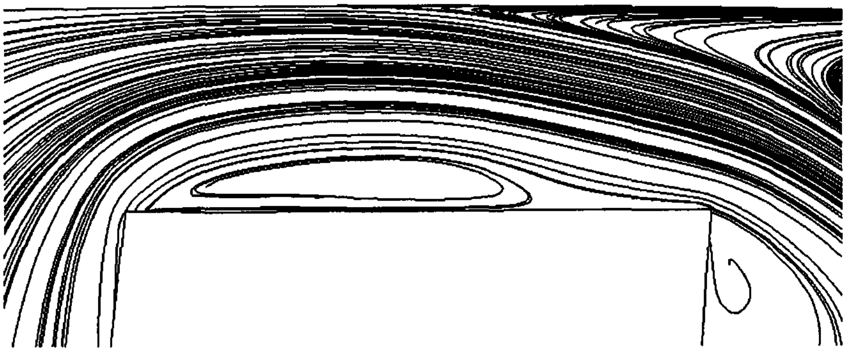

(c) 2 mm

Figure 4.4 Streamlines for the flow circulation and reverse cross flow in the tip region at the plane of 25% axial chord.

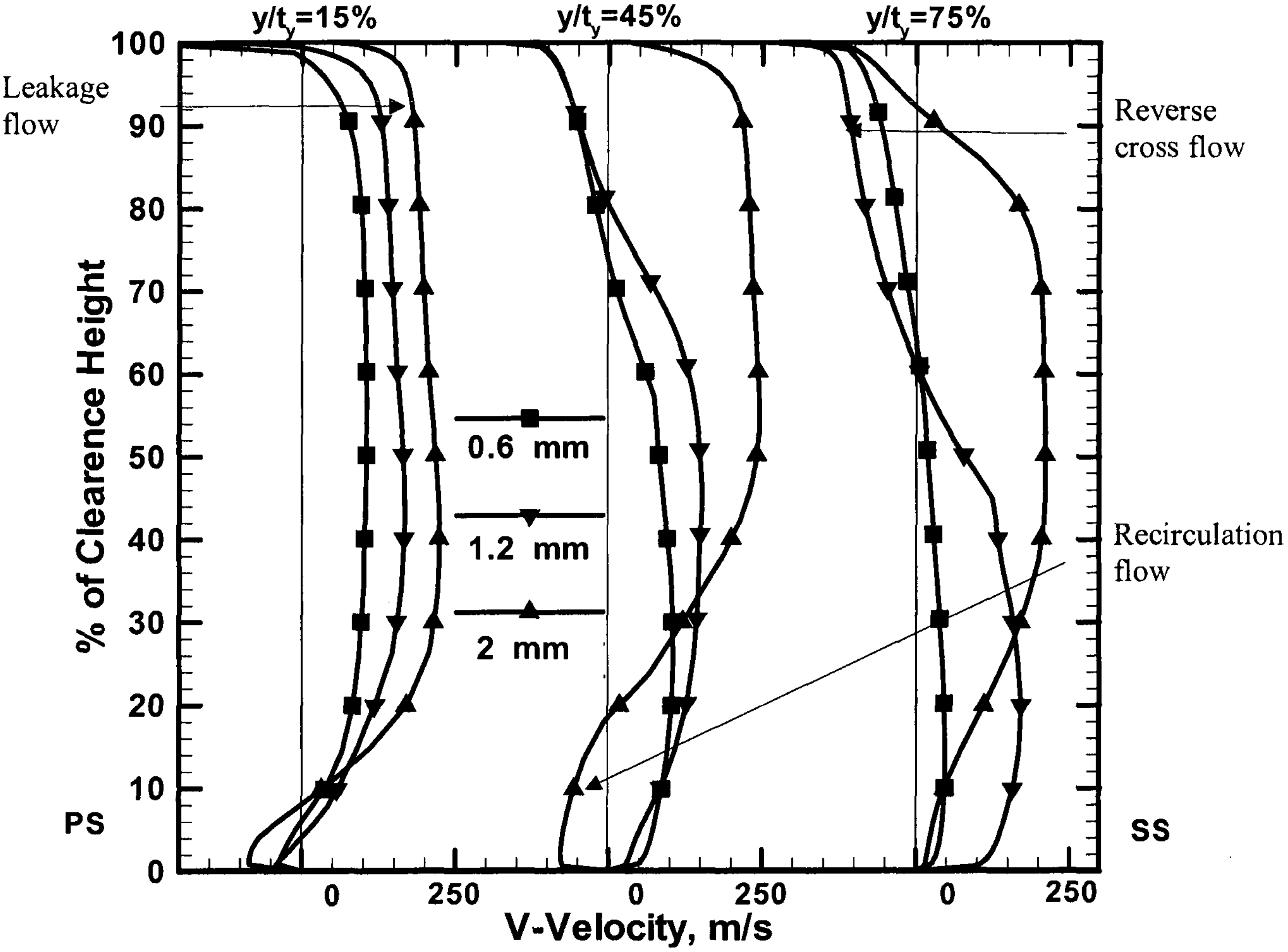

Figure 4.5 V-Velocity profiles along the y-direction at 25% of the axial chord for different clearance heights.

(1.2 mm case). This effect is gradually diminishing from suction side to pressure side where it is encountered by the high speed leakage flow from the pressure side. The pressure variations along the circumferential line at the 25% axial chord and the mid height of tip gap are shown in Fig. 4.6. As the clearance height increases, the pressure loss due to the leakage flow increases in the pressure side. It can also be seen in Fig. 4.6 that the larger pressure drop through the tip gap region for larger clearance height results in higher speed of leakage flow. Under the same operating condition, the leakage flow velocity increases with the clearance heights (Fig. 4.5), thus mass transfer rate through the tip gap increases. The reverse cross flow also increases with the clearance heights. However, at higher clearance height (2 mm), it rather decreases. Because at the same speed of rotation and operating condition, the viscous effect on the casing remains invariable, but the leakage flow speed much increases.

Flow separation is another important flow phenomena associated with the leakage flow. This causes a low pressure region on the blade tip surface near the pressure side, and obstructs the leakage flow attachment on the tip surface. The height of the flow recirculation region increases with the height of the tip gap (Fig. 4.4). Leakage flow reattachments on the tip surface occur at the location of $y/t_y = 25\%$ and 40% along $x/C_x = 25\%$ for 0.6 mm and 1.2 mm clearance heights, respectively. At a larger tip gap (2 mm), leakage flow reattaches at $y/t_y = 70\%$ from the pressure side edge at $x/C_x = 25\%$ plane. The flow reattachment increases the surface pressure and reduces the boundary layer thickness. Thus it is expected to have higher heat transfer at this reattachment region.

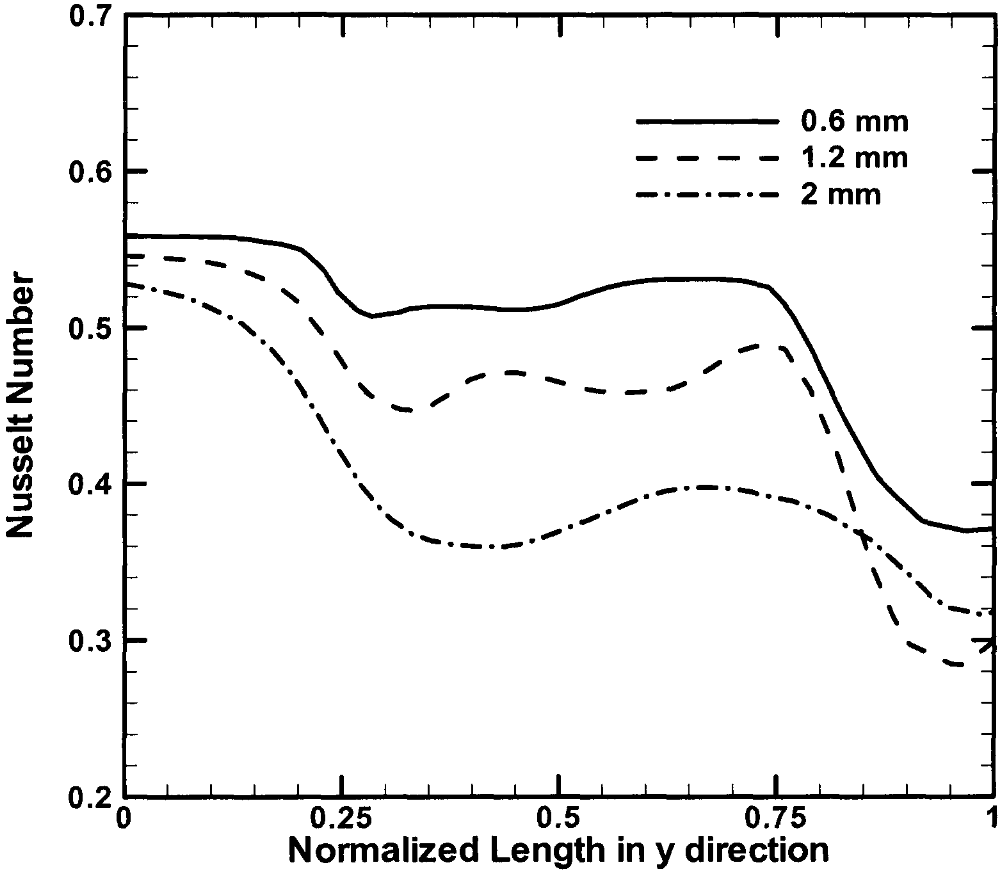

Figure 4.6 Static pressure ratio along the line $y/t_y = 0$ to 1, in the mid clearance at 25% of the chord for different clearance heights.

Figure 4.7 shows contour of Nusselt number on the casing for different clearance heights. The presence of the reverse cross flow and its effect on the heat transfer distribution on the casing is apparent. The higher heat transfer region is seen along the pressure side edge with a maximum near the blade leading edge and then decreases gradually. This could be due to the fact that the leakage flow of higher temperature approaches along the pressure side edge. It is observed that the heat transfer rate is lower in the region near the suction side where the leakage flow is detached from the casing by reverse cross flow (see Figs. 4.4 and 4.5).

Nusselt number distributions on casing circumference, between the projections of the blade tip pressure and suction side edges, are plotted for different clearance heights at 25% axial chord in Fig. 4.8. Heat transfer rate is higher near the pressure side edge, as discussed earlier, and rapidly decreases along the circumferential direction. It remains relatively low and constant value beyond certain locations of $y/t_y = 15\%$, 20% and 75% for 0.6 mm, 1.2 mm, and 2.0 mm heights, respectively. It can be attributed to relatively colder reverse cross flow coverage near the casing in this region (see Fig. 4.4). It is also shown in Fig. 4.4 that the case of 0.6 mm has thinner reverse cross flow coverage and earlier vortical mixing with the leakage flow (close to the pressure side) in comparison with the case of 1.2 mm. It causes higher heat transfer rate in this region (beyond $y/t_y = 25\%$) for 0.6 mm case than 1.2 mm case (Fig. 4.8). However, a reverse cross flow cannot be much dragged into the tip region for 2 mm case due to the higher speed leakage flow. In this case, there is no vortical mixing observed between reverse cross flow and

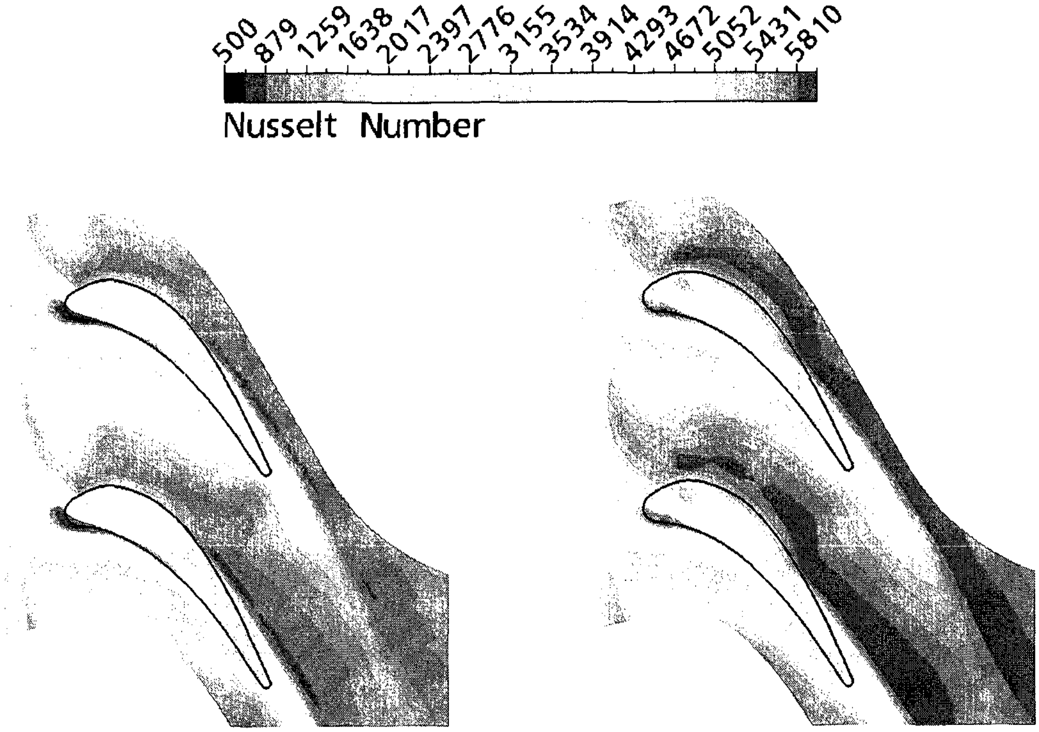

(a) 0.6 mm

(b) 1.2 mm

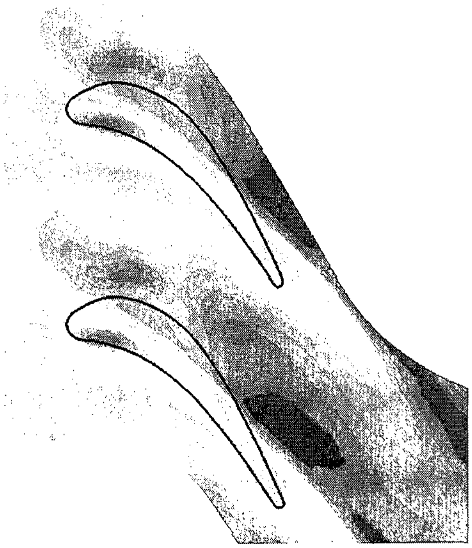

(c) 2 mm

Figure 4.7 Contour of Nusselt number on the shroud for three different clearance heights.

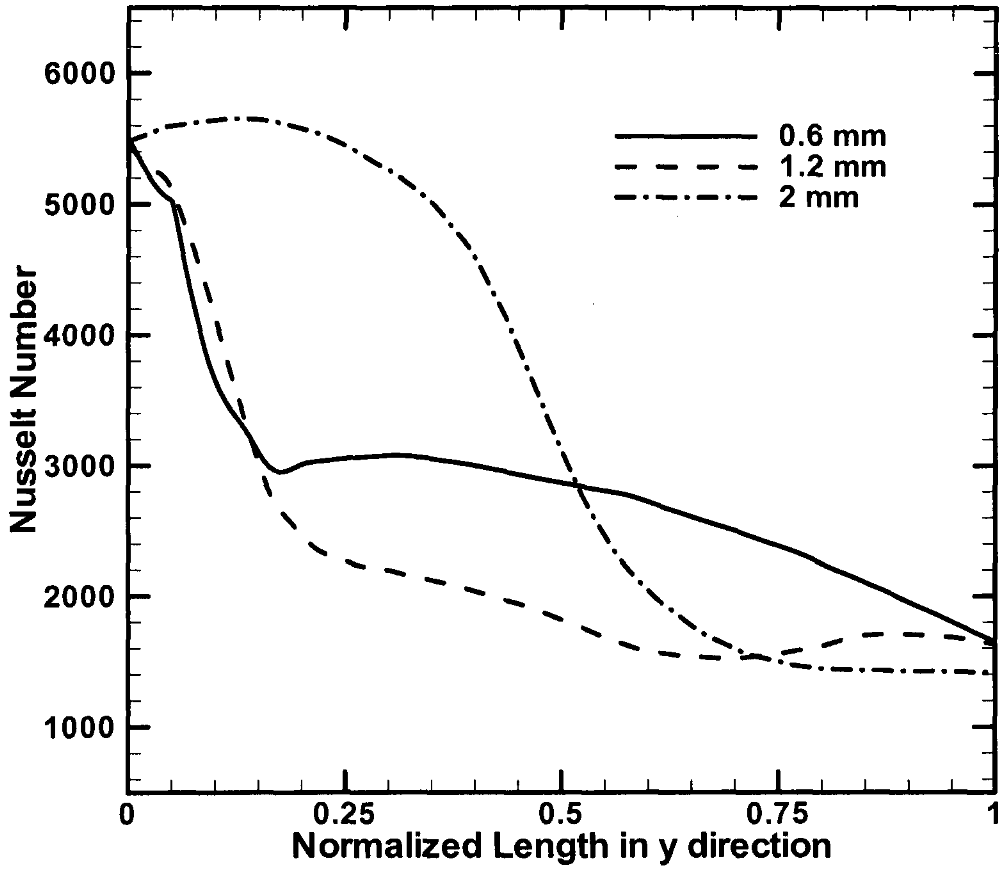

Figure 4.8 Nusselt number distributions along the casing thickness at 25% axial chord plane for different clearance heights.

leakage flow inside the tip region (Fig. 4.4c). This is the reason why the case of 2 mm has wider high Nusselt number distribution up to around $y/t_y = 60\%$ than smaller height cases (Fig. 4.8).

Nusselt number distributions on the blade tip surface are presented in Fig 4.9. Near the pressure side edge, heat transfer rate is lower indicating the region of flow recirculation on the tip surface for all cases (see Fig. 4.4). For 2 mm height, Nusselt number near the suction side, between 20% to 60% of the chord, is higher caused by the leakage flow reattachment beyond the flow separation region (Fig. 4.4). However, at smaller clearance heights (Fig. 4.8), the region of low heat transfer rate appears again beyond the leakage flow reattachment region where the heat transfer rate is high. At all clearance heights, the heat transfer rate on the tip surface becomes the minimum value near the trailing edge because of leakage flow lift off and the coverage of recirculating flow.

Figure 4.10 shows Nusselt number distributions along the circumferential line on the blade tip surface at 25% axial chord for different clearance heights. For both cases of 0.6 mm and 1.2 mm heights, same pattern can be seen it for Nusselt number distributions. Low heat transfer rate region exists near the pressure side since the leakage flow lift off (separation) and recirculates. Beyond this region, heat transfer rate increases due to the leakage flow reattachment on the tip surface. Near the suction side, a vortical mixing is observed between the reverse cross flow and tip leakage flow (see Figs. 4.4 and 4.5). The velocity and temperature of the leakage flow over the tip surface becomes lower due to this mixing as it approaches to the suction side edge (see Figs. 4.5 and 4.11).

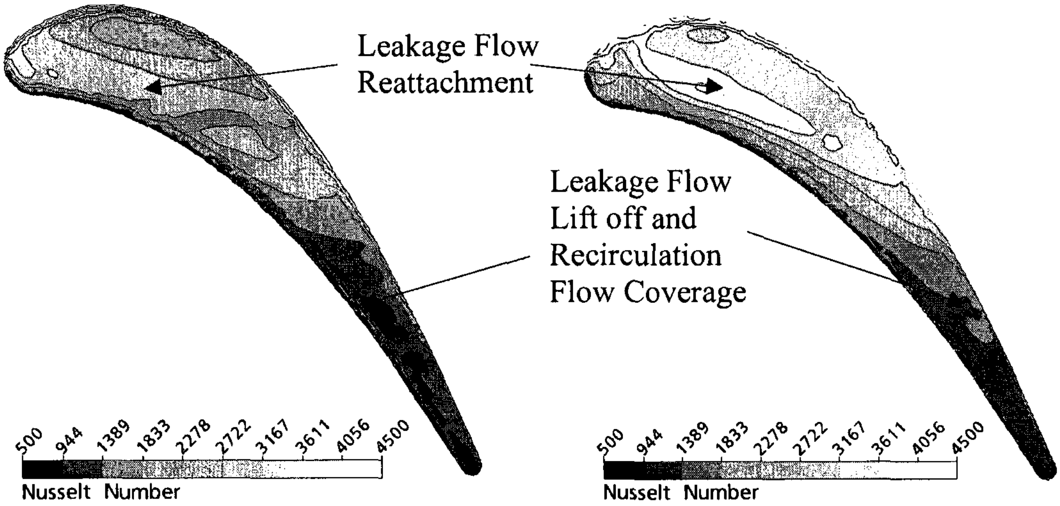

(a) 0.6 mm

(b) 1.2 mm

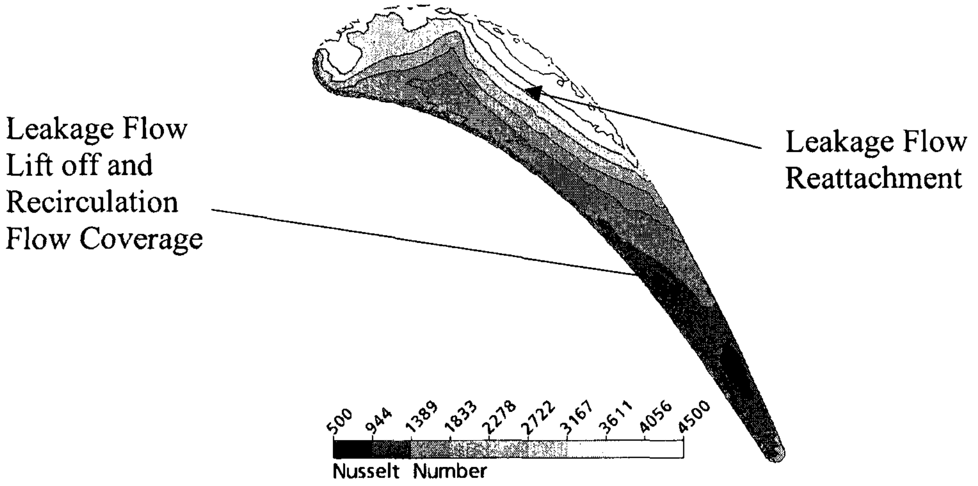

(c) 2 mm

Figure 4.9 Contour of Nusselt number on the blade tip surface for different height of the clearance.

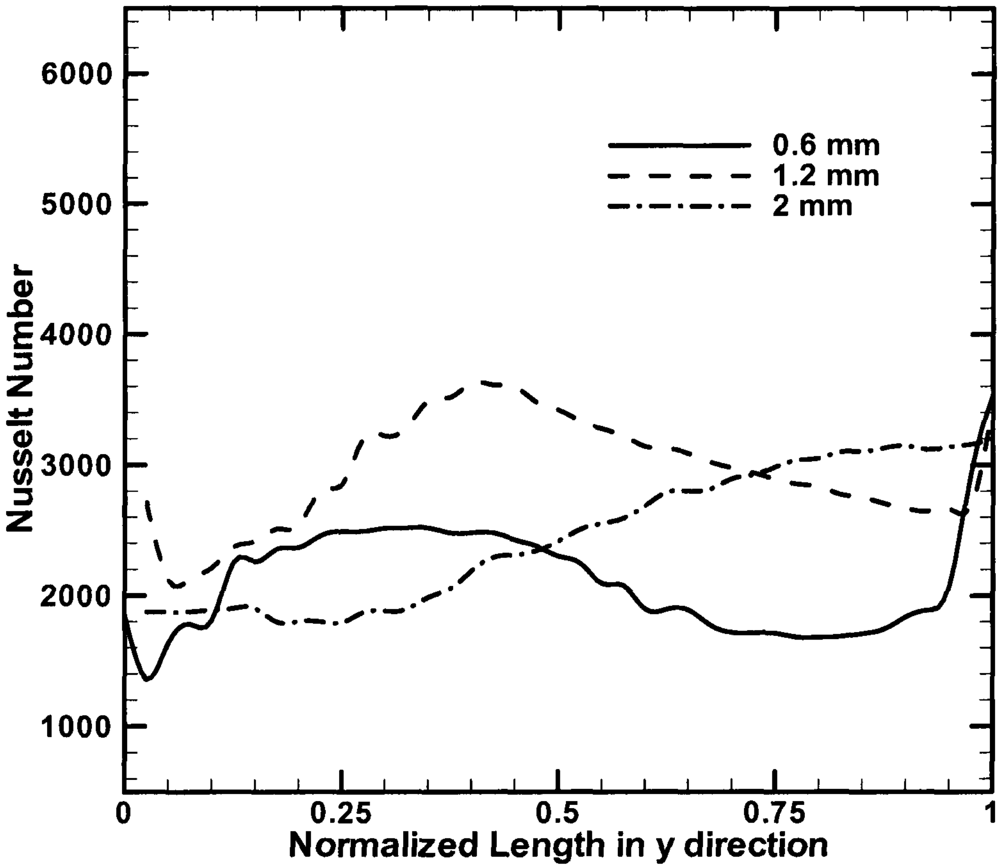

Figure 4.10 Nusselt number distributions along the blade tip thickness at 25% axial chord plane for different clearance heights.

Therefore, heat transfer rate decreases again near the suction side. However, the heat transfer rate increases continuously from pressure side to suction side in the case of 2 mm height, in compare to the cases of smaller gaps. At this higher clearance height, the flow recirculation size becomes larger near the pressure side and the leakage flow reattaches near the suction side without any reverse cross flow mixing inside the tip region (Fig. 4.4c).

4.3.2 Effect of the Rotational Speeds

Figure 4.12 shows tip leakage flows at different rotor speeds. The flow path through the tip clearance region is presented with streamlines at the mid plane of the tip clearance height. The change of flow incidence from positive (Fig. 4.12a) to negative (Fig. 4.12c) with respect to rotor speeds is clearly noticeable. It is observed that the blade tip region is covered by the leakage flow issued from the pressure side for a low speed rotation (9500 rpm). In this case, most of the leakage flow has normal direction to the blade profile of pressure side edge. As a result, the flow separation and recirculation due to the sudden change of flow direction occurs along the pressure side edge (see Fig. 4.4). In contrast to the case of the low rotation speed, the flow coming from the upstream and suction side, not the pressure side, mainly covers the upstream parts of the tip region (near the leading edge) for a high rotation speed (15500 rpm). Therefore, the separation near the pressure side edge becomes very small (see Fig. 4.13c) and not dominant up to 70% of axial chord. The small recirculation occurs rather near the leading edge and the suction side due to negative incidence (see Fig. 4.16), whereas it doesn't occur at the case of 9500 rpm.

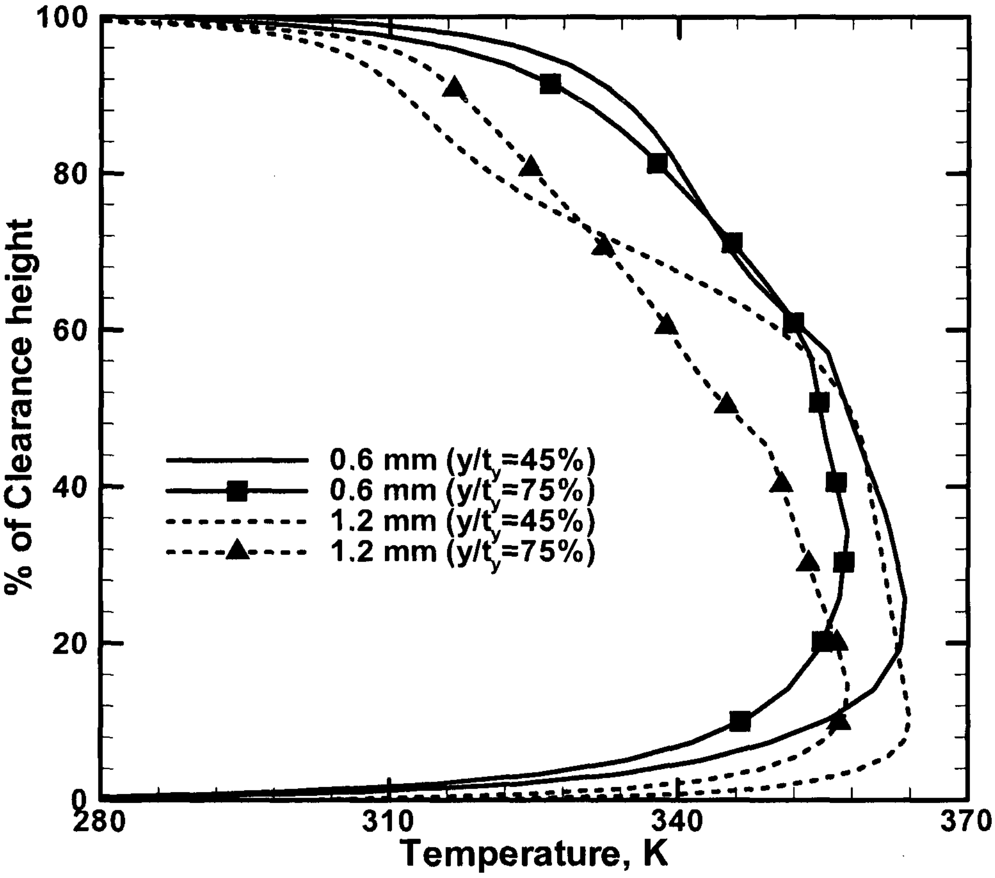

Figure 4.11 Static temperature profile along the y-direction at 25% of the chord for different clearance heights.

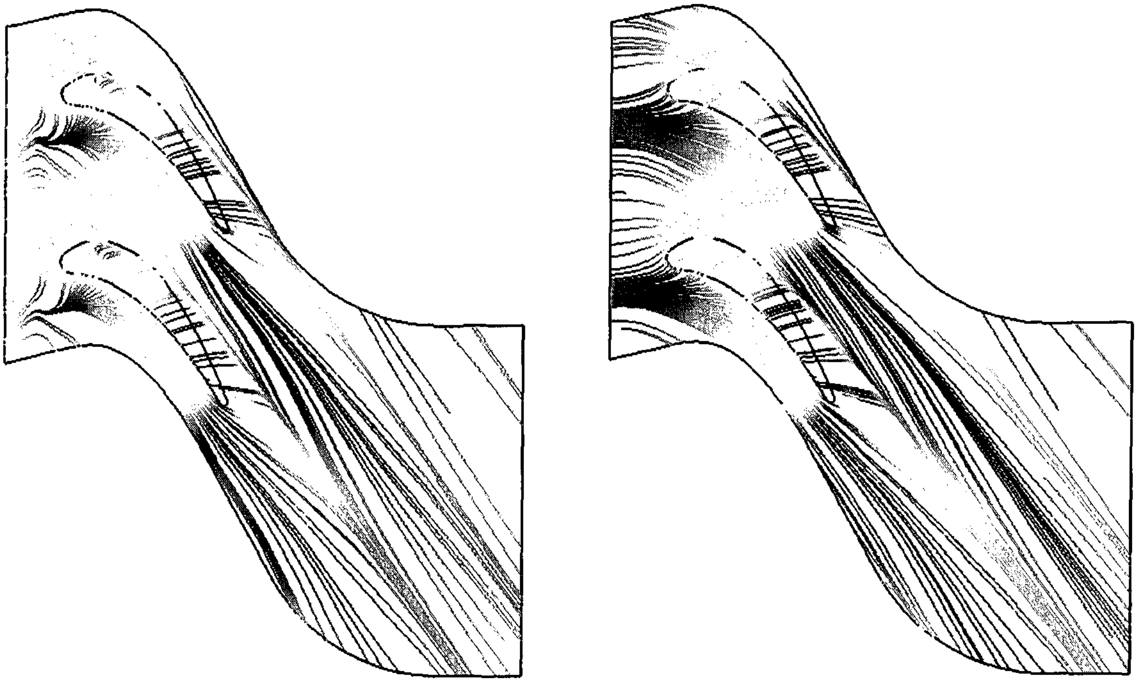

(a) 9500 rpm

(b) 12500 rpm

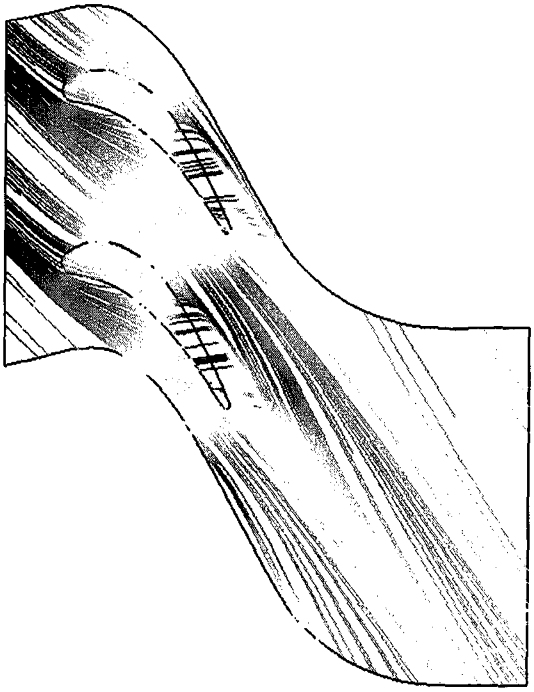

(c) 15500 rpm

Figure 4.12 Streamlines over the blade tip for three different speeds (coloured by relative velocity).

The effect of rotational speed on the variation of the tip leakage flow structure for 1.2 mm clearance height is illustrated by using 2-D velocity vectors in Fig. 4.13. It can be seen that the reverse cross flow from SS to PS near the casing is significant and dominates in the tip clearance region as the rotation speed increases. It is also attributed to the change of flow incidence angle depending on rotation speeds, ie. negative incidence for higher rotation speed. Leakage flow characteristics inside the tip gap are similar between two cases of 9500 rpm and 12500 rpm (Figs. 4.13a, b). However, when the rotor runs at higher speeds with negative incidence, the leakage flow structures and heat transfer distributions are far different from the other cases.

The Nusselt number distributions along the casing circumference are presented in Fig. 4.14 for different rotor speeds. The effect of the reverse cross flow and change of flow incidence on the heat transfer rate onto the casing with rotation speeds is well shown in Fig. 4.14. The leakage flow issued from the pressure side is shifting towards the trailing edge due to the upstream inlet flow with incidence change (Fig. 4.12). It is found that the critical region of high heat transfer rate along the pressure side edge moves toward trailing edge with the increase of the rotor speed. At a higher rotation speed, reverse cross flow takes more space inside the tip gap, since the effect of the relative motion of the casing is sufficiently strengthened. Therefore, the low heat transfer rate region near the suction side is enlarged with the rotor speeds. At 25% axial chord location, the maximum heat transfer rate at 12500 rpm decreases 20% compared to that of the low speed case (9500 rpm). For the higher speed (15500 rpm), the distribution is flattened, because the entire area is filled by the colder reverse cross flow (see Fig. 4.13c). The maximum

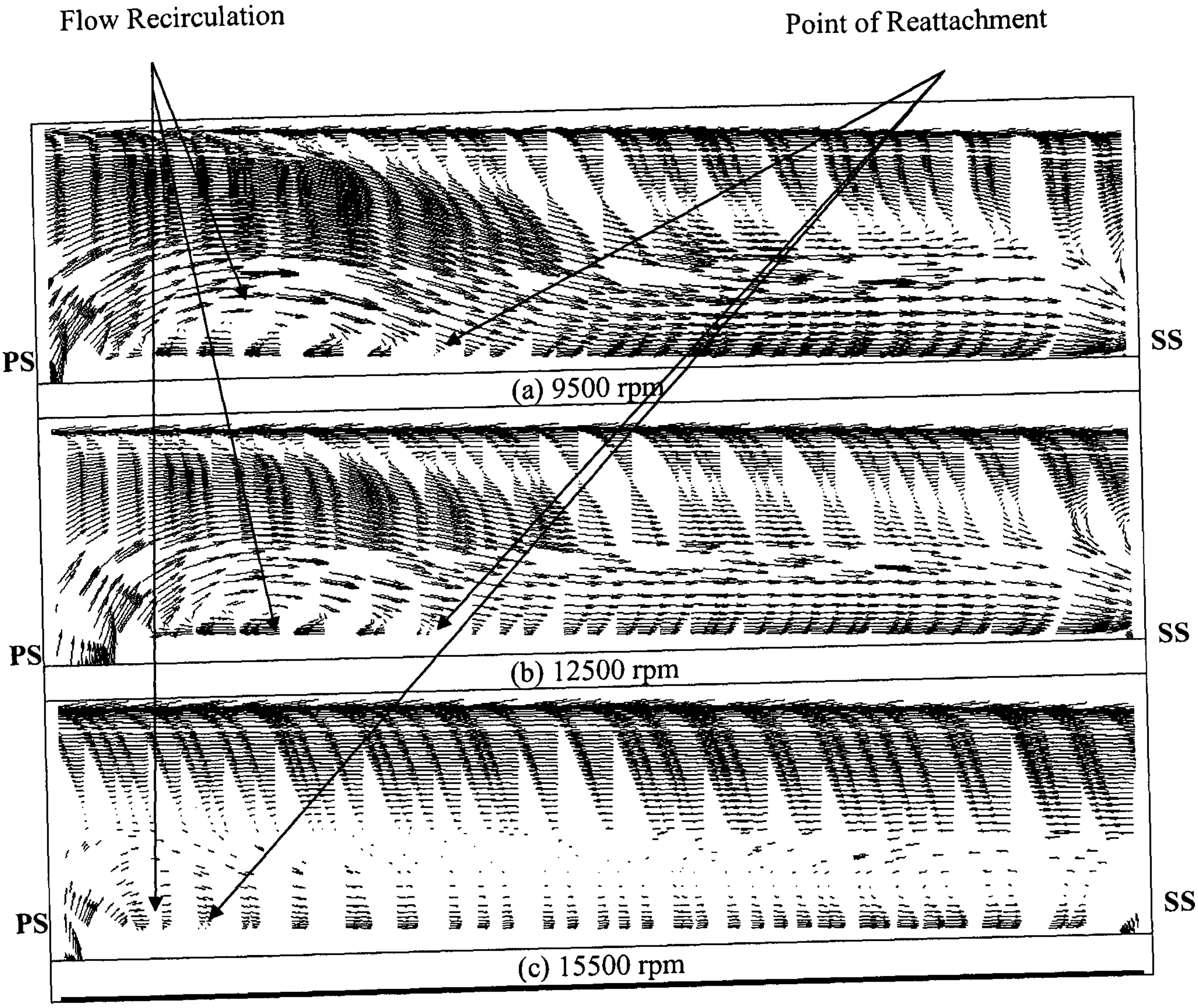

Figure 4.13 2D velocity vectors at the quarter axial chord plane.

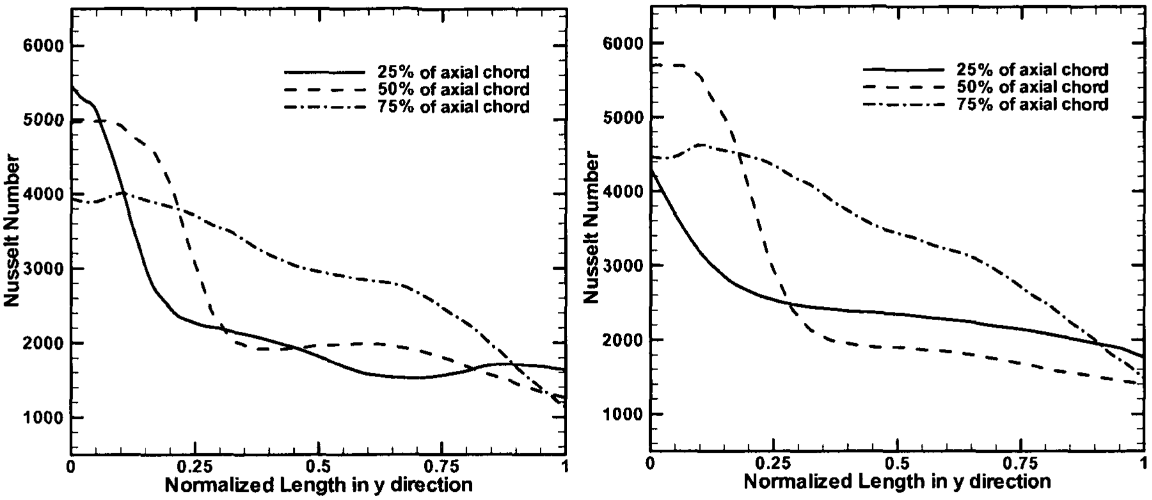

(a) 9500 rpm (b) 12500 rpm

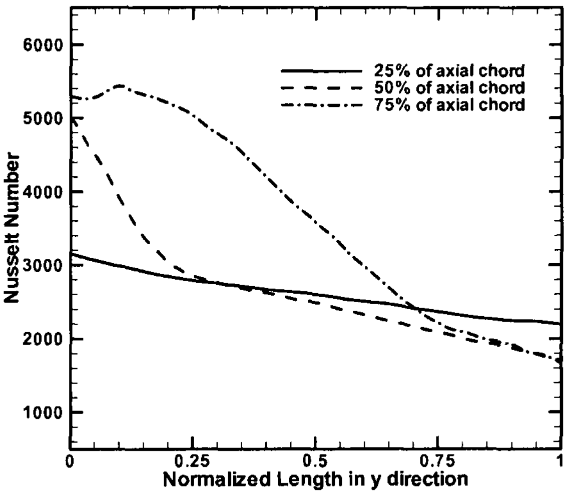

(c) 15500 rpm

Figure 4.14 Nusselt number distribution along shroud circumference from line of projections of blade tip pressure to suction.

reduction in heat transfer rate for higher speed (15500 rpm) is about 42% in comparing with the low speed case (9500 rpm). However, the critical region of high heat transfer for the high speed case (15500 rpm) appears close to the trailing edge where the heat transfer rate increases 32% more than the low rotation speed case due to the higher leakage flow velocity.

Nusselt number distributions on the blade tip surface for different rotor speeds are presented in Fig. 4.15. We can see the typical distributions in case of 12500 rpm, such as, the low heat transfer rate region near the pressure side edge and trailing edge due to the leakage flow separation and high heat transfer rate region because of the leakage flow reattachment (Figs. 4.9b & 4.15a). However, for the case of 15500 rpm, the heat transfer distribution is different from those of low speed conditions due to different leakage flow structure. It can be seen the higher Nusselt number region near the leading edge (Fig. 4.15b). However, the lower heat transfer rate region occurs in the inclined region between 20% to 40% axial chord. It might be attributed to the flow paths and mixing phenomena of leakage flow entering from the pressure side, upstream inlet flow, and reverse cross flow. Point A is located near the leading edge and has higher heat transfer rate, Point B is about 30% axial chord and near the pressure side (Fig. 4.15b).

In the higher rotation speed case (15500 rpm), the rotor inlet flow has negative incidence angle. Small recirculation in streamwise direction occurs near the leading edge (Fig. 4.16). This upstream inlet flow has higher temperature profile (at point A in Fig. 4.17). The direction of the leakage flow is changing around 20% axial chord from negative to

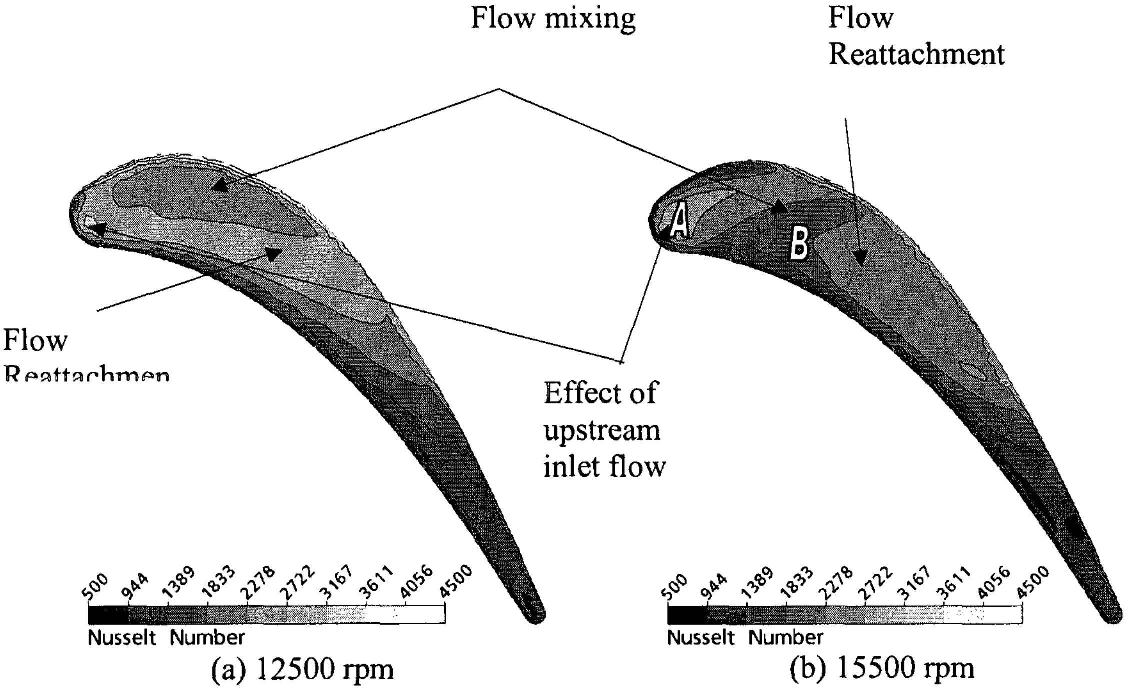

Figure 4.15 Contour of Nusselt number on the blade tip surface for different speeds.

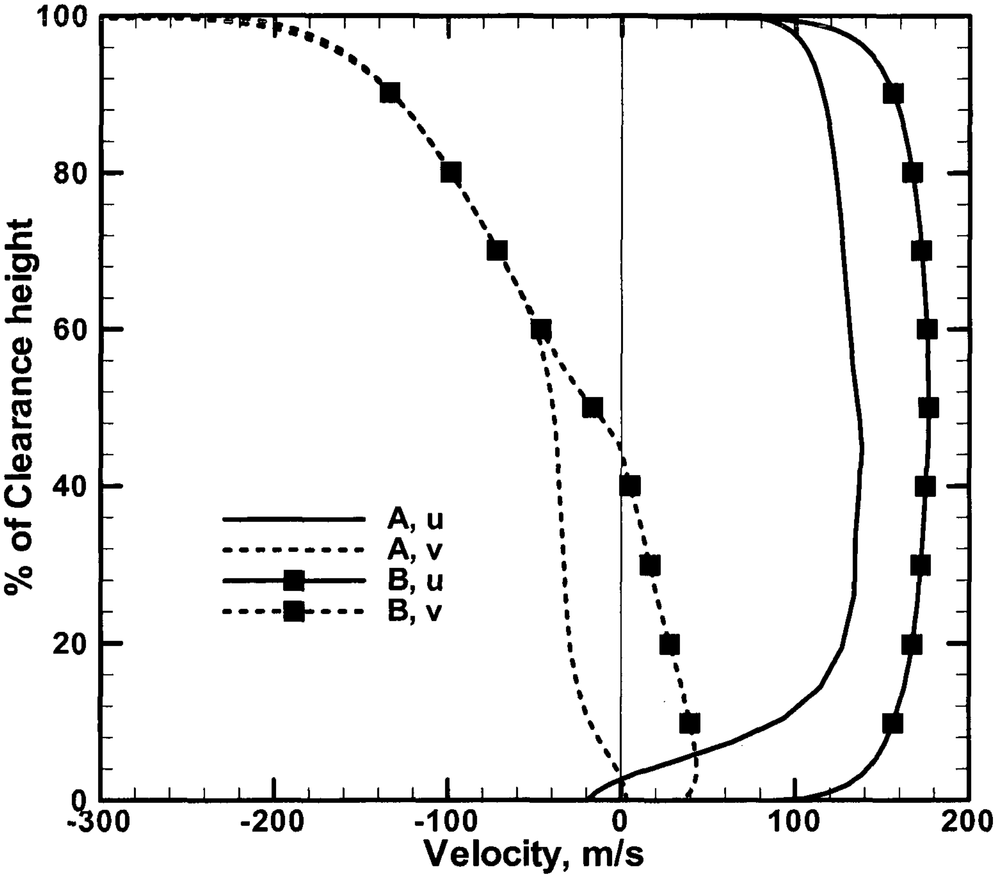

Figure 4.16 U and V velocity profile in the locations indicated in figure 4.15.

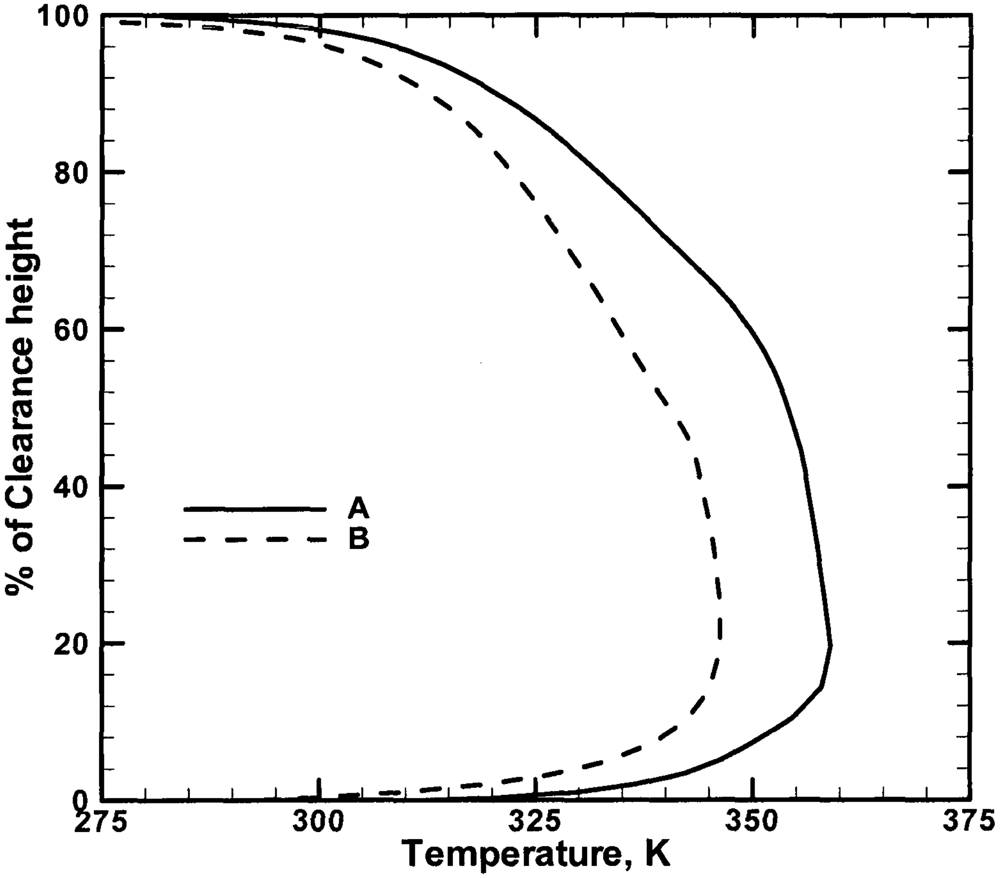

Figure 4.17 Temperature profile in the locations indicated in figure 4.15.

positive, and the leakage flow entering from the pressure side occupies over the tip surface (Fig. 4.16). Eventually, the mixing of hot upstream flow, leakage flow from the pressure side, and cold reverse cross flow is occurring around 20% to 40% axial chord region, and leaves towards the blade suction side. It results in lower heat transfer rate region along this mixing region. However, beyond this region, the typical leakage flow structure occupies on the tip surface.

Chapter 5

Unsteady Simulation and Analysis

In the steady analysis, typical tip leakage flow structures and heat transfer distributions have been demonstrated. Also, the effect of tip clearance heights and rotor rotation speeds on tip leakage flow and heat transfer rate features have been analyzed. However, the flow physics inside the turbine tip is proven to be highly unsteady, three dimensional and complex, leading to a critical heat transfer distribution on the turbine casing and blade tip. Since few studies have been conducted on the unsteady tip leakage flow associated with heat transfer characteristics, further unsteady simulations are still required to account for the effects of stator-rotor interactions; progressive stator trailing edge shock, incoming secondary flow and wakes, and periodic rotor passing. These effects have been ignored in the steady simulations due to the circumferential averaging at the stator-rotor interface. In this chapter, the unsteady results of the tip leakage flow and heat transfer rate under those effects will be discussed in detail with the challenges of numerical methodology for achieving time-accurate solutions.

5.1 Computational Details

All unsteady cases have been simulated using a commercial CFD (Computational Fluid Dynamics) solver ANSYS CFX R.11. A high resolution second order central difference scheme for the space and second order backward Euler scheme for the time were used to discretize the equations for the flow, turbulent kinetic energy, and specific dissipation rate. Similar boundary conditions based on the experimental works of Chana and Jones

[12,13] were applied (see Table 3.2) for this unsteady simulation. At the inlet of the stator domain, a total pressure of 4.6 bar and a total temperature of 444 K were specified, while a static pressure of 1.46 bar at the rotor domain outlet was set to achieve a value close to the experimental static pressure at the rotor blade exit. In order to facilitate an appropriate setup for the unsteady cases (see Table 3.4), a steady-state simulations with "Stage" option at the stator-rotor interface were performed, depending on the selected case parameters (see Table 3.3). Stage model, in ANSYS CFX, performs a circumferential averaging on the fluxes at the interface upstream in the stationary frame of reference. The averaged fluxes are applied to the interface downstream as the inlet flow condition, for the rotor domain in the rotating frame of reference. The steady results using "Stage" model were then used as initial values for the time dependent simulations by setting the interface as "Transient Rotor-Stator" model in CFX. This model allows for simulating time dependent characteristics of the flow. In this model, a sliding interface is used to allow rotational movement of the rotor domain with respect to the stationary stator. A sufficient number of time steps have been used to ensure that the flow field is adequately resolved for each pass of the stator vane. The time dependant heat transfer results were then recorded on the rotor casing and tip, and finally analyzed.

5.2 Tests for Time Steps, Sub Iterations and Vane Pass

Accuracy in unsteady simulations is highly dependent on the number of time steps during one vane passing period (time step size) and the number of subiterations for each time step. An optimum number of time steps were selected based on trials and comparisons of the results in order to reduce the computational cost and achieve an accurate solution in

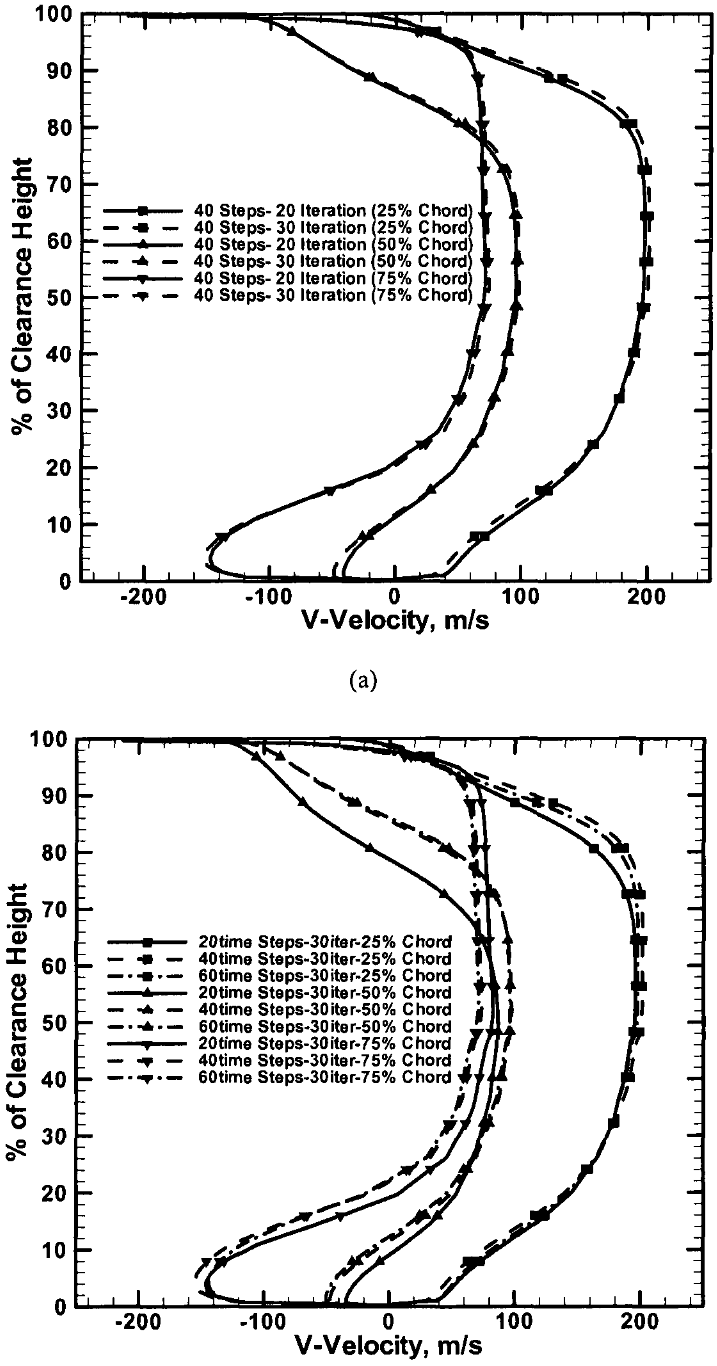

(a)

(b)

Figure 5.1 Effect of number of (a) sub-iterations, (b) time steps.

time. Figure 5.1 illustrates the effect of the number of subiterations for each time step (Fig. 5.1a) and the number of time steps for each vane pass (Fig. 5.1b). Convergence for the continuity, momentum, heat transfer and turbulence, such as mass flow rate, total pressure and static pressure at different locations along the domain, were monitored during the simulation. The convergence residuals for each time step dropped at least three orders of magnitude within 20-30 subiterations. Negligible differences were observed in velocity and temperature profiles at the tip gap between 20 and 30 subiterations (Fig. 5.1a). It is also seen that the predictions have a discrepancy between 20 and 40 time steps. However, at a further increase in the number of time steps (the decrease of time step size), the discrepancies are insignificant when compared to 40 time steps. It can therefore be the optimum condition which can be used without any significant loss of solution accuracy for the unsteady simulation.

The simulations with unsteady stator-rotor interface model were performed for all cases and allowed to run up to 200 time steps (5 vane passing periods) with 20 sub iterations for each time steps. All simulations were performed using a parallel computing of 14 processors with 2.2 GHz AMD Opteron and 14 GB memory on ENCS HPC cluster system at Concordia University. The simulation time was approximately 5 days for 200 time steps of 5 vane passing periods.

5.3 Results and Discussions

5.3.1 The Stator – Rotor Interaction

The phenomenon of the stator trailing edge shock is associated with a turbine stage, operating at transonic flow conditions. This shock has a greater interaction with the rotor passage flow, resulting in a change of flow direction and properties. The instantaneous pressure contours in the region between stator and rotor at mid clearance height for two different instants are depicted in Fig. 5.2 to see the effect of upstream stator flow on the downstream rotor flowfields. The over-accelerated nozzle vane flow is accompanied with a shock at the stator trailing edge, in order to match the back pressure. The high pressure region with relatively high pressure gradient near the stator trailing edge can be seen in Fig. 5.2. This high pressure region is progressing further to the rotor blade (Fig. 5.2b). It is strongly related with the phenomenon of the stator trailing edge shock. To capture an accurate shock wave, fine grid adaptation is required in the shock region, but has not been used to avoid unacceptable long computational times. This study has focused on the tip clearance region and already adapted a fine mesh in the tip region. Predicted results at different time instants demonstrate that the rotor aerodynamics is greatly affected by the upstream stator flow structure. Hence, the pressure loading on the blade varies significantly with respect to time, furthermore affecting the leakage flow aerodynamics. It can be observed (Fig. 5.2) that, at the instant of $t^*=0.25$, the leading edge region of the rear blade (relative position, 4) is influenced by the high pressure region, related with the trailing edge shock. However, at the instant of $t^*=0.5$, the high pressure region reaches approximately mid chord of the pressure side of the rear blade (relative position, 1) and the other blade is positioned out of this effect. For high speed cases, a similar phenomenon can be observed at different relative positions due to different rotational speeds. Thus, similar effects on the blades were observed at the instants of t*=0.125 and 0.375. When the stator trailing edge shock propagates to the rotor flow field, the flow through the shock undergoes a change in flow direction as well as an increase in pressure. As a result, the flow structure in the rotor tip region will also be affected by this phenomenon. However, in the steady simulation, the effect of stator shock on the rotor section was eliminated due to averaging treatment at the stator-rotor interface.

Figure 5.3 is presented to examine the inlet flow angle variations along the circumferential direction at the mid span of the rotor side inlet at two different instants. Inlet flow angles are calculated using the relative velocity vectors of axial and tangential components at the rotor inlet. Typically, the inlet flow angle of the rotor has a wave pattern (periodic distribution) along the circumferential direction, due to the stator outlet velocity distribution of wave pattern, caused by vane wake and boundary layer effects. In the steady predictions, however, a constant inlet flow angle has been used due to circumferential averaging at the interface. In Fig. 5.3, the inlet flow angle gradually increases to the maximum value along the circumferential direction, following the non-uniform velocity distributions of the vane outflow. However, when the flow passes the relatively high pressure gradient region, related with the trailing edge shock, the inlet flow angle suddenly drops to the minimum. The variation of the flow angle at the rotor inlet is about ±14 degrees for the baseline case (Fig. 5.3a). Due to the change of flow

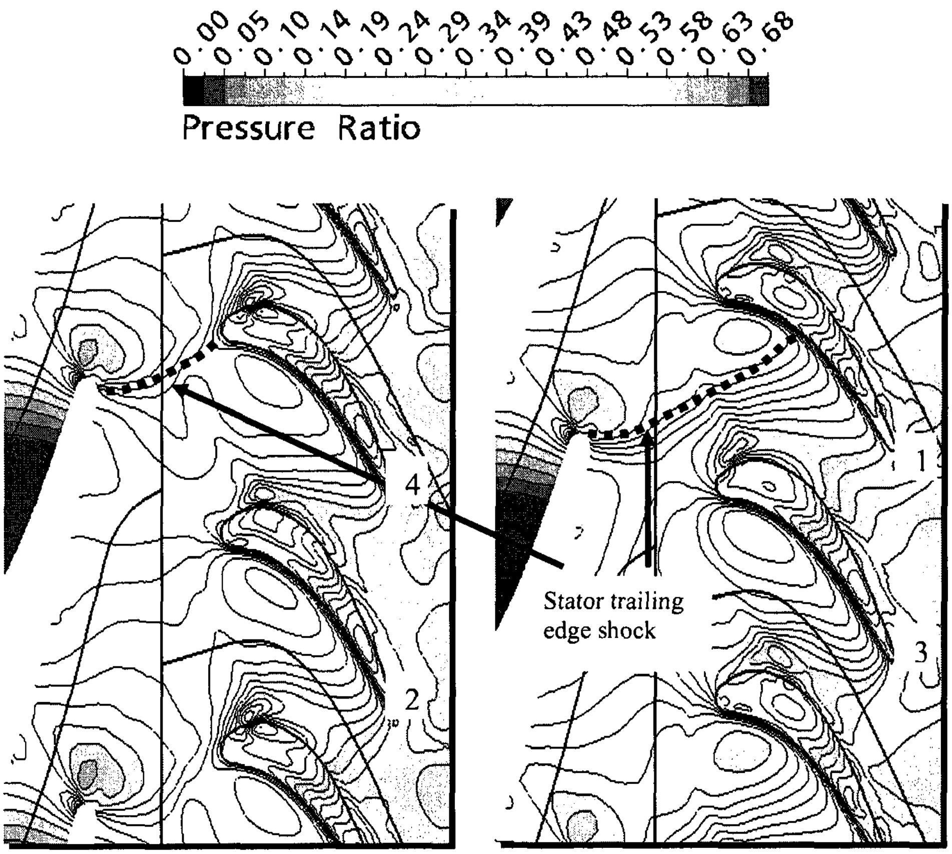

(a) t*=0.25 (5th period)

(b) t*=0.5 (5th period)

Figure 5.2 Pressure contour at stator-rotor mid clearance span.

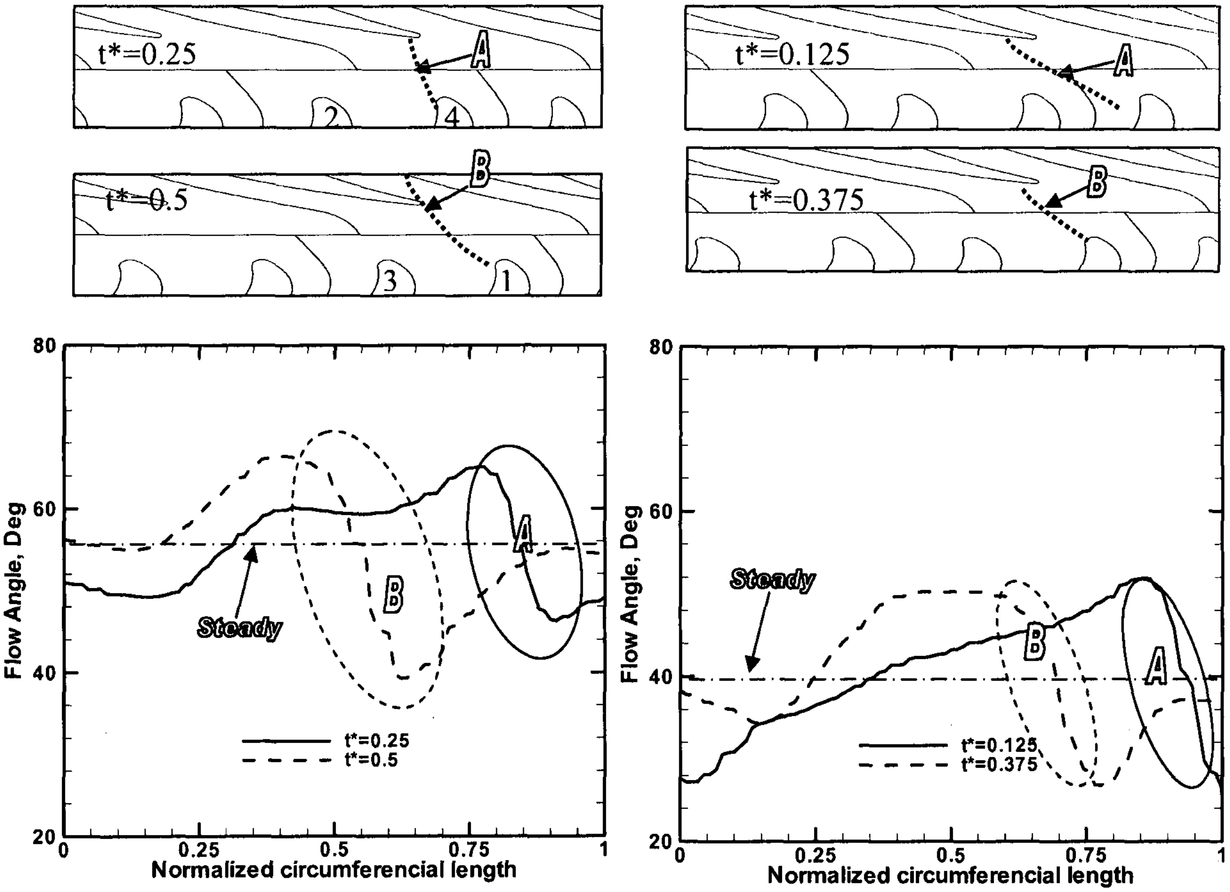

(a)

(b)

Figure 5.3 Inlet flow angle at mid span of the rotor side interface for one pitch along the circumference a. Case: 9500 rpm; 1.2 mm; b. Case: 12500 rpm; 1.2 mm.

incidence, the leakage flow structure is seen differently depending on the relative position of the rotor at different time instants. As seen in Fig. 5.3a, when the non-dimensional time is 0.25, the effect of the shock appears in the vicinity of the leading edge of the rear blade (blade 4). Therefore, the entire passage flow in front of the pressure side of the rear blade remains unaffected and the flow enters the rotor with higher circumferential velocity component (highest inlet flow angle; largest negative incidence). On the other hand, right after the shock, the flow angle (Fig. 5.3a, across location B) suddenly drops, thus, turning the inlet flow towards the axial direction (lowest inlet flow angle; smallest negative incidence) at the instant of t*=0.5, the relative blade position of 1. Therefore, the rotor blade undergoes the gradual increase of inlet flow angle along the relative positions from 1 to 4. At a relatively higher speed (Fig. 5.3b), the overall inflow angle is comparatively less than the low speed case. The maximum angle reached is about 50 deg which is less by 18 degree comparing with the low speed case (Fig. 5.3a). As a result, the flow enters the tip gap with a relatively higher axial component; therefore, the v-velocity component decreases significantly in compare with low speed case (Fig. 5.5b).

5.3.2 Time Periodic Patterns

Unsteady variations of the flow field inside the tip clearance region were monitored for pressure, temperature and velocities, as presented in the Fig.5.4. The non-dimensional time is defined as

$$t^* = \frac{t}{\theta_{stator}} \qquad (5.1)$$

Where θ_{stator} is the stator passing period that may be further defined as

$$\theta_{stator} = \frac{\varphi_{stator}}{\Omega} \tag{5.2}$$

It is to be noted that the relative position of the rotor and stator, at the time of t*= 0, is as indicated in Fig. 3.7. The relative position of the rotor blade follows the numbering 2-3-4-1 with a non-dimensional time sequence (Fig. 5.2).

All monitoring points were located at a quarter axial chord plane for both the front and rear blades. The pressure is normalized using area-averaged rotor inlet condition from steady results. The wall heat flux is calculated using monitored wall adjacent temperature. In Fig. 5.4a, the periodic patterns of the flow field can be observed for both adjacent blades with a phase lag of the half vane pitch. The amplitude of pressure fluctuations is about 20% of the averaged rotor inlet pressure. The maximum pressure is greater than the mean rotor inlet pressure. The critical phenomena of pressure fluctuation are to be discussed with the leakage flow structure variation. At an instant t*=0.125, the tip leakage flow velocity increases through the gap of the front blade, thus is expanding the separation zone. As a result, a low pressure exists (A) at this point since the leakage flow reattachment occurs beyond the monitoring point. As the time progresses, the leakage flow reattachment point moves closer to the monitoring point since the leakage flow speed is gradually decreasing. A peak pressure (B) is due to relatively low speed leakage flow. The pressure is then reduced to a lower value (C) where the leakage velocity increases further. The lowest speed of the leakage flow near this monitoring point is observed at D where the pressure reaches maximum value. The variations of the pressure at the blade tip are signifying the nature of the leakage flow unsteadiness inside the tip clearance region. Eventually, the pressure is low in the separation zone and become high at the tip leakage flow re-attachment. And this leakage flow structure varies

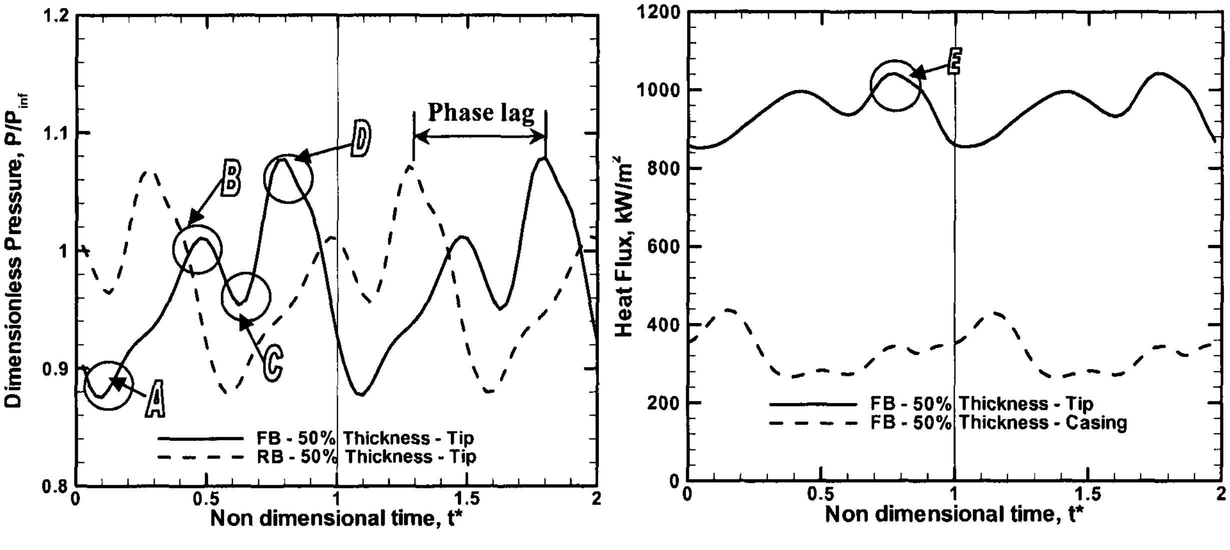

(a) Dimensionless Pressure

(b) Heat Flux

Figure 5.4 Time histories inside the tip clearance at different locations in the quarter axial chord plane. (Case: 9500 rpm; 1.2 mm) with time. The heat flux variations with the time are presented (Fig. 5.4b) at two points to capture the effect of reverse cross flow and leakage flow reattachment. The heat flux is significantly lower on the casing at this monitoring point than that on the tip surface. Because this monitored point is in relatively low temperature reverse cross flow coverage. On the other hand, when the leakage flow is reattached on the tip surface the boundary layer insulation becomes very thin and thus, increases the wall heat flux. At the instant of t*=0.75, the heat flux reaches the peak point (E) due to the flow reattachment point is at a closest distance of the monitoring point. It is then gradually decreasing since the attachment point shifting away from the monitoring point due to increase of leakage flow speed. The maximum amplitude of the heat transfer rate fluctuation on the blade tip, caused by the unsteady leakage flow structure variations, reaches up to about 25% of the mean heat transfer rate. Therefore, the high pressure and heat flux fluctuations should be considered to understand and design the tip clearance region.

5.3.3 Tip leakage Flow Structural Variation

In this unsteady simulation, the instantaneous tip leakage flow and heat transfer data were captured at eight equal time instants for each vane passing period. For simplicity, the results have been presented here at two selected instants of t*=0.25 and 0.5. In one stator pitch, there are two adjacent blades demonstrating the same periodic behavior with half-period phase lag (Fig. 5.4). Therefore, four different features in one period can be seen using only two selected instants with two adjacent blades.

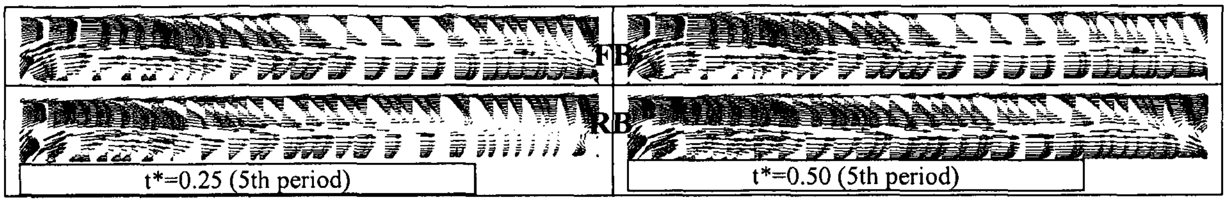

(a) 0.6 mm

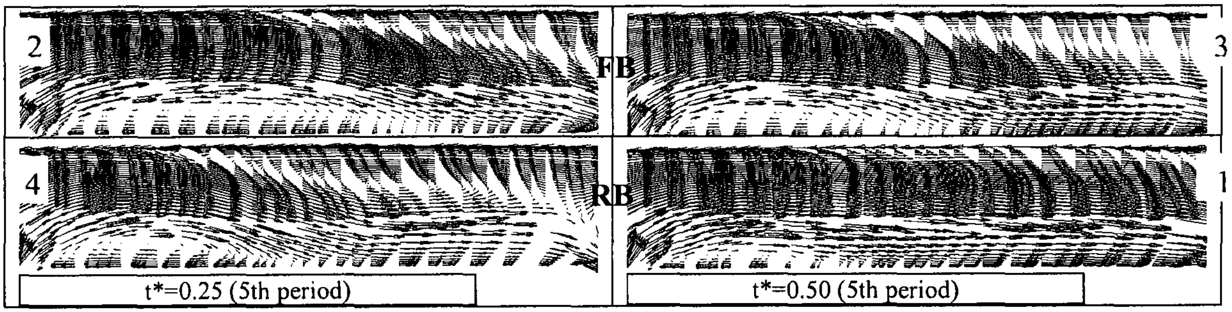

(b) 1.2 mm

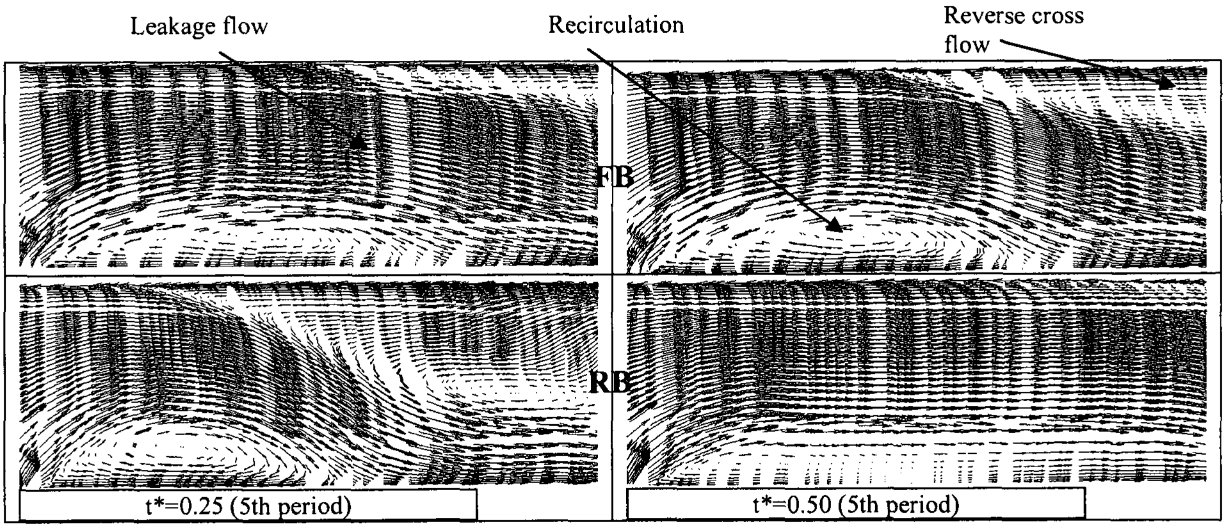

(c) 2 mm

Figure 5.5 Velocity vectors at quarter axial chord plain for different clearance heights.

Leakage flow patterns, at different time instants, are visualized using 2D velocity vector diagrams in Fig. 5.5, for both the front and the rear blades at the quarter axial chord plane. Leakage flow recirculation zone, reattachment and the critical line of zero v-velocity (the major consequences of the flow complexity) are apparent in these vector diagrams. In general, leakage flow entering the tip gap from the pressure side with sudden change in directions causes the flow to be separated from the tip surface. Flow then reattaches on the surface beyond the separation zone. These typical flow structures were also seen in the steady simulation. However, unsteady simulation can predict to what extend the variations might occur due to upstream flow unsteadiness. At each instant, the flow structures inside the tip regions of two neighbor blades are different. The tip leakage flow structure variation follows the sequence of 1-4 (Fig. 5.5b). This flow variation could be attributed to the change of the influence of the upstream wakes and the stator trailing edge shock during vane passing period, such as, the change of flow incidence and so on. From the vector visualization, it is observed that at the time, $t^*=0.5$, reverse cross flow shows minimum interaction with the leakage flow in the rear blade region (blade 1). This might be because of the smallest inlet flow angle and highest pressure flow due to the shock (see Fig. 5.2). As a result, the higher velocity leakage flow (which is mostly normal (90^0) to the reverse cross flow direction) dominates over the reverse cross flow in the tip region. As the rotor blade rotates, the relative position is changing. As a result, the inlet flow angle increases (Fig. 5.3) and the leakage flow structure varies from 1 to 4 in Fig. 5.5b. Finally, in the rear blade (blade 4), at the time of $t^*=0.25$, it has the highest inlet flow angle and lowest pressure flow. The leakage flow is almost opposite (180^0) to the reverse cross flow direction. As a result, the reverse cross

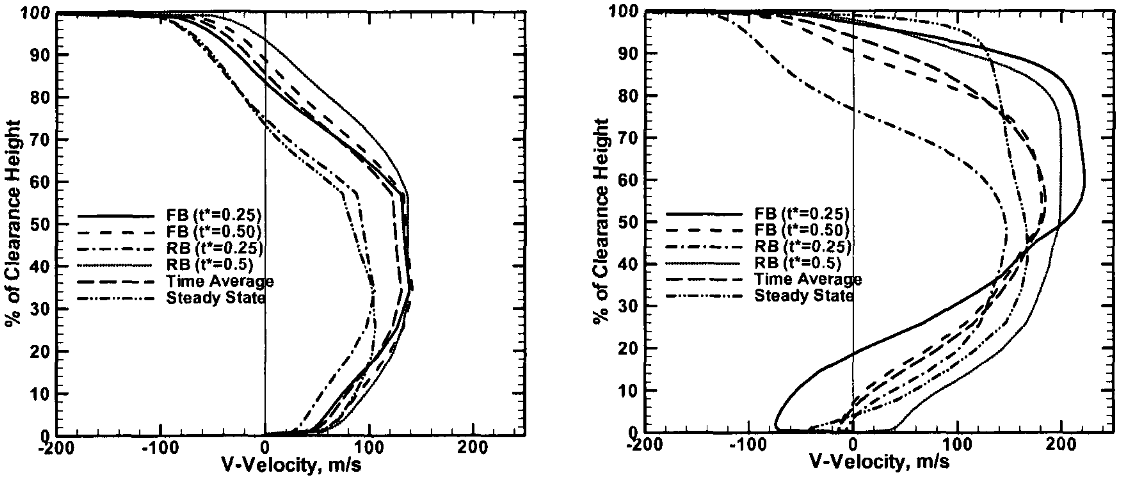

(a) 0.6 mm

(b) 1.2 mm

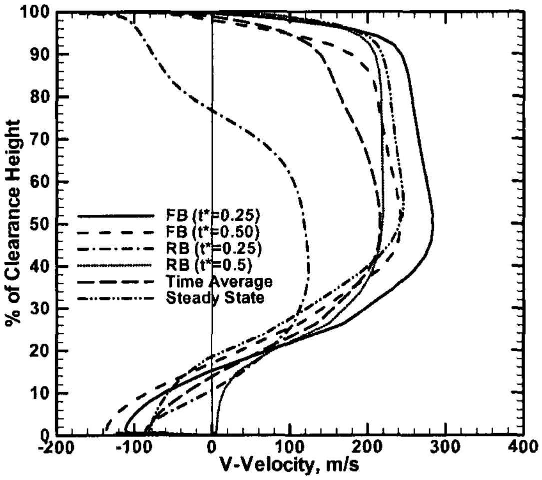

(c) 2 mm

Figure 5.6 V-velocity profile clearance region at $x/C_x = 25\%$; $y/t_y = 50\%$ for different clearance heights.

flow has significant coverage in the clearance region. The same typical leakage flow structure can be observed for other clearance heights as well (Fig. 5.5). Thus, it may be concluded here that the leakage flow velocity is considerably increases with the increase of the clearance heights and shows highly time dependent in nature with larger flow separation and high reverse cross flow coverage. In contrast, the reverse cross flow becomes relatively dominant as the clearance height decreases due to the leakage flow weakening.

To investigate the local velocity variation of the tip leakage flow and to explain the effects of opposing movements of the leakage flow and casing, v-component of the velocity in the clearance region is considered. In Fig. 5.6, the velocity distributions are plotted for both front and rear blade against the normalized height of the tip gap at a location of $y/t_y = 50\%$ and $x/C_x = 25\%$. The unsteady results, at t*=0.25 and 0.5, are compared with time averaged and steady results for all clearance heights. As seen in Fig. 5.6b, the maximum variation of the local v-velocity reaches up to about 250 m/s near the casing, due to variation of the balance between the leakage flow and reverse cross flow. At t*=0.5, in the rear blade (blade 1 in Figs. 5.2 & 5.5), the leakage flow is seen to have dominating the clearance region while the reverse cross flow appears above 95% of the clearance height. This might be attributed to the effect of trailing edge shock progressing to the rotor section. The shock causes the high pressure concentration in front of the rear blade (blade 1 in Fig. 5.2b), thus, increasing the leakage flow velocity due to higher pressure difference. However, at an earlier time instant (t*=0.25), this pressure concentration does appear in the front blade (blade 2 in Fig. 5.2a) which further induces the reverse cross flow, inside the gap in the rear blade (blade 4), due to high pressure gradient along the normal to the passage flow. The significant height of the separation, about 21% of the gap, appears in the front blade (blade 2) at a time instant of t*=0.25. The reverse cross flow has shown maximum clearance coverage in the rear blade region (blade 4 in Figs. 5.2 & 5.5), which is approximately 80% of the clearance height at the instant of 0.25. Steady predictions have shown flat velocity distribution (Fig. 5.6b), whereas the time average prediction is mostly parabolic. At a smaller clearance, steady prediction has captured the stagnation point of v-velocity far from the casing, while the time instant data varied near the casing. The maximum deviation between steady and time average data (Fig 5.6a) is about 35% at the mid clearance. At a higher clearance (2mm), the maximum interaction of the leakage flow with the reverse cross flow is observed where the point of zero v-velocity falls around 75% of the clearance height at the same time instant (t*=0.25). The maximum leakage flow velocities are observed to be 140 m/s, 210 m/s and 280 m/s, respectively, for small, medium and large clearance gap. As the clearance height increases, the variation of the velocity profile becomes severe. Time average data show the intermediate values in the instantaneous data. However, the steady prediction represents the typical structure close to one of the instantaneous profile. Thus, the steady prediction could not show the critical profiles, such as, the maximu and the minimum.

5.3.4 Heat Transfer Rate Distribution Variation

The unsteady heat transfer data were recorded on the rotor casing and blade tip and analyzed with the time averaged as well as steady solutions. The time averaged data are computed from the unsteady data (during the fifth vane pass). Figure 5.7 shows contours of the Nusselt number on the casing for the case of 9500 rpm speed and 1.2 mm clearance height. The effect of the relatively lower temperature reverse cross flow and higher temperature leakage flow on the heat transfer rate distribution over the casing is visible. The casing heat transfer rate distribution shows unsteadiness in nature. It is attributed to the unsteady behaviors of the upstream incoming flow, such as wakes, shock, and vane passing. These results in the variations of the balance of tip leakage flow and reverse cross flow. Eventually, the higher heat transfer rate region moves back and forth circumferentially with changing the slope during the period. It is also observed in Fig. 5.7, that the larger and higher heat transfer rate regions occur at front blade (blade 2) of t*=0.25 and rear blade (blade 1) of t*=0.5. These blades have the dominant leakage flow with the higher pressure region in the pressure side of the blade caused by the trailing edge shock (Fig. 5.2) and small inlet flow angle (Fig. 5.3). In the time averaged heat transfer rate distribution, we can see the smeared heat transfer rate between the high and low heat transfer regions due to the averaging. The steady heat transfer rate distribution is close to that of certain instantaneous case (blade 4 at t*=0.25) which has the smallest area of high heat transfer rate region and the largest reverse cross flow coverage because of the lowest pressure in the pressure side and the opposite direction of the leakage flow to the reverse cross flow. Finally, steady simulation might overestimate the effect of reverse cross flow and underestimate the high heat transfer rate region due to neglecting unsteady effects caused by the trailing edge shock and wake from the upstream stator section. However, the overall leakage flow structure, heat transfer rate distribution pattern, as well as the range of heat transfer rate can be well predicted in steady simulations.

Nusselt number distributions along the casing circumference at 25% axial chord from line of projections of the blade tip pressure and suction side edges for all clearance heights are plotted in Fig. 5.8. It is seen that the maximum heat transfer rates exists near the pressure side edge, whereas at the suction side the heat transfer is lower. Therefore, the casing undergoes the change of heat transfer rates around Nu=2000 to 7000, by the rotor blade passing. The pressure on the blade pressure side near the leading edge increases due to shock, thus, induces higher tip leakage flow velocity. The increased leakage flow velocity is then strongly opposing the incoming flow (reverse cross flow) from the suction side which has relatively lower temperature. For the other clearance heights, the maximum heat transfer fluctuation is about 78% (1.2 mm) and 83% (2 mm). As seen in Fig. 5.8a, for smaller clearance heights, the heat transfer distribution is stepper. Sudden increase of heat transfer (jump up) indicates the high temperature gradient on the casing surface. As a result, the thermal stresses are expected to be higher which may cause major consequences to the casing metal. Heat transfer rate is distributed more evenly along the circumferential direction as the clearance heights increases. The highest spreading of the high heat transfer region is observed in the rear blade at t*=0.5 (Fig. 5.8c), while the distributions are relatively sharp at t*=0.25 in the rear blade region. This is because the reverse cross flow (which has relatively low temperature) can strongly interact with the leakage flow at t*=0.25 (Fig. 5.5c) and detach the leakage flow from the casing. However, in the rear blade region, at the instant of t*=0.25, the distributions are consistently stepper at all heights of the clearance. Steady predictions underpredicted the high heat transfer region. However, the pattern of heat transfer rate distribution can be captured by the steady predictions. On the other hand, time averaged data (Fig. 5.8d)

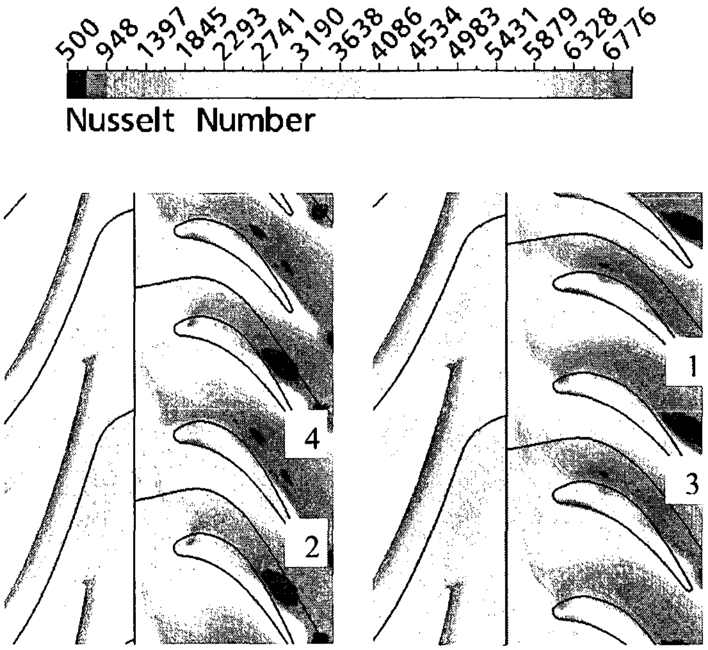

(a) t*=0.25 (5th period) (b) t*=0.5 (5th period)

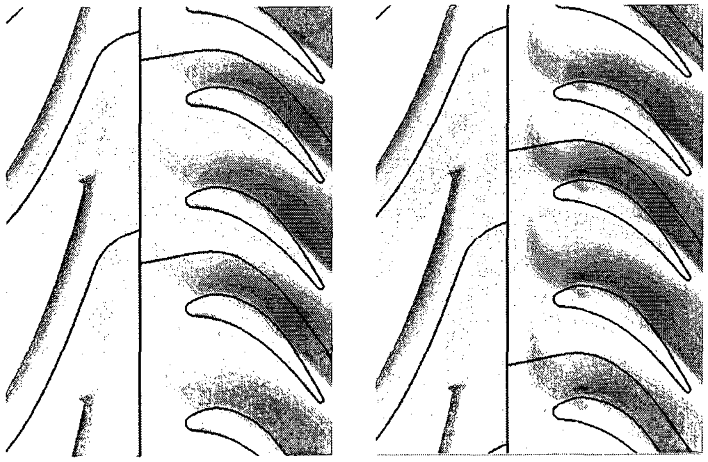

(c) Time average (d) Steady

Figure 5.7 Nusselt number contours on the casing (Case: 9500 rpm; 1.2 mm).

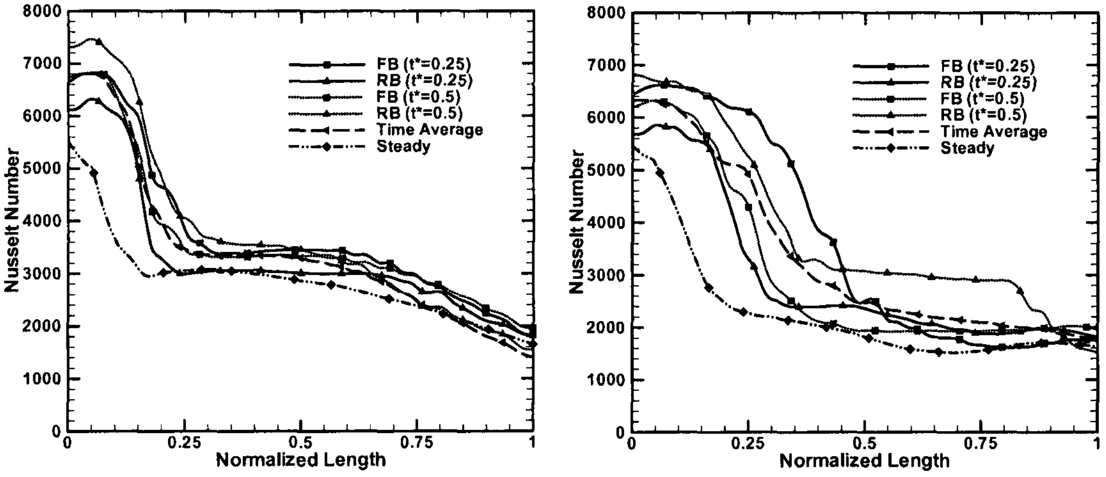

(a) 0.6 mm

(b) 1.2 mm

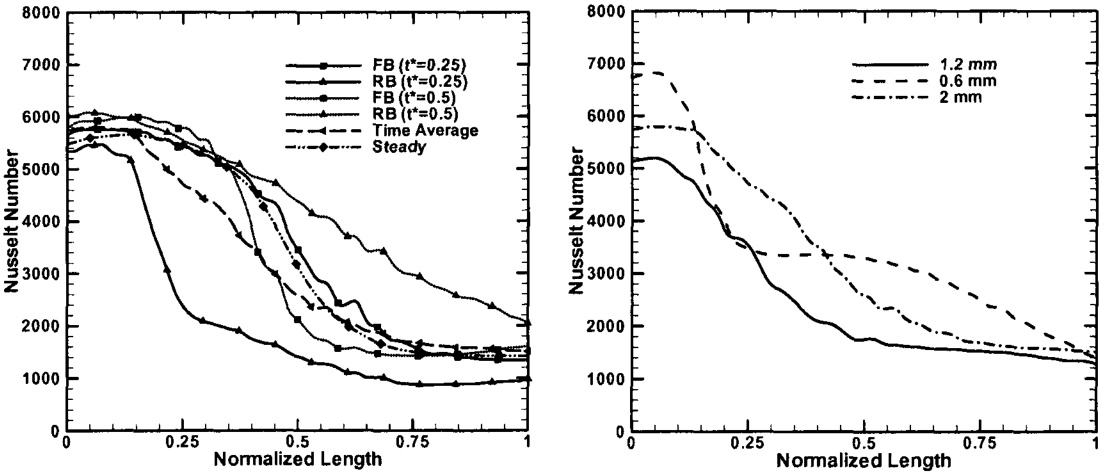

(c) 2 mm

(d) Time Average

Figure 5.8 Nusselt number distribution along casing circumference at 25% chord from line of projections of blade tip pressure to suction.

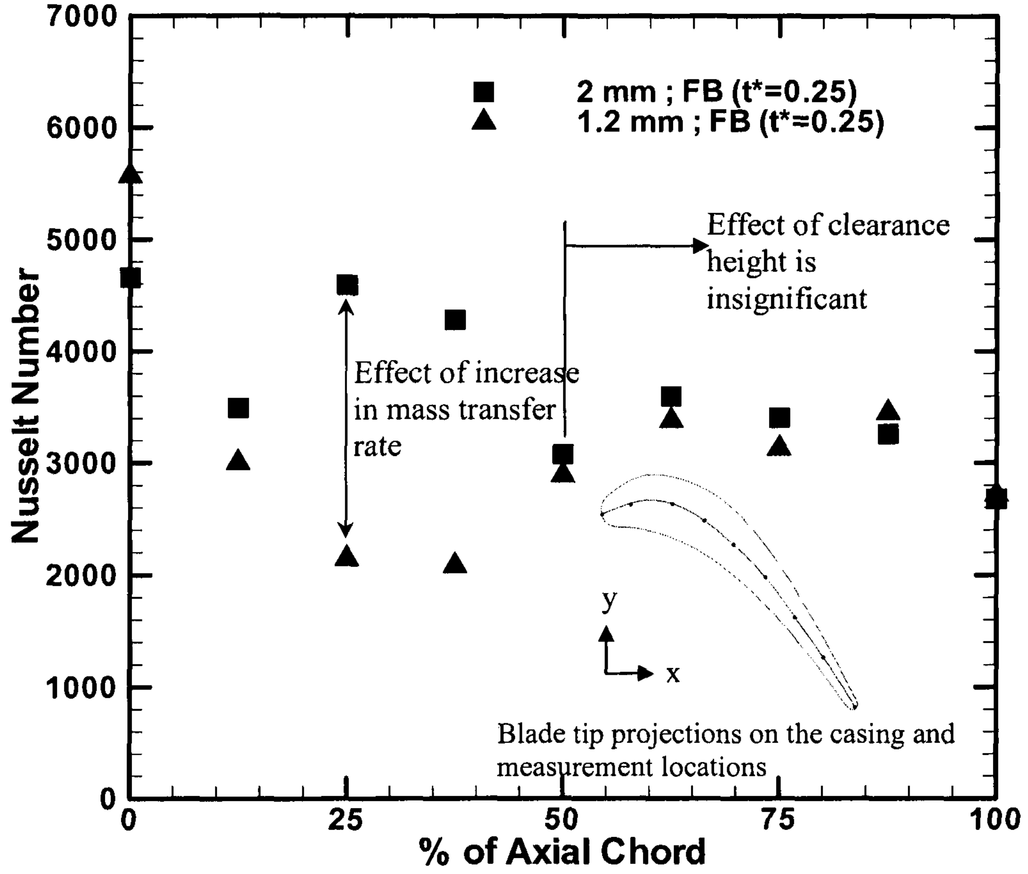

Figure 5.9 Nusselt number along the camber on the casing for different clearance heights.

shows higher heat transfer rate near the pressure side and much stepper for smallest clearance height in compare to higher clearance heights. Medium height (1.2 mm) has the minimum heat transfer rate at this location. For the smaller clearance heights, the leakage flow is reduced and the coverage of the reverse cross flow becomes thinner. Thus, it has a high heat transfer rate. For the larger clearance heights, the larger leakage flow induces higher heat transfer rate. Based on this phenomenon, we come to a conclusion that there can be an optimal clearance height between the gap of 1% (0.6 mm) and 5% (2 mm) of the span at which the heat transfer rate could be lowest.

Figure 5.9 is presented in order to see the heat transfer variations along the camber line on the casing from leading edge to trailing edge for medium (1.2 mm) and high (2mm) clearance heights. At a time step of t*=0.25, the effect of increase in mass transfer rate through the gap are significant from $x/C_x = 10\%$ to 50%. It is already discussed in steady analysis that the larger pressure drop through the tip gap for larger clearance heights results in higher speed of leakage flow. And then the tip leakage flow becomes stronger than the reverse cross flow for higher clearance height. As a result, the heat transfer at the high clearance height is observed two times higher in compare to that of medium clearance height, at a location $x/C_x = 25\%$. However, beyond $x/C_x = 50\%$, the effects of clearance heights are seen insignificant because of dominant leakage flow regardless clearance heights caused by the smaller thickness of the staggered blade.

Figure 5.10 shows the Nusselt number distributions on the blade tip surface at different time instants as well as the time averaged and steady predictions. The low and high heat transfer regions on the tip surface are strongly related with the leakage flow separation and reattachment. The size and location of the leakage flow separation and reattachment are affected by the flow incidence angle and pressure distribution. Along the leakage flow passage from pressure to suction sides, the typical heat transfer distribution on the tip surface can be seen for the blade 2, 3, and 4; low heat transfer rate near pressure side by separation, high heat transfer rate by leakage flow reattachment, and heat transfer rate decreasing again by mixing between the leakage flow and reverse cross flow. The inlet flow angle increases with the sequence of 2-3-4, thus, the high heat transfer region, caused by the reattachment, also moves normal to the leakage flow direction. However, for the blade 1, it has smallest inlet flow angle (close to axial direction) and highest pressure flow due to the shock (Fig. 5.2). At this instant, the effect of the reverse cross flow was seen lowest (Fig. 5.5) due to high speed leakage flow. As a result, Nusselt number gradually increases toward the suction side. Although the significantly different heat transfer rate distributions can be seen at each blade with time variation, we can see the almost same heat transfer rate distribution on both blades after time averaging. It represents the periodic characteristics of the unsteady tip leakage flow and heat transfer rate. The steady heat transfer rate distribution showed the typical distribution pattern close to the time averaged data. However, it couldn't show the locally and instantaneously higher heat transfer features.

The contour of the Nusselt number on the rotor casing and tip surface is also presented in Figs. 5.11 and 5.12 for 12500 rpm speed of the rotor and 1.2 mm gap. At a higher rotating speed, the high heat transfer regions were shifted to the mid chord along the

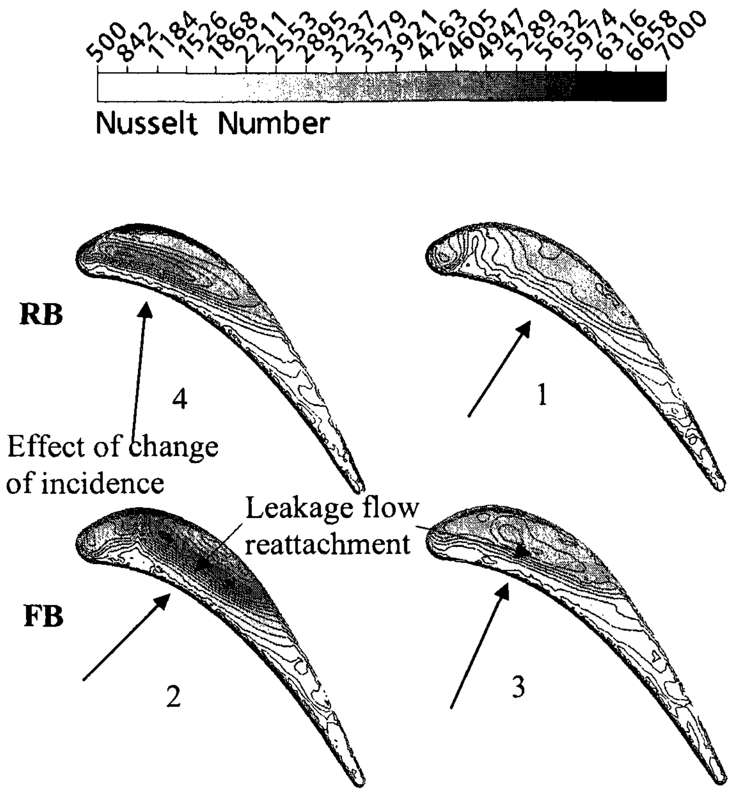

(a) t*=0.25 (5th period)   (b) t*=0.5 (5th period)

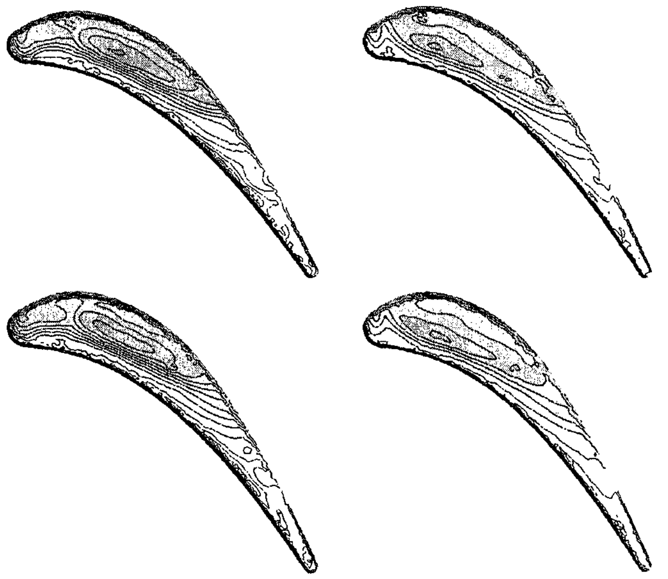

(c) Time average   (d) Steady

Figure 5.10 Nusselt number contours on the blade tip (Case: 9500 rpm; 1.2 mm).

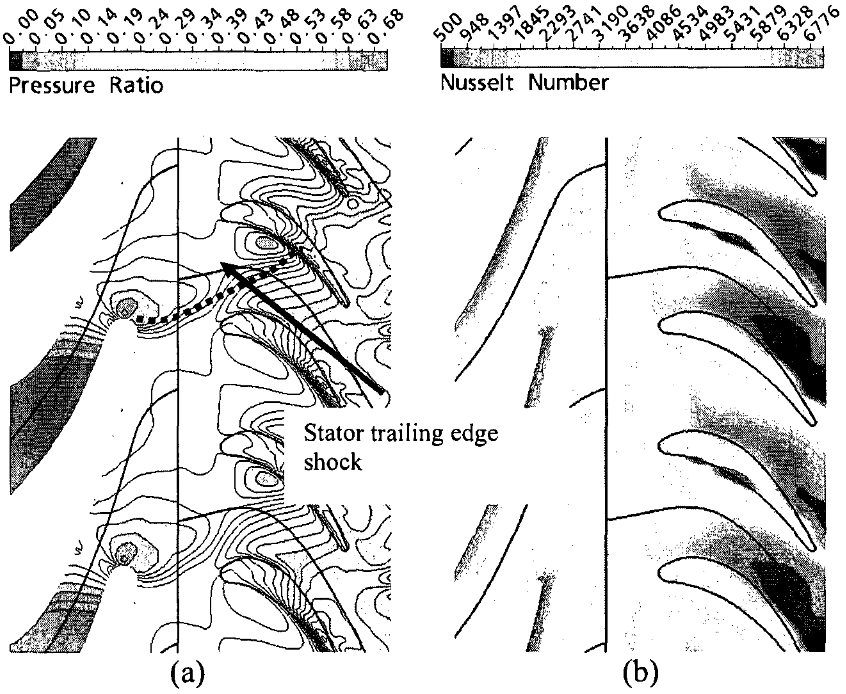

t*=0.125 (5th period)

Figure 5.11 Contour of (a) pressure ratio at mid span and (b) Nusselt number on the rotor casing for the rotor speed of 12500 RPM.

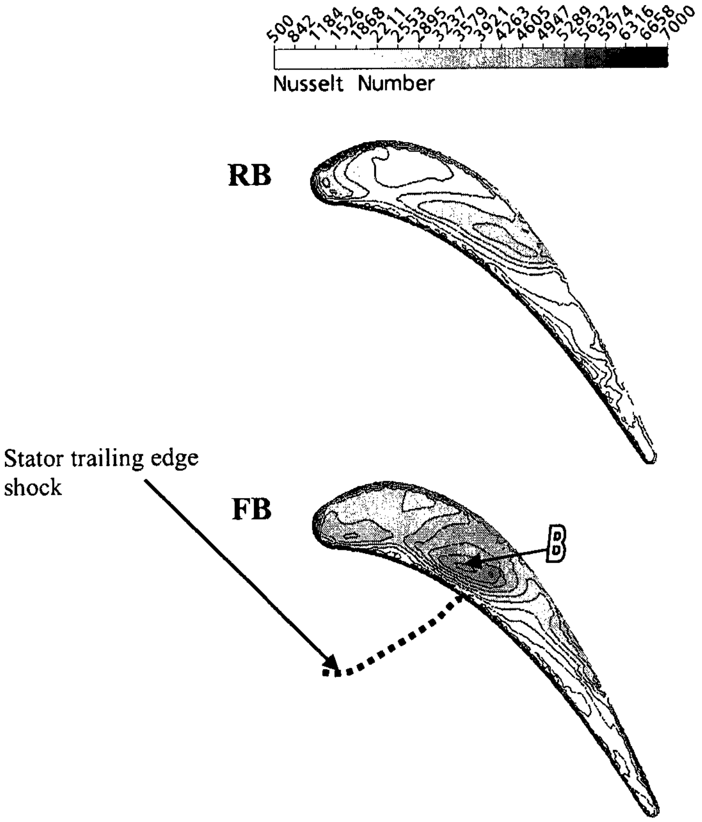

t*=0.125 (5th period)

Figure 5.12 Contour of Nusselt number on the rotor blade tip for the rotor speed of 12500 RPM.

pressure edge due to the change of flow incidence as observed in steady analysis [Chapter 4]. The effect of stator trailing edge shock on the local heat transfer rate becomes severe for higher rotation speed. The higher heat transfer rates were observed at the region where the trailing edge shock reached, for both of casing (Fig. 5.11) and tip surface (Fig. 5.12). Eventually, the heat transfer behaves strongly time dependent due to upstream flow unsteadiness. This behavior could not be captured by steady simulations. Therefore, unsteady simulation should be performed particularly for high speed gas turbine engine.

In order to explain the cause of high critical heat transfer region (B) in Fig. 5.12, 3D pathlines of the leakage flow is presented in Fig. 5.13. As seen in the figure, the leakage flow reattaches on the tip at B with higher impingement effect, might be due to the shock (Fig. 5.12) and the change of inlet flow angle (Fig. 5.3 b).

The effect of rotor speeds on the casing camber line heat transfer distributions are illustrated in Fig. 5.14. As it is seen in steady analysis that the leakage flow dominate in downstream region for higher rotor speeds, whereas the upstream region of the tip clearance is dominated by the reverse cross flow. As a result, at a higher speed the heat transfer rate is lower at the upstream region in Fig. 5.14. Casing leading edge at 9500 rpm has 60% higher heat transfer rate than that of 12500 rpm. However, as the speed increases, the heat transfer is increased in the downstream region (beyond mid chord) and is seen 48% higher compared to the low speed case at $x/C_x = 65\%$. This is again, as discussed earlier, due to dominant leakage flow beyond the mid chord caused by the change of flow angle.

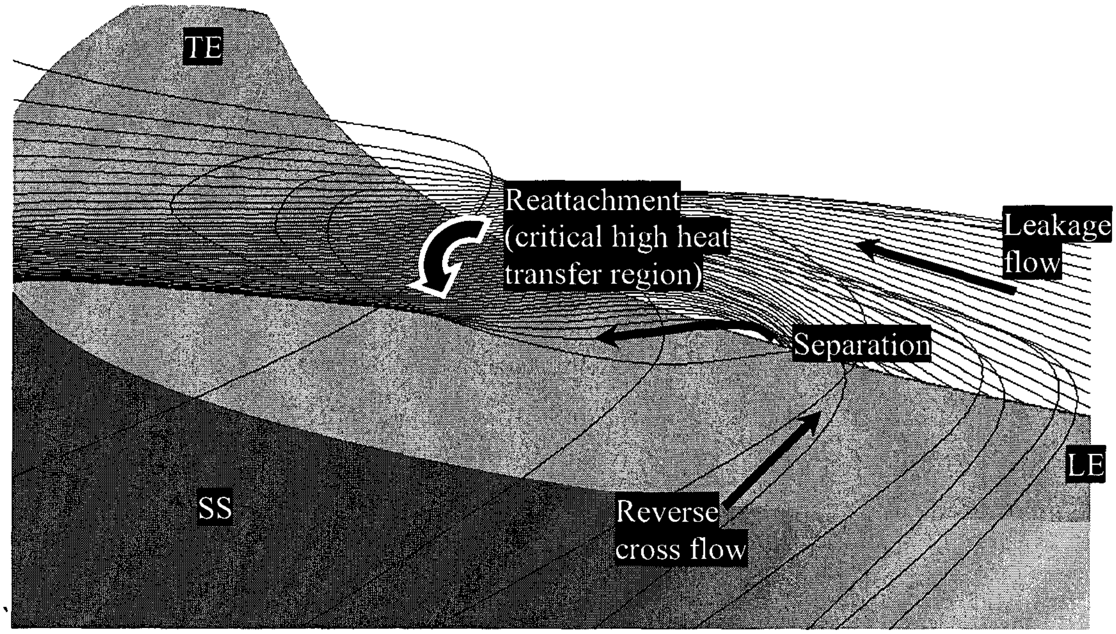

Figure 5.13 Effect of the flow at a location of high heat transfer as indicated in Fig. 5.12.

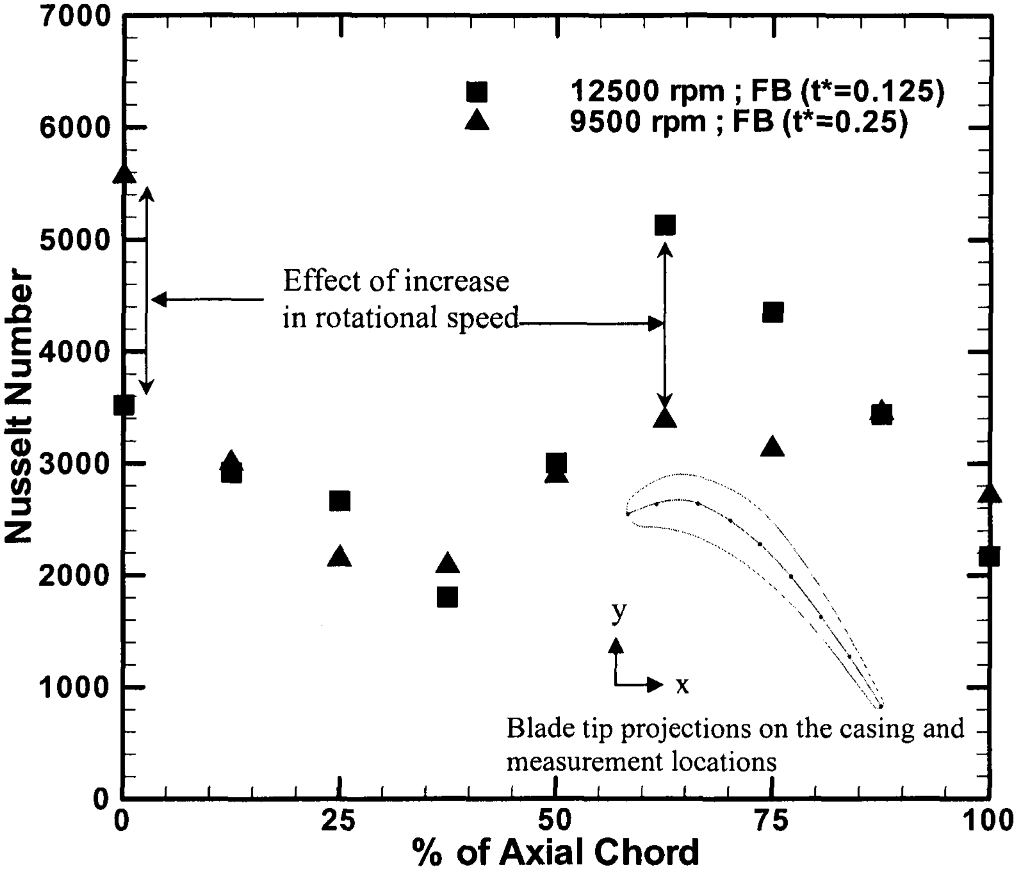

Figure 5.14 Nusselt number along the camber on the casing for different rotor speeds.

Figure 5.15 presents the relative comparison of maximum heat transfer rate values of the instantaneous, time-averaged and steady data on the casing for different clearance heights and speeds. The area-averaged mean values are also depicted in Fig. 5.15. The figure is only presented for the casing since the maximum heat transfer rate is observed relatively higher than the heat transfer rate on the blade tip surface. From the maximum heat transfer trend, it is observed that the heat transfer rate decreases as tip gap increases (Fig 5.15 a), however, the area-averaged Nusselt number slightly increases. For a given clearance height, a highest heat transfer rate is evident at medium rotor speed (Fig. 5.15b). The maximum Nusselt number is 21%, 29% and 45% of the maximum time averaged value, respectively, for 0.6 mm, 1.2 mm and 2 mm gaps. On the other hand, at a medium speed the heat transfer rate is observed as high as 68% of the maximum time averaged value. Steady simulation could not capture this kind of critical high local value. However, it can provide closer values to the time averaged values.

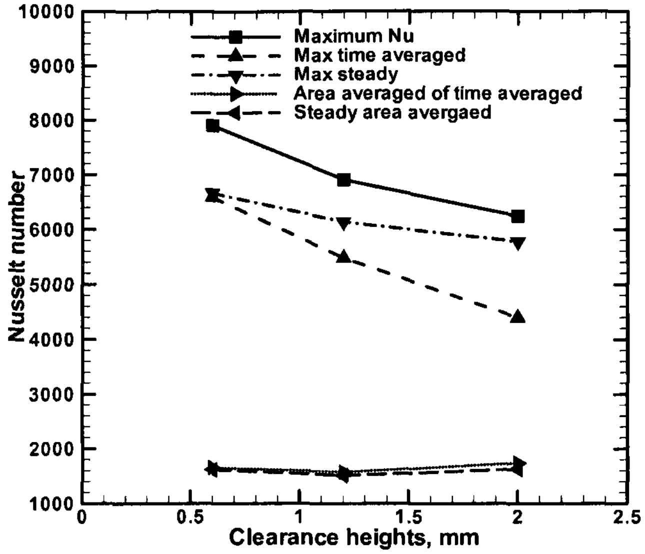

(a)

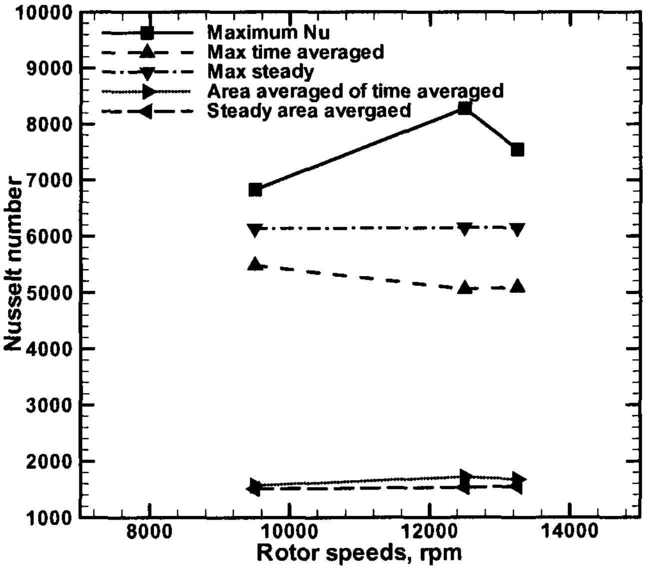

(b)

Figure 5.15 Comparison of critical heat transfer value for (a) clearance heights and (b) rotor speeds.

Chapter 6

Summary and Conclusions

Turbine cooling plays a vital role to the overall performance improvement of the turbine engine. It is still a major concern for the turbine cooling designer in identifying the region of high thermal load where cooling is required. This study was mainly conducted with an intention to lead the designer to optimize cooling area required for the turbine casing and blade tip and help them to understand the heat transfer characteristics associated with complex tip leakage flow. The main focus of this study was to investigate the effect of different clearance heights and rotation rates of the blade on both the leakage flow aerodynamics and the heat transfer unsteadiness. A high pressure ratio single stage turbine model was adopted in this study. The experimental and numerical data from the work of Chana and Jones [12, 13], Hilditch et al. [40], and Roux et al. [39] were adopted to compare with the steady numerical predictions and found in reasonable agreement. For the unsteady simulations, two different non dimensional time steps of 0.25 and 0.5 of the stator vane passing period were analyzed to account the effects of upstream wake and stator trailing edge shock. Numerical validations for different time step sizes, number of sub iteration and number of stator vane pass were tested for time accurate predictions to ensure a reasonable accuracy of the solutions.

From the steady simulations, it was observed that tip leakage flow structure is highly dependent on the height of the tip gap as well as the rotor speeds. Flow separation occurs near the pressure side edge of the blade tip for all clearance heights. In this separated flow region, the heat transfer rate was seen lower because of low temperature and low pressure separation zone. Just beyond the separation zone, the leakage flow is reattached on the tip surface. This leakage flow reattachment contributed to the blade tip surface heat transfer enhancement. It was also observed that the point of flow reattachment on the tip surface tends to move towards the suction side as the clearance heights increases. On the other hand, the critical region of high heat transfer on the casing exists above the blade tip leading edge that continues along the pressure side edge at all clearance heights. However, at high speed rotation, it tends to move downstream region due to change of inlet flow angle and the enhanced effect of casing relative motion.

For high speed case (15500 rpm), the heat transfer rate on the casing, at the pressure edge of $x / C_x = 75\%$, is increased by 32% than the low speed case. The maximum heat transfer rate, at a medium speed, decreases by 20% compared to the low speed case. For the higher speed (15500 rpm), the distribution is more flattened at 25% axial chord location because the entire area is filled by the colder reverse cross flow. On the other hand, at a further increasing the speed (15500 rpm), the maximum heat transfer reduction is about 42% in compare to low speed case. However, the critical region of high heat transfer for the high speed case (15500 rpm) appears close to the trailing edge where the heat transfer rate increases 32% than the low rotation speed case due to the high speed leakage flow attachment to the casing. When the rotor speed increases higher (15500 rpm), a complex flow mixing occur between upstream main flow, leakage flow and reverse flow within the quarter chord region. This complex phenomenon results in some critical region of heat transfer distribution on the blade tip surface.

For the unsteady simulation, the effect of stator trailing edge shock has been observed significant under this transonic operating condition. It was seen that the relative change in the position of the shock and vane alters the flow inlet directions at the rotor domain and results in the variations of the leakage flow structures and heat transfer rate distributions. In general, for any clearance heights with a constant speed, reverse cross flow dominates the rear blade tip region at t*= 0.25, while the frontal blade region shows maximum leakage flow coverage. On the other hand, reverse cross flow has been strongly opposed by the leakage flow, at a time t*=0.5 in the rear blade, due to presence of stator trailing edge shock. For the higher clearance height, a significant coverage of the reverse cross flow observed at a time instant of 0.25 in the rear blade region at $x/C_x = 50\%$.

For higher clearance height, the casing heat transfer is more evenly distributed at almost all time instants in compared to smaller clearance heights. Therefore, it may be concluded here that, as long as the thermal stress is concerned, higher clearance gap is preferable. However, high clearance gap involves significant aerodynamic losses since the leakage vortex increases in size due to high mass transfer through the gap which was not taken into account in this study. On the other hand, for smaller clearance height, the heat transfer distribution on the casing is stepper. This sudden increase of heat transfer rate indicates high temperature gradient on the casing surface. Furthermore, at a fixed height of the clearance, increasing rotor speeds reduces the flow separation and allows more coverage of the reverse cross flow inside the gap. Based on the results of both steady and unsteady simulations, it may be concluded that similar typical leakage flow structures and heat transfer rate distribution patterns are obtainable for either cases. However, steady simulation somewhat underpredicted the heat transfer rate and couldn't capture the critical local high heat transfer phenomena. Moreover, the tip leakage flow and heat transfer rate distribution is seen periodically steady for each vane passing.

Based on the relative comparison of heat transfer rate values of the instantaneous, time-averaged and steady data on the casing for different clearance heights and speeds, it is observed that the heat transfer rate decreases as tip gap increases, however, the area-averaged Nusselt number slightly increases. For a given clearance height, a highest heat transfer rate is evident at medium rotor speed. The maximum Nusselt number is 21%, 29% and 45% of the maximum time averaged value, respectively, for 0.6 mm, 1.2 mm and 2 mm gaps. On the other hand, at a medium speed the heat transfer rate is observed as high as 68% of the maximum time averaged value. Steady simulation could not capture this kind of critical high local value. However, it can provide closer values to the time averaged values.

Chapter 7

Future Directions and Recommendations

Turbine tip leakage flow and casing heat transfer has been the major interest for both the researchers and turbine manufacturers since gas turbine engine is the foremost means of producing useful work. In the recent years, need for increasing energy demand has been attracting the awareness of improving the turbine performance and efficiency. Turbine tip leakage flow has a major role in deteriorating the turbine efficiency by several percentages. The only way to recover this efficiency is to keep the leakage flow as low as possible. It is very obvious that reducing the clearance heights will eventually decrease the leakage flow mass transfer through the gap which is expected. However, the possibilities of surface rubbing between the tip and casing will increase significantly which is absolutely undesirable from turbine safety view point. Therefore, it is highly important to implement the leakage flow reduction technique with keeping the safe allowances between the tip and casing. In the recent years, there have been several such techniques reported in the open literature. A recessed tip with different geometric configurations can reduce the leakage flow significantly in compared to a flat tip surface. However, no universal methods have been recommended that could reach the target level of safety issue. This current study can be further extended by implementing some design methodology for the turbine tip geometry configurations. On the other hand, a novel technique of the film cooling holes might also be introduced on the casing or the blade tip surface to minimize the leakage flow and heat transfer as well.

Inlet temperature variation in regard to the actual temperature distributions in the combustor exit may also be included in the future simulations. In this present study, the inlet temperature was specified as 444 K following the experimental work of Chana and Jones [12, 13]. It is also recommended to extend this work further considering higher inlet temperature condition that could be the more realistic representation of the turbine operating condition.

In the current study the geometric heights of the clearance was kept constant in both steady and unsteady simulations. However, in actual case when turbines are operating at higher rotating speed the centrifugal growth of the turbine metal can no longer be neglected. In contrast, turbine material properties are also related to the temperature. The temperature is not entirely constant over the surfaces which may cause uneven surface deformation. As a result, the geometric gap of the clearance will be varying with the rotor speeds as well as surface temperature distribution. Therefore, the existing work may be further extended by coupling FEA (Finite Element Analysis) method in order to optimize the minimum critical height of the clearance under the same operating condition.

References

1. Tallman, J., and Lakshminarayana, B., "Numerical Simulation of Tip Leakage Flows in Axial Flow Turbines, With Emphasis on Flow Physics: Part I- Effect of Tip Clearence Height", Journal of Turbomachinery, Vol. 123/314, 2001.

2. Tallman, J., and Lakshminarayana, B., "Numerical Simulation of Tip Leakage Flows in Axial Flow Turbines, With Emphasis on Flow Physics: Part II- Effect of Outer Casing Relative Motion", Journal of Turbomachinery, Vol. 123/325, 2001.

3. Han, J. and Azad, G. M. S., "Detailed Heat Transfer Coefficient Distributions on a Large Scale Gas Turbine Blade Tip", Journal of Heat Transfer, Vol. 123/803, 2001.

4. Eriksson, D., Mumic, F., and Sunden, B., "On Predction of Tip Leakage Flow and Heat Transfer in Gas Turbines", Proceedings of ASME Turbo Expo, 2004, GT2004-53448, 2004.

5. Key, N. L. and Arts, T., "Comparison of Turbine Tip Leakage Flow for Flat Tip and Squealer Tip Geometries at High-Speed Conditions", Journal of Turbomachinery, Vol. 128, pp. 213-220, 2006.

6. Schabowski, Z., and Hodson, H., "The Reduction of Over Tip Leakage Loss in Unshrouded Axial Turbines Using Winglets and Squealers", Proceedings of ASME Turbo Expo, 2007, GT2007-27623, 2007.

7. Han, J. and Kwak, J. S., "Heat Transfer Coefficients on the Squealer Tip and Near Squealer Tip Regions of a Gas Turbine Blade", Journal of Heat Transfer, Vol. 125/669, 2003.

8. Newton, P. J., Lock, G. D., Krishnababu, S. K., Hodson, H. P., and Dawes, W. N., Hannis, J., and Whitney, C.,"Heat Transfer and Aerodynamics of Turbine Blade Tips in a Linear Cascade", Journal of Turbomachinery, Vol. 128, Issue 2, pp. 300-309, 2006.

9. Lamyaa, A., "Numerical Modeling of Heat Transfer and Pressure Losses for an Uncooled Gas Turbine Blade: Effect of Tip Clearence and Tip Geometry", Proceedings of ASME Turbo Expo, 2007, GT2007-27008, 2007.

10. Yamamoto, A., Matsunuma, T., Ikeuchi, K., and Outa, E., "Unsteady Endwall/Tip-Clearance Flows and Losses Due to Turbine Rotor-Stator Interaction", American Society of Mechanical Engineers (Paper), 94-GT-461, pp. 1-10, 1994.

11. Kumada, M., Iwata, S., Obata, M., and Watanable, O., "Tip Clearance Effect on Heat Transfer and Leakage Flows in the Shroud-Wall Surface", Journal of Turbomachinery, Vol. 116, pp. 39-45, 1994.

12. Chana, K. S., and Jones, T. V., "An Investigation of Turbine Tip and Shroud Heat Transfer", Journal of Turbomachinery, Vol. 125, pp. 513-520, 2003.

13. Chana, K. S., and Jones, T. V., "Heat Transfer And Aerodynamics Of An Intermediate Pressure Nozzle Guide Vane With And Without Inlet Temperature Non Uniformity", Proceedings of ASME Turbo Expo 2003, GT2003-38466, 2007.

14. Polanka, M. D., Hoying, D. A., and Meininger, M., "Turbine Tip And Shroud Heat Transfer And Loading-Part-A: Parameter Effect Including Reynolds Number, Pressure Ratio, And Gas To Metal Temperature Ratio", Journal of Turbomachinery, Vol. 125/97, 2003.

15. Thorpe, S. J., Yoshino, S., and Thomas, G., "Blade Tip Heat Transfer In Transonic Heat Transfer", Journal of power and energy, Vol. 219 part A, 2005.

16. Metzger, D. E., Dunn, M. G., and Hah, C., "Turbine Tip and Shroud Heat Transfer", Journal of Turbomachinery, Vol. 113, pp. 502-507, 1991.

17. Matsunama, T., "Effects of Reynolds Number and Freestream Turbulence on Turbine Tip Clearence Flow", Journal of Turbomachinery, Vol. 128/ 167, 2006.

18. Rhee, D., and Cho, H. H., "Local Heat/Mass Transfer Characteristics On A Rotating Blade With Flat Tip In Low-Speed Annular Cascade- Part1: Near-Tip Surface", Journal of Turbomachinery, Vol. 128/96, 2006.

19. Yang, D., and Feng, Z., "Tip Leakage Flow and Heat Transfer Predictions for Turbine Blades", Proceedings of ASME Turbo Expo 2007, GT2007-27728, 2007.

20. Haller, B. R., and Hilditch, M. A., "External Heat Transfer on a Shrouded HP Gas Turbine Stage", Proceedings of ASME Turbo Expo 2007, GT2007-27168, 2007.

21. Loma, A., Paniagua, G., Verrastro, D., and Adami, P., "Transonic Turbine Stage Heat Transfer Investigation in Presence of Strong Shocks", Proceedings of ASME Turbo Expo 2007, GT2007-27101, 2007.

22. Harvey, N. W., and Ramsden, K., "A computational Study of a Novel Turbine Rotor Partial Shroud", Journal of Turbomachinery, Vol. 123/534, 2001.

23. Camci, C., Dey, D., and Kavurmacioglu, L., "Aerodynamics of Tip Leakage Flows Near Partial Squaler Rims In An Axial Flow Turbine Stage", Journal of Turbomachinery, Vol. 127, pp. 14-24, 2005.

24. Saha, A. K., Acharya, S., Bunker, R., and Prakash, C., "Blade Tip Leakage Flow with Pressure Side Winglet", International Journal of Rotating Machinery, Volume 2006, Article ID 17079, Pages 1-15, 2006.

25. Kusterer, K., Moritz, N., Bohn, D., Sugimoto, T., and Tanaka, R., "Reduction of Tip Clearance Losses in an Axial Turbine by Shaped Design of the Blade Tip Region", Proceedings of ASME Turbo Expo 2007, GT2007-27303, 2007.

26. Krishnababu, S. K., Dawes, W.N., Hodson, H. P., Lock, G. D., Hannis, J., and Whitney, C., "Aero thermal Investigations of Tip Leakage Flow In Axial Flow Turbines Part II: Effect Of Relative Casing Motion", Proceedings of ASME Turbo Expo 2007, GT2007-27368, 2007.

27. Ameri, A. A., Steinthorsson, E., and Rigby, D. L., "Effect of Squealer Tip on Rotor Heat Transfer and Efficiency", Journal of Turbomachinery, Vol. 120, pp. 753-759, 1998.

28. Thomas, B., and Kalfas, A. I., and Abhari, R. S., "Control Of Rotor Tip Leakage Through Cooling Injection From The Casing In A High Work Turbine: Experimental Investigation", Proceedings of ASME Turbo Expo 2007, GT2007-27269, 2007.

29. Saxena, V., Nasir, H., and Ekkad, S. V., "Effect of Blade Tip Geometry on Tip Flow and Heat Transfer", Journal of Turbomachinery, Vol. 126, pp. 130-138, 2004.

30. He, L., Menshikova, V., and Haller, B. R., "Influence of Hot Streak Circumferential Length-Scale in Transonic Turbine Stage", ASME Turbo Expo 2004, GT2004-53370, 2004.

31. Molter, S., M., Dunn, M. G., Haldeman, C. W., Bergholz, R. F., and Vitt, P., "Heat Flux Measurements and Predictions for the Blade Tip Region of A High Pressure Turbine", ASME Turbo Expo 2006, 6-90048, 2006.

32. Gaetani, P., Persico, G., Dossena, V., and Osnaghi, C., "Investigation of the Flow Field in a High-Pressure Turbine Stage for Two Stator-Rotor Axial Gaps- Part II: Unsteady Flow Field", Journal of Turbomachinery, Vol. 129, pp. 580-590, 2007.

33. Adami, P., Denos, R., and Fidalgo, V. J., "Transport of Unsteadiness across the Rotor of a Transonic Turbine Stage", ASME Turbo Expo 2006, GT2006-90462.

34. Loma, A. D., Paniagua, G., and Verrastro, D., "Transonic Turbine Stage Heat Transfer Investigation in Presence of Strong Shock", ASME Turbo Expo 2007, GT2007-27101, 2007.

35. Xie, Y., Lan, J. B., Fan, T., and Zhang, D., "An Investigation of Unsteady Aerodynamic load on Turbine Blade Considering Rotor-Stator Interactions", Preceedings of ISABE, ISABE-2007-1257.

36. Phutthavong, P., Hassan, I., and Lucas, T., "Unsteady Numerical Investigation of Blade Tip Leakage, Part 1: Time-Averaged Results", Journal of Thermophysics and Heat Transfer, Vol. 22, No. 3, pp. 464-473, 2008a.

37. Phutthavong, P., Hassan, I., and Lucas, T., "Unsteady Numerical Investigation of Blade Tip Leakage, Part 2: Time-Dependent Parametric Study", Journal of Thermophysics and Heat Transfer, Vol. 22, No. 3, pp. 474-484, 2008b.

38. Wilcox, D.C.,"Multiscale model for turbulent flows",In AIAA 24th Aerospace Sciences Meeting. American Institute of Aeronautics and Astronautics, 1986.

39. F. R. Menter, M. Kuntz and R. Langtry "Ten Years of Industrial Experience with the SST Turbulence Model", Turbulence, Heat and Mass Transfer 4, Begell House, Inc., 2003.

40. Kader, B.A., "Temperature and concentration profiles in fully turbulent boundary layers", International Journal of Heat and Mass Transfer, 24(9):1541-1544, 1981.

41. Roux, J., M., Mahe′, P., Sauthier, B., and Duboue′, J. M., "Aerothermal predictions with transition models for high-pressure turbine blades", Proceedings of International Mechanical Engineers, Vol. 215, Part A.

42. Hilditch, M. A., Smith, G. C., Anderson, S. J., Chana, K. S., Jones, T. V., Ainsworth, R.W. and Old. eld, M. L. G., "Unsteady measurements in an axial Flow turbine", Prec3eedings of AGARD Conference 1996, pp. 571.

43. Krieger, M. W., Lavoie, J. P., Vlasic, E. P., and Moustapha, S. H., "Off-Design Performance of a Single-Stage Transonic Turbine", Journal of Turbomachinery, Vol. 129, pp. 177-183, 1999.

44. Hah, C., "A Navier-Stokes Analysis of Three-Dimensinonal Turbulet Flows Inside Turbine Blade Rows at Design and Off-Design Conditions", ASME Journal of Engineering for Gas Turbine and Power, Vol. 106, pp. 421-429, 1984.

45. Moustapha, H., Gas Turbine Design, Lecture Notes, 2007.

46. Ansys CFX version-11 documentation.

Appendix

A. Mathematical Formulation of Automatic Wall Function

The wall-function is an approach through which the near wall tangential velocity is related to the wall-shear-stress in the log-law region by means of a logarithmic relation.

In this approach, the viscosity affected sublayer region is calculated by employing empirical formulas to provide near-wall boundary conditions for the mean flow and turbulence transport equations. These formulas connect the wall conditions (e.g., the wall-shear-stress) to the dependent variables at the near-wall mesh node which is assumed to lie in the fully-turbulent region of the boundary layer.

The logarithmic relation for the near wall velocity is given by:

$$u^{+} = \frac{U_t}{u_\tau} = \frac{1}{\kappa}\ln(y^{+}) + C \tag{A.1}$$

where:

$$y^{+} = \frac{\rho \Delta y u_\tau}{\mu} \tag{A.2}$$

$$u_\tau{}^{+} = \left(\frac{\tau_\omega}{\rho}\right)^{\frac{1}{2}} \tag{A.3}$$

u^{+} is the near wall velocity, u_τ is the friction velocity, U_t is the known velocity tangent to the wall at a distance of Δy from the wall, y^{+} is the dimensionless distance from the wall,

τ_ω is the wall shear stress, κ is the von Karman constant and C is a log-layer constant depending on wall roughness (natural logarithms are used).